Development and Validation of Scale-resolving Computational Models Relevant to IC-engine Flow Configurations

Vom Fachbereich Maschinenbau
an der Technischen Universität Darmstadt
zur
Erlangung des Grades eines Doktor-Ingenieurs (Dr.-Ing.)
genehmigte

D i s s e r t a t i o n

vorgelegt von

Dipl.-Ing. Chi-Yao Chang

aus Taipeh, Taiwan, R.O.C.

Berichterstatter:	Prof. Dr.-Ing. C. Tropea,
	Prof. Dr.-Ing. S. Jakirlić,
	Prof. Dr.rer.nat. A. Sadiki
Tag der Einreichung:	10.12.2013
Tag der mündlichen Prüfung:	20.01.2014

Darmstadt 2015
D17 (Diss. Darmstadt)

Hiermit versichere ich, die vorliegende Doktorarbeit unter der Betreuung von Prof. Dr.-Ing. C. Tropea und Apl. Prof. Dr.-Ing. S. Jakirlić nur mit den angegebenen Hilfsmitteln selbständig angefertigt zu haben.

Darmstadt, den 10. Dezember 2013

For my parents, my brother Daniel,
and my girlfriend Sarah.

Abstract

Turbulent swirling and tumbling flow currents are dominating phenomena in the internal combustion engine systems. These occurrences have great influence on the quality of fuel-air mixture and combustion. Concerning the employment of the CFD (Computation Fluid Dynamics) methods for relevant flow simulations, the LES (Large Eddy Simulation) method is becoming more and more the computational tool in the field of engine design and optimization, thanks to its predictive capability to better estimate the rotational characteristics and cycle-to-cycle variations. This method compensates the disadvantages of classical RANS (Reynolds Averaging Navier-Stokes) models of turbulence by resolving the instantaneous flow structures. However, it is accompanied by uncertainties concerning the required mesh resolution.

The hybrid eddy-resolving methods, which gain increased popularity in the CFD community, are conceptualized to combine the advantageous characteristics of RANS and LES. This leads to an advanced modeling strategy for complex flow configurations at higher Reynolds numbers. On one hand, the large flow structure is captured in accordance with the applied grid spacing; furthermore, the small structures are computed by an appropriately modified RANS model of turbulence.

In the present work, an eddy-resolving model, denoted as "Very Large Eddy Simulation" (VLES) according to Speziale (1998), is formulated and validated. The validations are preliminary carried out by computing some important generic configurations as decay of homogeneous isotropic turbulence (Tavoularis et al. (1997); underlying the basic turbulence law concerning its natural decay), plane channel flow (Moser et al. (1999); most important representative of wall-bounded flow configurations for studying the near-wall turbulence) and flow over a periodical arrangement of two-dimensional hills (Temmermann et al. (2003); separation at a curved continuous surface) to check the model's predictive capabilities. Furthermore, a real three-dimensional swirling flow in a vortex tube with different shapes of outlet orifices (investigated experimentally by Grundmann et al.,2012) and a generic piston-cylinder assembly focusing on the compression of a tumbling vortex generated during the intake phase (experiment by Borèe

et al., 2001) were computed to examine whether the relevant flow properties can be correctly captured computationally. Finally, an industrial engine system (not accounting for the spray and combustion) for which the experimental reference is provided by Baum et al. (2013) is considered for the final validation to see the suitability of the turbulence models formulated presently for the application in internal combustion engines.

Compared to both the Partially Averaged Navier-Stokes (PANS) and RANS methods (the four-equation k-ζ-f model of Hanjalić et al., 2004, was used as the RANS constituent in the present hybrid scheme; in addition the pure LES and RANS computations, the latter employing the same model as the PANS and VLES, have been performed), the present eddy-resolving model exhibits better reproduction of the corresponding reference data. The VLES, which suppresses the modeled turbulent properties to the level of subgrid-scale explicitly by appropriately modifying the turbulent viscosity model, is especially capable of triggering the fluctuation in the entire flow region, whereas PANS shows a too diffusive representation. These features enable the calculation to preserve the LES operating mode in the configurations where the employment of a RANS model is not satisfactory. Furthermore, the VLES method utilizes the currently computed (instantaneous) values without having to extract the averaged properties. This also avoids the problem the PANS method has in the time-dependent calculation of flows with moving boundaries.

Kurzfassung

Turbulente verdrallte Strömung und "Tumbling motions" sind die dominierenden aerodynamischen Phänomene im Verbrennungsmotor, die sowohl die Mischung zwischen Luft und Brennstoff, als auch den Verbrennungsprozess stark beeinflussen. In den Anwendungen der Numerischen Strömungsmechanik (CFD - *Computational Fluid Dynamics*) findet die Methode der Grobstrukturtursimulation (LES - *Large Eddy Simulation*) immer mehr die Verwendung im Design- und Optimierungprozess der Verbrennungsmotoren dank der korrekten Erfassung der strukturelen Eigenschaften der drallbehafteten Strömung sowie deren zyklischen Veränderungen. Diese Methode kompensiert den Nachteil der RANS-Vorgehensweise (nach Reynolds gemittelte Navier-Stokes'sche Methode) durch Auflösen der instantanen turbulenten Strukturen, obgleich die durch die Gitterauflösung bedingte Genauigkeit zu prüfen ist. Die hybriden Modellierungsstrategien, die in den letzten Jahren stark an der Popularität in der CFD-Community gewonnen haben, koppeln die besten Eigenschaften der LES und RANS Methoden: einerseits sind die großen, energie-tragenden Wirbelstrukturen entsprechend der Gitterbreite aufgelöst; anderseits sind die hoch-frequenten turbulenten Skalen von den Modellen umfasst.

In der vorliegenden Arbeit wird die sogenannte "Very Large Eddy Simulation" Methode (VLES) formuliert und validiert. Die Validierung wird zuerst anhand einiger wichtiger generische Fälle durchgeführt, um das allgemeine Verhalten des Modells zu überprüfen. Die Testfälle beziehen sich auf "das Abklingen der homogenen isotropen Turbulenz" (referente direkte numerische Simulation - DNS - wurde von Tavoularis et al.(1997) durchgeführt; hier geht es um den grundlegenden Prozess des natürlichen Abklingens der Turbulenz), die "turbulente Kanalströmung" (DNS von Moser et al.(1999), dies stellt den wichtigsten Testfall zur Untersuchung der Turbulenz im wandnahen Bereich) und die "periodische Strömung über einen zweidimensionalen Hügel" (LES von Temmermann et al.(2003) zur Untersuchung der separierenden Scherschicht an einer gekrümmten kontinuierlichen Oberfläche). Weitere Validierung der hier formulierten VLES Methode ist anhand der Berechnung der verdrallten Strömung in einem Wirbel-Rohr (experimentell untersucht von Grundmann et al.(2012)) und

einer generischen Motorkonfiguration (experimentell untersucht von Borée et al.(2001)) durchgeführt. Das Ziel war zu prüfen, ob die entsprechenden physikalischen Phänomene wiedergegeben werden können. Letztendlich wurde eine reale Motorgeometrie mit den sich bewegenden Ventilen und dem Kolben (ohne Kraftstoffeinspritzung und Verbrennung) berechnet. Die Referenzdaten wurden im Rahmen des Experimentes von Baum et al.(2013)) zur Verfügung gestellt.

Zudem wurden all die aufgeführten Strömungsfälle mit der "Partially Averaged Navier-Stokes" (PANS) Methode und der konventionellen RANS Methode (das Vier-Gleichungsmodell k-ζ-f von Hanjalić et al.(2004) wurde eingesetzt; dieses RANS Modell stellt den Bestandteil sowohl der PANS als auch der VLES Methode dar) berechnet. Das VLES hybride Modell liefert vielversprechende, zu den entsprechenden LES und experimentellen Daten komplementäre Ergebnisse. Vor allem dort, wo keine geometrisch bedingte Generierung der Instationarität der Turbulenz vorhanden ist (wie im Fall einer Ablösung), ist VLES fähig, die Geschwindigkeitsfluktuationen aufzulösen, während PANS zu diffusiv erscheint. Die Eigenschaft von VLES, die modellierten turbulenten Größen explizit zum Feinstruktur-Level (*sub-scale*) zu unterdrücken, ermöglicht die Erhaltung der fluktuierenden Strömungsstruktur, wie im Fall einer LES. Diese Eigenschaft ist insbesondere in den Konfigurationen nützlich, wo das zu Grunde gelegte RANS Modell nicht geeignet ist. Außerdem ermöglicht die VLES die momentanen Größen im Rahmen der Methode direkt zu berücksichtigen, ohne sie mitteln zu müssen. Dies kommt insbesondere in den zeitlich abhängigen Strömungsfällen mit den sich bewegenden Berandungen (z.B. Ventile und Kolben) zu Geltung.

Acknowledgements

It is a wonderful experience being in SLA for my last 4.5 years doing my Ph.D. For this great time, I would like to thank Prof. Tropea for the opportunity and Prof. Jakirlić for the patient supervising. Special thank goes to the company AVL List GmbH for supporting financially this project, especially to Dr. G. Rainer and PD Dr. B. Basara.

The model validation cannot be successfully performed without relevant reference data. For these, I sincerely appreciate the help of Florain Wassermann, Prof. J. Borèe and Elias Baum for making their experimental data available.

Furthermore, I would like to thank all the colleagues and friends, especially Lukas Lutej and Zoran Pavlovic for helping me by the mesh generation and simulation setups.

Time flies, I still remember the first couple days being in the institute as a new comer. Every one is really nice and soon I felt like belonging to this place. In the last years, it was sometimes really stressful. I stayed in the office till midnight summarizing the results. Sometimes, it was casual. We spent some hours playing soccer on the meadow. What I really love in SLA is the easy atmosphere. There is no estrangement, every colleague is willing to help.

Gisa, Tony and Robert are the three colleagues who really helped me a lot. We were in the same office, doing similar projects, discussing with each other. After work, we went for sport, spending time with each other. For me, they are more like close friends than just colleagues in the office. For this great occasion, I have to thank SLA.

An old Chinese saying reads: "There are too many people I have to thank, so I thank God." I enjoyed the time being in SLA and I will definitely miss here.

May the force be with you.
Darmstadt, December 10th 2013 Chi-Yao Chang

Contents

1 Introduction

Flow structure in the internal combustion engine systems is extremely complex. It is characterized by a multiplicity of different simultaneously occurring processes: fuel injection, two-phase mixture, turbulent swirl and tumbling motions, chemical reaction, etc. Each phenomenon is highly complex exhibiting explicit influence on the engine performance. From the engineering and industrial perspective the understanding of the physics underlying these mechanisms is of decisive importance with respect to the possible engine system optimization. Accordingly, thorough and systematic investigations are required.

In the last decades, the CFD (computational Fluid Dynamics) methods developed to a well-applied prediction tools in solving the problems of fluid mechanics and associated disciplines. Compared to the experimental investigations, CFD provides detailed and extensive illustrations of three-dimensional structure of a turbulent flow; this is also valid for the flow properties (e.g., component of the Reynolds stress dissipation tensor) which are not easily accessible by the measurement technique. However, the simulation results are associated with certain inaccuracies, which depend on the employed numerical methods used for the discretization of the governing equations and the models describing mathematically the transport processes. The latter is specifically the case concerning the models describing turbulence. If the theoretical assumptions representing the rationale of the model development are not fulfilled, they can fail in capturing the turbulent characteristics correctly. Especially in the complex systems, the modeling issue can have a great influence on the quality of simulation results. Therefore, a thorough validation of computational methods together with turbulence models represents an issue of decisive importance in the development of CFD.

1.1 Phenomenon of Turbulence: an Introduction

Appropriate turbulence models are conceptualized to fulfill the underlying physical phenomena. In general, turbulence is an unsteady, irregular and three-dimensional phenomenon. Reynolds number (Re) represents a char-

acteristic quantity used to characterize the fluid flow regime. The Reynolds number represents the ratio of inertial forces (proportional to the product of the characteristic flow velocity and the characteristic length) to the viscous forces (proportional to the kinematic viscosity coefficient):

$$Re = UL/\nu$$

For higher velocities and larger dimensions of a flow configuration, yielding high Reynolds number values, the flow regime is turbulent. Onset of a turbulent flow representing the transition from the laminar to turbulent flow regime occurs at the so-called critical Reynolds number (Re_c). For flow Reynolds numbers smaller than Re_c viscous forces dominate the flow field. Instabilities are damped by the viscous effects and flow remains in the laminar regime. In the turbulent flow regime, the inertial forces overweight the viscous ones enabling turbulent eddy structures developing randomly in a spatio-temporal sense in the entire flow field. Accordingly, the turbulence is characterized by a multiplicity of different time and length scales representing the characteristic sizes and durations of turbulent eddies.

Energy Spectrum

Eddy structure represents the basis of a turbulent flow. There is an overlap of vortices of different shapes and sizes. From the engineering point of view, only the statistical description of a highly unsteady, instantaneous turbulent flow field, expressed by mean values, variance, skewness, etc., is of importance.

The energy spectrum is a specific feature of a turbulent flow, obtained by the Fourier transformation of two-point correlation of the velocity fluctuations pertinent to the homogeneous conditions (zero separation between the points). For flows at different Reynolds number the normalized energy cascade has similar evolution. The turbulent eddy structures can be associated with the energy containing range, inertial sub-range and dissipative range of an energy spectrum, see Fig 1.1.

In the productive, energy containing range, the large eddy structures are generated by the deformation of the mean flow; they contain the most of the turbulent energy. The corresponding energy spectrum slope has the power of 2 in the energy cascade diagram. In the inertial sub-range the process of the energy transfer from large to smaller eddies takes place. In this range, the curve slope follows the power of $-5/3$ representing a very important energy spectra characteristic. This range exists if the Reynolds number is large enough. Otherwise, inertial sub-range is rare to be observed. Dissipation range occupies the area where the smallest, dissipative

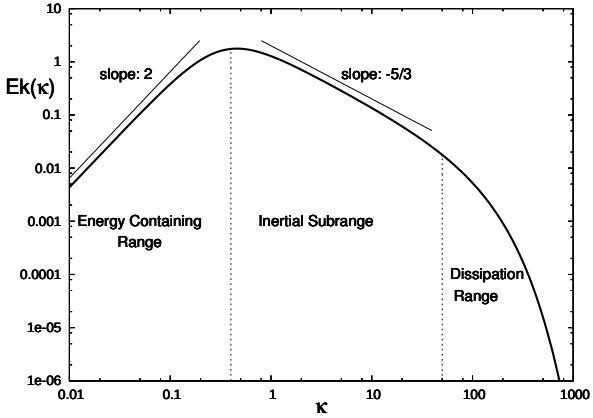

Figure 1.1: Energy cascade of homogeneous turbulence

eddies reside. In this range, the eddies are regarded to be (locally) isotropic; it means that the eddies do not have preferential orientation. The energy pertinent to these eddies dissipates ultimately into the heat duo to viscous effects. Kolmogorov (1991, [45]) defined the characteristic length, time and velocity scales to describe the smallest eddies in a turbulent flow by assuming them dependent on the kinetic energy amount 'survived' through the energy cascade and the fluid viscosity only. Furthermore, he hypothesized that the dissipation takes place only within the smallest length scale range. His arguments have had tremendous influence on turbulence model development. Generally, energy spectra offers plausible quantitative details of the turbulence structure, as e.g. integral time and length scales; turbulent kinetic energy and dissipation rate can also be estimated by the energy cascade representation.

Near-wall Turbulence

Studying turbulence in the wall vicinity is of great importance keeping in mind that the largest majority of the flow configurations of practical importance is surrounded by the solid walls. The near-wall mean flow velocity is strongly influenced by both the viscous and turbulent effects, but the intensity of this influence rates differently, see Fig 1.2 and 1.3.

To parametrize the turbulent effects in the near-wall region, the dimensionless normal-to-wall distance y^+ is introduced, obtained by the normalization of the wall distance y by the viscous length ν/U_τ (with U_τ represent-

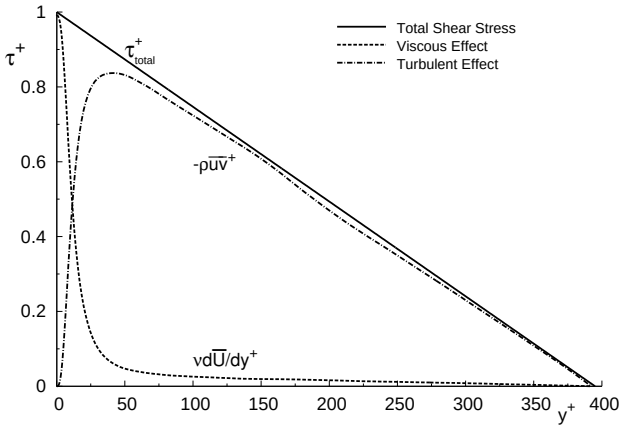

Figure 1.2: Viscous and turbulent shear stress in a wall-bounded flow (here a plane channel)

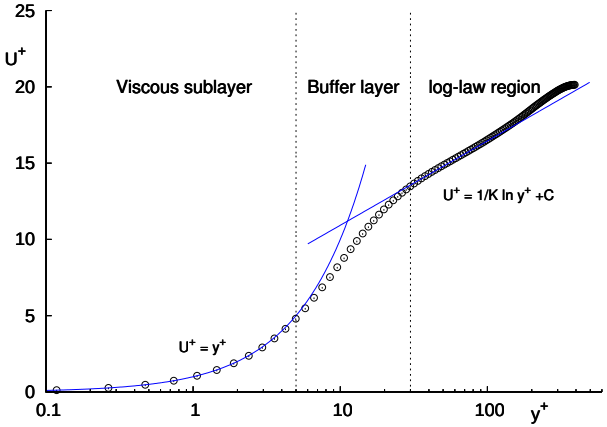

Figure 1.3: Normalized flow velocity profile in the near wall region of a plane channel

ing the 'friction velocity'). For $y^+ < 5$, the shear stress originating from the viscous effects dominate. The mean velocity is linearly proportional to the wall distance. This flow region is termed 'viscous sublayer'. Away

from the wall at $y^+ > 30$, the turbulent effects overweight the viscous ones; the velocity profile underlies the well-known 'law-of-the-wall' expressed by its logarithmic dependence on the distance to the wall, see Fig 1.3. The formulations defining the velocity field pertinent to both viscous sublayer and the logarithmic-law region read as follows:

$$\begin{aligned} U^+ = &\quad y^+ \qquad\qquad \text{for} \quad y^+ < 5 \\ = &\quad \frac{1}{\kappa}\ln y^+ + C \quad \text{for} \quad y^+ > 30, \end{aligned} \tag{1.1}$$

Here, U^+ and y^+ are the normalized velocity and the wall distance, defined as

$$U^+ = U/U_\tau, \quad y^+ = yU_\tau/\nu$$

with the 'wall shear stress velocity'

$$U_\tau = \sqrt{\frac{\tau_w}{\rho}}$$

The buffer layer occupies the range $5 < y^+ < 30$, where the viscous and turbulent properties overlap and none of them has the dominant effect.

Accounting for these near-wall turbulent properties is of great importance with respect to formulating the models for the near-wall treatment, specifically with respect to the development of the so-called 'wall functions' utilized in the numerical simulations.

To summarize: in the last decades, detailed investigations (experimental and numerical) of the turbulence physics became the main topic in scientific activities. Better understanding of the turbulent flow phenomena led not only to a relevant scientific progress, it also provided enhanced conditions for improving and optimizing technical applications.

1.2 Simulation and Modeling of Turbulent Flows: an Overview

Starting point in the mathematical description of a fluid flow are the Navier-Stokes equations, describing comprehensively the flow dynamics independent of the flow regime. However, due to the non-linearity of the terms describing the convective transport in this partial differential equation system, the general analytical solution doesn't exist. Exceptions are a few laminar flow configurations. Thank to the advanced computational technology, the numerical procedures have become the indispensable alternative

to approximate the solution of the Navier-Stokes equations. In the turbulent flow case, the numerical simulation is extremely challenging due to the complex eddy structures exhibiting large range of different length and time scales. A full numerical resolution of a turbulent flow field, i.e. Direct Numerical Simulation (DNS), requires enormous high computational resources.

Direct numerical simulation is the computational method aiming at resolving the complete turbulent flow field. Accordingly, all structures up to the Kolmogorov scales are captured and illustrated in the realizations. According to Pope (2000, [72]) it demands the numerical cell size being smaller than 2.1 times of Kolmogorov lengthscale. Within this range, the estimated dissipation rate does not exhibit qualitative changes in terms of finer resolution. Also, DNS requires high accuracy of the numerical schemes used, it means a high order differencing scheme for the spatial discretization and at least the Range-Kutta 4^{th} order scheme for the temporal discretization.

The higher the Reynolds number, the smaller the size of the Kolmogorov eddies. This gradual reduction of the size of the dissipative eddies with increase of the Reynolds number implies an appropriately high resolution of the numerical grid. Accordingly, the required grid cells number is directly dependent on the Reynolds number following $Re^{9/4}$. This criterion limits the time step to be appropriately fine in order to fulfill the criterion of Courant number, which should be smaller than unity. All this makes the DNS extremely demanding for the flow field under the high Re conditions. Nowadays, DNS is mostly applied in Fourier or Chebyshev mode, which provides correspondingly high accuracy of the employed differencing schemes. However, this method restricts the investigations to simple generic geometries. Due to very high computational costs, a DNS has been currently mostly performed for the scientific purposes.

As the engineers are mostly interested in statistical representation of the turbulent features, the Reynolds decomposition of the instantaneous flow properties appearing in the Navier-Stokes equation into time-averaged and fluctuating parts has been conveniently applied. The consequence of the time-averaging (i.e. ensemble-averaging in the case of the unsteady mean flow) of the continuity and momentum equations is the appearance of a symmetric 2^{nd} order tensor originating from the convective transport term. This tensor, called Reynolds stress tensor, represents statistically the auto-correlation of fluctuating velocity components. Derivation of the exact transport equation of the Reynolds stress tensor leads to appearance of complex, higher order non-closed tensors; such an equation cannot be used

directly providing the solution of all six non-zero Reynolds stress components. Therefore, the Reynolds stress tensor is modeled appropriately within the computational strategy called Reynolds-Averaged Navier-Stokes (RANS) framework. The modeling rationale is based on different mathematical and physical assumptions.

The simplest turbulence models in the RANS framework are the models based on the so-called eddy-viscosity concept. Within this model group the Reynolds stress tensor is, according to Boussinesq (1877), presented as the product of the turbulent viscosity and the mean rate of strain. This so-called Eddy-Viscosity Modelling (EVM) strategy reduces the modeling of the 2nd-rank Reynolds stress tensor (determined by six components) to modeling of the eddy viscosity representing a turbulent property of the scalar nature. The determination of turbulent viscosity was first investigated by Prandtl (1925). He introduced the concept of mixing length using the analogy of the mean free path in thermodynamics by observing a turbulent shear flow. Accordingly, in analogy to the molecular viscosity, the turbulent viscosity is dependent on a characteristic length (termed 'mixing length') and a characteristic velocity, representing the product of the velocity gradient magnitude and the afore-mentioned lengthscale; the latter is to be empirically determined depending on the flow configuration. Furthermore, Prandtl (1945) proposed a one-equation formulation for the turbulent viscosity with the turbulent kinetic energy representing the characteristic velocity scale ($k^{1/2}$). A differential model equation governing the turbulent viscosity was formulated by Spalart and Allmaras (1994, [82]). The model constants and functions have been calibrated by using numerous empirical data; Spalart-Allmaras one-equation model is currently widely applied in the turbo-machinery and aircraft aerodynamics.

First two-equation model based on the eddy-viscosity concept is proposed by Hanjalić (1970, [30]) who derived transport equations for the kinetic energy of turbulence (k) and its dissipation rate (ϵ). The latter variable serves for defining the turbulent length scale ($k^{3/2}/\epsilon$) in the model of the turbulent viscosity. Jones and Launder (1972, [40]) adopted these equations and proposed the well-known k-ϵ model. They introduced a damping function, modeled in terms of the Reynolds number of turbulence, to provide appropriate viscous influence onto the turbulent viscosity in the near-wall region. This model was slightly modified by Launder and Sharma (1974, [52]). The two-equation k-ϵ model, in conjunction with the wall functions for modeling the wall region (Launder and Spalding, 1974, [53]), became, due to its numerical robustness, the most-widely used RANS model for

the last forty years, especially in the industrial environment. Another two-equation eddy-viscosity model has been proposed by Wilcox (1988, [96]) who introduced a 'frequency variable' representing the inverse turbulent time scale ($\omega \propto \epsilon/k$) to provide modeling the near-wall region without further modifications. This model was later improved by Menter (1994, [63]) who introduced some important transport equation details.

The immediate wall vicinity turbulence remains further a tough issue for modeling due to its physical complexity. Durbin (1991, [13]) introduced the transport equation for the normal-to-the-wall stress component ($\overline{v^2}$; actually, in the Durbin's model this variable represents a scalar which behaves similar to the Reynolds stress component by approaching the solid wall) using the elliptic relaxation method to model the pressure-strain correlation. This method represents important improvement of the classical two-equation model. A damping function is not longer needed here. With the aim to increase the numerical robustness of the Durbin's model, Hanjalić et al. (2004, [31]) replaced the variable $\overline{v^2}$ by its ratio to the turbulent kinetic energy k. Accordingly they introduced a new variable $\zeta = \overline{v^2}/k$ enabling finally a weaker dependency of the model equations on the wall distance. Both Durbin's and Hanjalić's et al. models are capable of capturing the influence of the near-wall anisotropy onto the turbulent viscosity by introducing $\overline{v^2}$ variable, i.e. ζ variable to model the characteristic velocity scale. However, the influence of the Reynolds stress anisotropy on the velocity field is, as it is the case with all linear eddy-viscosity models, cannot be captured.

The latter can only be accounted for when the Reynolds stress components appearing in the equation of motion are individually modeled. Such a possibility is offered within the Reynolds-stress model (RSM) group. Here, each Reynolds stress component represents the solution of its own differential equation. Herewith the specific, individual dynamics of the Reynolds stress components can be captured. Launder et al. (1975, [51]), Speziale et al. (1991, [84]), Durbin (1993, [14]) and Jakirlić and Hanjalić (2002, [37]) dedicated their effort to derive such models. A possibility to derive an algebraic version of the Reynolds stress model by neglecting the transport properties of a differential model version was investigated by Wallin and Johansson (2000, [94]). Since there are many terms in the Reynolds stress transport equations which have to be further modeled, the numerical robustness represents an important issue in the calculation employing a RSM model.

Instead of averaging turbulent flow properties, the Large Eddy Simula-

tion (LES) method applies the concept of spatial filtering. Accordingly, the instantaneous flow quantities are decomposed into the resolved and subgrid (unresolved) scales by introducing a filter function; in the most frequently applied LES methods the numerical grid itself plays the role of a filter function - one deals here with the so-called implicit filtering. The turbulent flow properties not resolved by the grid, representing the so-called 'residual turbulence' of the LES method, are estimated by applying an appropriately formulated subgrid-scale (SGS) model. The role of the subgrid-scale models is to dissipate turbulent kinetic energy at the grid level. The most-known and most-widely applied SGS LES model was proposed by Smagorinsky and Manabe (1962, [81]). They adopted the Prandtl's mixing length concept and applied it to model the subgrid scale turbulence. They assumed the subgrid turbulent length scale being proportional to the numerical grid size, and the relevant velocity scale to the resolved velocity gradient. Later, Germano et al. (1991, [20]) presented the so-called dynamic subgrid scale model to variably determine the Smagorinsky constant by weighting the resolved and filtered stress tensors. However, the underlying assumptions are only valid if the grid size corresponds to the spectral cut-off laying well within the inertial sub-range (close to the dissipative region), in which the modeled turbulent production is equal to the turbulence destruction term. Otherwise, the modeled turbulent viscosity will be underestimated. This can lead to the unrealistic representation of the simulation results. Near-wall turbulence modeling is difficult topic also within the LES framework. Since the turbulent eddy sizes are correspondingly reduced by approaching the solid wall, a very fine grid resolution in the wall vicinity is required. Accordingly Nicoud and Ducros (1999, [66]) proposed the wall-adapting local eddy-viscosity model (WALE), which is based on the velocity gradient tensor and capable of capturing appropriately the near wall turbulent features. It is furthermore important to mention the so-called coherent structure Smagorinsky model from Kobayashi et al. (2007, [44]). Besides these zero-equation SGS models the so-called transport models have also been proposed. The most prominent is the one-equation model by Yoshizawa (1985, [98]) which employs the transport equation to describe the dynamics of the subgrid turbulent kinetic energy used to estimate properly the corresponding turbulent velocity scale. Kim and Menon (1995, [42]) proposed the dynamic version of this model. Comparing to the RANS framework, the turbulent eddy structures are resolved by applying the LES method. The time-averaged turbulence anisotropic features are evaluated afterwards by applying the averaging procedure. The LES method is substantially less-

demanding compared to DNS, but it still didn't reach the level to be true industrial standard due to the high computational costs.

Demands for fine spatial and temporal resolution within the LES framework and the incapability of RANS method to capture any spectral dynamics (it is especially visible when computing flow separated from continuous curved surfaces exhibiting a broader frequency range) led to hybrid LES/RANS methods. Here appropriately adjusted (mostly by introducing the grid-spacing as a model parameter) RANS-based models mimic the subgrid-scale models. The entire flow field is realized in an unsteady manner (we recall that running a classical RANS model in an unsteady framework cannot capture any turbulent fluctuations). The employment of such eddy-resolving (ER) models enables use of coarser grid resolutions. Generally speaking, ER methods are based on a grid-spacing-based filter function, which helps resolving the flow structures to a certain extent in accordance with the mesh resolution. In the regions meshed by a coarser grid, the ER methods imply intensified application of the RANS-based SGS model to handle the unresolved properties. The activities on development of the eddy-resolving methods have been significantly intensified in the last years. The concept of Very Large Eddy Simulation(VLES), representing a seamless hybrid LES/RANS method, was first proposed by Speziale (1997, [83]). Accordingly a RANS model is applied in unsteady mode by introducing a built-in function to modify the subgrid scale turbulent viscosity. Similar methodology was also applied and validated in a two-dimensional backward-facing step flow by Koutmos and Mavridis (1997,[46]). Within the VLES computational framework, Johansen et al. (2004, [39]) modified the built-in function and calibrated it based on the Kolmogorov energy spectrum. This formulation has been followed and discussed by Han et al. (2012, [28][97]) who used different eddy-viscosity-based RANS models. One of the most prominent Hybrid LES/RANS methods is certainly the Detached Eddy Simulation(DES)[88] method. In the original version from 1997 the one-equation model proposed by Spalart and Allmaras is used for modeling the relevant turbulent viscosity. An appropriate length scale representing the switch between the wall distance (implying the RANS operating mode) and the respective grid-spacing measure (implying the DES functioning in the LES mode) is implemented in the nominator of the corresponding destruction term. The Scale Adaptive Simulation (SAS) method, proposed by Menter and Egorov (2010, [64]), is a novel Unsteady RANS method being capable of capturing the turbulence unsteadiness. The key-element is the model term in the scale-supplying equation formulated in

terms of the von-Karman length scale. This term comprises the ratio of the first to the second derivative of the velocity field. The latter derivative represents a measure of the variability of the vortex structures. The resolved and modeled turbulent flow characteristics are realized in an implicit manner. Maduta and Jakirlić (2012, [59]) applied the SAS methodology to a near-wall Reynolds stress model. The so-called Partially Averaging Navier-Stokes (PANS) method is developed by Girimaji (2006, [22]) as the seamless bridging technique between RANS and DNS. Girimaji introduced the ratio of modeled-to-total turbulent properties, which defines the modeling level in different regions in the flow domain. Similar concept is followed by Schiestel and Dejoan (2005, [77]) within the so-called Partially-Integrated Turbulence Model (PITM). [23] and [58] validated PANS method by means of computing different flow geometries by adopting a constant value of the model-to-total ratio of the kinetic energy of turbulence. To make this ratio variable, Girimaji and Abdol-Hamid (2005, [24]) introduced its dependency on the grid-spacing and turbulent length scale. Schiestel and Dejoan (2005, [77]) defined the corresponding ratio by analyzing the Kolmogorov energy spectrum. Such a model constellation is validated by computing different generic geometries employing a RSM-based model by Fadai-Ghotbi et al. (2010, [17]). The quality of the results obtained by an ER method depends strongly on the background RANS model; it relates especially to the regions featured by high modeling level. Following the idea of Girimaji and Abdol-Hamid (2005, [24]), Basara et al. (2011, [5]) combined the concept of the PANS computational strategy and the advantages of the afore-mentioned near-wall k-ζ-f model. This model scheme represents a near-wall extension of the PANS method validated intensively in several generic and industrial flow configurations, e.g. in [47] [49] and [29].

1.3 Development of Internal Combustion Engines: a short Notice

Internal combustion engine(ICE) represents the core of an automobile powertrain system, which is encountered in over 99% of current vehicles worldwide. From the engineering perspective, the development of an IC engine accounts for optimization of many parameters, such as pollutant emissions, durability, etc. For all these considerations, the economic focus is always of great concern. On one hand, the fuel consumption of vehicles should be as low as possible. On the other hand, the engine power should be maximized;

accordingly an efficient combustion process becomes the main target within the engine development process.

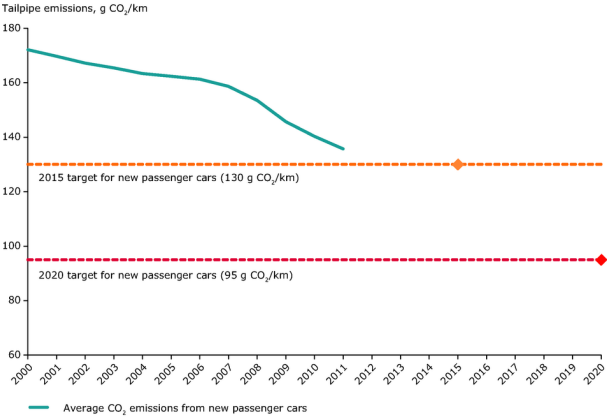

(a) Evolution and targets of CO_2 emission

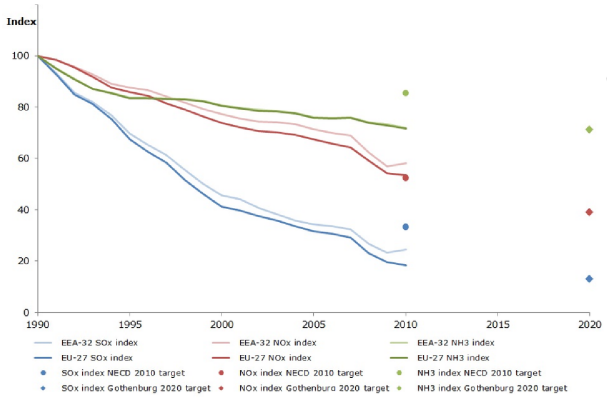

(b) Evolution and targets of SOx, NOx and NH_3 emission

Figure 1.4: European emission standards for CO_2 and pollutants [http://www.eea.europa.eu]

Environmental focus is another important issue in the engine development. Due to the global climate change, corresponding laws are made to lower the pollution on Earth. According to the European Emission Standards, the CO_2 and NOx emission of new passenger cars in 2020 should

be reduced by about 50% of the values from 1990, see Fig 1.4. These restrictions force the automobile industry to develop clean and ecologically beneficial vehicles. All these legislative restrictions and economic ambitions point to the engine system, at which the optimal combustion process is aimed. In other words, if the fuel can be consumed thoroughly, the exhaust pollutants can also be controlled. At the same time, power efficiency can be improved. This intention requires detailed investigations of flow characteristics in the IC engine. Looking at the mechanism encountered in a single cylinder spark-ignition(SI) engine, where, for instance, fuel is injected during the intake stroke building up the mixture with the air flow. Subsequently, ignition occurs after the compression stroke and the flame propagates within the whole combustion chamber. During this process, the potential energy is transformed by the chemical reaction into mechanical energy of the flow, inducing finally the piston displacement. Accordingly, the relevant investigations focus on issues such as air flow in combustion chamber, movement of spray and drop interaction, fuel air mixture, ignition and flame propagation, etc. Accordingly, relevant flow configurations are extremely complex, geometrically but also with respect to the turbulence structure. Among all afore-mentioned phenomena, the turbulent flow characteristics play the role of decisive importance influencing to great extent other features, mostly the air flow structure in the entire engine system. Hence, the thorough understanding of turbulence is the most important goal when investigating an engine configuration.

1.4 Turbulent Swirl and Tumbling Flows: some introductory Remarks

Swirling flow effects and tumbling motion are the most important aerodynamic phenomena encountered in the internal combustion engine system. For instance in a four stroke engine, the air is sucked through the valve into the combustion chamber during the intake stroke. Due to the piston movement, the air flows along the chamber wall generating large structures, which create the tumbling motion. In addition, due to the asymmetric arrangement of the valves, swirling flow is generated. The axis of the swirling vortex is parallel to the piston velocity direction, see Fig 1.5(a). The interaction of swirl and tumbling movements contributes decisively to the complexity of the aerodynamic properties of a combustion chamber.

Tumbling motion is a special feature appearing specifically in the inter-

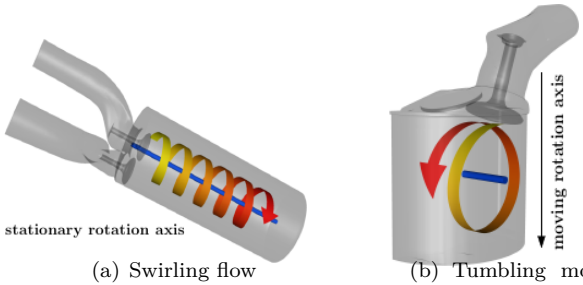

(a) Swirling flow (b) Tumbling motion

Figure 1.5: Illustrations of swirl(left) and tumbling(right) flows[19]

nal combustion engine system. This flow phenomenon is characterized by a large rotational structure with the axis being perpendicular to the direction of piston velocity, see Fig 1.5(b). In general, the utilization of the tumble is to increase the turbulence intensity during the compression process in the combustion chamber before the ignition occurs. The increased turbulence level contributes to the enhancement of the flame stability and thermal efficiency during the combustion process. Currently, such a flow configuration is widely applied in the engine design in the automobile industry.

Unlike the tumbling motion, swirling flow is a well observed phenomenon in the nature and industrial practice. Natural phenomena resemble for instance a water in a basin flowing into the weep-hole generating a whirlpool, similar to the air mass movement in a tornado shown in the weather broadcast, etc. They all contain a large rotational structure generated externally. Swirling flow is also followed by a high turbulence level. Special features of a swirling flow are applied in many engineering devices. Cyclone separator for instance, see Fig 1.6(a), uses the centrifugal force to separate solid particles from gaseous phase. Regarding heat transfer, Ranque-Hilsch vortex tube is conventionally applied to separate compressed gas into hot and cold streams, see Fig 1.6(c). The most significant application of swirling properties is the design of combustion chambers, where the swirl generators are employed for the purpose of efficient ignition and stable combustion. Accordingly, the swirling effects causes break-up of the injected fuel into small droplets, producing homogeneous mixture of fuel and air. Besides, the associated, swirl-induced recirculation zone, generated in the center of combustor, enhances the flame stability, see Fig 1.6(b). Nowadays, this

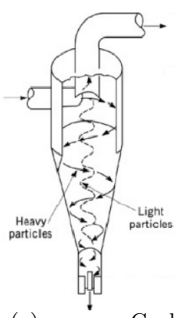

(a) Cyclone separator[79]

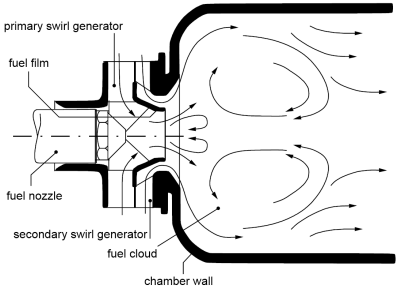

(b) Combustion chamber[35]

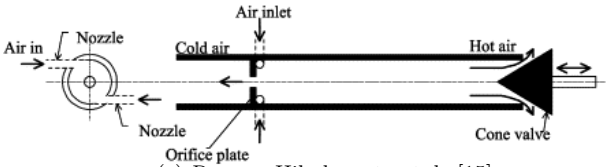

(c) Ranque-Hilsch vortex tube[15]

Figure 1.6: Examples of swirling flow applications (schematics)

configuration represents the standard design concept in the gas turbine combustion system.

1.5 Outline of the present Work

A competent numerical simulation encompasses several integral parts, all being of decisive importance with respect to its predictive capability. First, a proper computational mesh is required. The mesh resolution has explicit effects on the quality of results. Another crucial factor is the computational method consisting of equations governing the flow field in a configuration considered and a numerical method employed for their spatial and temporal discretization. Most important part of the mathematical model are the transport equations describing the associated turbulence phenomena.

The PANS and VLES methods, both representing the eddy resolving methods, are the computational frameworks being of prime importance in the present work. Principally, the employment of both methods results

in a fluctuating turbulent flow field correlated closely to the applied mesh resolution. The PANS method developed by Basara et al. (2011, [5]) was straightforwardly applied to the flow configurations relevant to the IC engine aiming at its thorough validation by assessing its physical rationale in wall-bounded flow configurations. In contrast, the VLES method represents the method developed in present work. Instead of adjusting the sink term in the transport equation of the turbulent dissipation rate affecting appropriate reduction of the kinetic energy of turbulence towards a subgrid-scale level within the PANS framework, the VLES method implies appropriate suppression of the relevant turbulent viscosity towards the one corresponding to the residual turbulence of the LES method, but by employing a coarsened spatial and temporal resolution.

Before applying these eddy-resolving turbulence models to the internal combustion engine configurations, they should be thoroughly validated in a broad range of wall-bounded flows featured by separation, swirling and tumbling motion. In chapter 2, a detailed theoretical rationale of the RANS, LES, and hybrid LES/RANS computational methods in conjunction with the background turbulence models is given. It is worth noting that even if the numerical procedures used for obtaining corresponding solutions are identical, their physical backgrounds are very different. After introducing turbulent models, a brief description of the numerical procedure utilized in the present work is given in chapter 3, where the interpolation and discretization methods of the governing equations and their terms are described. The validations of the PANS and VLES methods by means of computing some relevant generic configurations are carried out in chapter 4. The natural decay of homogeneous isotropic turbulence (underlying the exponential turbulence decay law), flow in a plane channel (representing the most important representative when studying the near-wall turbulence) and flow over a periodic arrangement of two-dimensional hills (exhibiting flow separation from a curved continuous surface) are the selected cases; the corresponding reference data are the DNS results of Tavoularis et al. (1997, [85]), Moser et al. (1999, [65]), the LES data of Temmerman et al. (2003, [86]) and the experimental results made available by Rapp and Manhart (2011, [73]). In addition all these configurations are computed by the LES method as well as by the RANS k-ζ-f model, representing the background RANS model of both PANS and VLES methods, for the sake of comparative assessment.

For the purpose of analyzing computationally some phenomena encountered in the internal combustion engines, the helical structures in a vortex

tube, as well as the generation and compression of a tumbling vortex are computed; the results and associated discussion are displayed in chapter 5. The corresponding reference data are the experimental investigations of Grundmann et al. (2012, [27]) and Borée et al. (2001, [8]). The presently considered eddy-viscosity RANS models are generally not capable of delivering correct results.

Finally, all turbulence models considered are applied to computing the air flow in a realistic, four-stroke internal combustion engine, which is described in chapter 6. This case is based on the experimental investigation of Baum et al. (2013, [6]). It is a very complex configuration used to verify the capability of the turbulence models applied in capturing the relevant aerodynamic phenomena as well as their suitability for industrial usage. The summary of the predictive capabilities of the hybrid models used is discussed in chapter 7 by analyzing their advantages and disadvantages compared to LES and RANS methods. The work closes with an outlook giving some suggestions for possible future development of turbulence models in conjunction with further applications.

2 Mathematical Modeling of Turbulence: theoretical Rationale

The numerical procedure employed within the Computational Fluid Dynamics framework is similar in the case of all turbulence models being conventionally in use - RANS, LES and Hybrid LES/RANS models - for solving the problems of fluid flow and heat transfer. However, different models rely on different theoretical principles. Consequently, they can result in an inherently different flow field.

E.g., RANS is the method relying on the time-averaging procedure. Accordingly, the fluctuating, instantaneous flow field (representing the rationale of the DNS relying on the solution of the three-dimensional, time-dependent Navier-Stokes equations) is transformed statistically into a time-averaged (or ensemble-averaged) flow field. In RANS the turbulence is fully-modeled by an appropriate statistical turbulence model; the outcome are the time-averaged flow features, such as mean velocity, mean pressure, mean temperature as well as the time-averaged turbulent quantities.

Comparing to the RANS rationale, the starting point of the LES method are the spatially filtered Navier-Stokes equations. Accordingly, the three-dimensionality of the fluctuating turbulence can be captured. The quality of the numerical results depends explicitly on the numerical grid resolution.

Hybrid LES/RANS methods represent the variable resolution methods. These, so-called bridging methods provide smooth and seamless transition from RANS to LES in terms of a 'filter-width control parameter' variation. The filter width depends not only on the numerical grid size, but also on the modeled turbulent length scale. Similar as in the case of conventional LES method, the realization of these eddy-resolving method leads to a fluctuating flow field. Unlike in the LES method the fraction of the resolved turbulence can be substantially less than 80%. However, better structural properties of the RANS-based models playing the role of the subscale model enable such a constellation. Accordingly, the turbulence eddies captured by these methods exhibit somewhat larger length and time scales (in accordance with the correspondingly coarser spatial and temporal resolutions), but a lower amount of the resolved turbulence suffices to correctly

capture the time-averaged flow properties, which, in the RANS case, is only possible when computing attached flows influenced by moderate pressure gradients. The flows featured by the organized, large-scale coherent structures and the bulk flow unsteadiness, as encountered e.g. in flows involving separation, are beyond the reach of the RANS models, almost independent of modeling level, unlike it is the case with the eddy-resolving methods.

2.1 Reynolds-Averaged Navier-Stokes (RANS) Approach

The rationale of the RANS computational approach relies on the Reynolds' (1895) proposition. Accordingly, the principles of statistical operation are utilized and a physical property ϕ is decomposed into the mean ($\overline{\phi}$) and fluctuated part (ϕ'), see Fig 2.1.

$$\phi = \overline{\phi} + \phi',$$

The mathematical definition of $\overline{\phi}$ is represented by

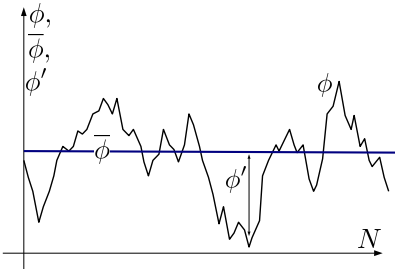

Figure 2.1: Principle of Reynolds averaging

$$\overline{\phi} = \lim_{N\to\infty} \frac{1}{N} \sum_{\xi=1}^{N} \phi^{(\xi)},$$

denoting the property ϕ, averaged over an appropriate amount of samples. Thus, the statistical averaging procedure of $\overline{\phi}$ and ϕ' yields

$$\overline{\overline{\phi}} = \overline{\phi}, \quad \overline{\phi'} = 0.$$

By applying the statistical operation principles and Reynolds decomposition, the transport equation of a mean property $\overline{\phi}$ can be formulated as follows

$$\frac{D\overline{\phi}}{Dt} = \frac{D(\overline{\overline{\phi}+\phi'})}{Dt} = \frac{\partial\overline{\phi}}{\partial t} + \frac{\partial}{\partial x_j}\left(\overline{U}_j\overline{\phi} + \overline{u'_j\phi'}\right), \tag{2.1}$$

with the quantity $\overline{u'_j\phi'}$ appearing in the convection term denoting the correlation of fluctuated physical properties.

The continuity and momentum equations (with ϕ' replaced by u'_i) for a single phase, incompressible flow, without consideration of volumetric force read

$$\frac{\partial\overline{U}_i}{\partial x_i} = 0 \tag{2.2}$$

$$\frac{D\overline{U}_i}{Dt} = \frac{\partial\overline{U}_i}{\partial t} + \overline{U}_j\frac{\partial\overline{U}_i}{\partial x_j} = -\frac{1}{\rho}\frac{\partial\overline{p}}{\partial x_i} + \frac{\partial}{\partial x_j}\left(\nu\frac{\partial\overline{U}_i}{\partial x_j} - \overline{u'_iu'_j}\right). \tag{2.3}$$

Here, $\overline{u'_iu'_j}$ (Reynolds stress) represents the second-order moment of velocity fluctuations originating from the convective transport, which has to be defined by a statistical model of turbulence.

The determination of the Reynolds stress tensor is a very challenging task. Based on the Cayley-Hamilton theorem, Pope (1975, [71]) proposed a most general algebraic formulation of $\overline{u'_iu'_j}$ exhibiting dependency on the mean flow deformation tensors. He formulated the Reynolds stress tensor in terms of the mean rate of strain ($\overline{S}_{ij}$) and mean rate of rotation ($\overline{\Omega}_{ij}$) tensors; this formulation consists of the linear-independent terms up to the fifth order:

$$\begin{aligned}\frac{\overline{u'_iu'_j}}{k} - \frac{2}{3}\delta_{ij} &= \beta_1\overline{S_{ij}} + \beta_2(\overline{S}^2_{ij} - \frac{1}{3}II_S\mathbb{I}) + \\ &\beta_3(\overline{\Omega}^2_{ij} - \frac{1}{3}II_\Omega\mathbb{I}) + \beta_4(\overline{S}_{ij}\overline{\Omega}_{ij} - \overline{\Omega}_{ij}\overline{S}_{ij}) + \\ &\beta_5(\overline{S}^2_{ij}\overline{\Omega}_{ij} - \overline{\Omega}^2_{ij}\overline{S}_{ij}) + \beta_6(\overline{S}^2_{ij}\overline{\Omega}_{ij} + \overline{\Omega}^2_{ij}\overline{S}_{ij} - \frac{2}{3}IV\mathbb{I}) + \\ &\beta_7(\overline{S}^2_{ij}\overline{\Omega}^2_{ij} + \overline{\Omega}^2_{ij}\overline{S}^2_{ij} - \frac{2}{3}V\mathbb{I}) + \beta_8(\overline{S}_{ij}\overline{\Omega}_{ij}\overline{S}^2_{ij} - \overline{S}^2_{ij}\overline{\Omega}_{ij}\overline{S}_{ij}) + \\ &\beta_9(\overline{\Omega}_{ij}\overline{S}_{ij}\overline{\Omega}^2_{ij} - \overline{\Omega}^2_{ij}\overline{S}_{ij}\overline{\Omega}_{ij}) + \beta_{10}(\overline{\Omega}_{ij}\overline{S}^2_{ij}\overline{\Omega}^2_{ij} - \overline{\Omega}^2_{ij}\overline{S}^2_{ij}\overline{\Omega}_{ij})\end{aligned} \tag{2.4}$$

where the mean rate of strain tensor ($\overline{S}_{ij}$) and the mean vorticity tensor ($\overline{\Omega}_{ij}$) are defined as,

$$\overline{S}_{ij} = \frac{1}{2}\left(\frac{\partial\overline{U}_i}{\partial x_j} + \frac{\partial\overline{U}_j}{\partial x_i}\right), \quad \overline{\Omega}_{ij} = \frac{1}{2}\left(\frac{\partial\overline{U}_i}{\partial x_j} - \frac{\partial\overline{U}_j}{\partial x_i}\right), \tag{2.5}$$

and

$$II_S = tr\{\overline{S}_{ij}^2\}, \quad II_\Omega = tr\{\overline{\Omega}_{ij}^2\}, \quad III_S = \{\overline{S}_{ij}^3\}$$
$$IV = tr\{\overline{S}_{ij}\overline{\Omega}_{ij}^2\}, \quad V = tr\{\overline{S}_{ij}^2\overline{\Omega}_{ij}^2\}$$

are the five independent invariants of the combination of $\overline{S}_{ij}$ and $\overline{\Omega}_{ij}$ the β coefficients are based upon.

The most widely used formulation for the engineering purposes is the linear one proposed by Boussinesq (1877). He adopted the linear dependency on $\overline{S}_{ij}$ tensor and introduced the concept of turbulent viscosity ν_t. Thus, Reynolds stress tensor can be formulated as follows

$$\overline{u_i' u_j'} = 2\nu_t \overline{S}_{ij} - \frac{1}{3}\overline{u_k' u_k'}\delta_{ij}, \tag{2.6}$$

The corresponding momentum equation takes the following form

$$\frac{D\overline{U}_i}{Dt} = \frac{\partial \overline{U}_i}{\partial t} + \overline{U}_j \frac{\partial \overline{U}_i}{\partial x_j} = -\frac{1}{\rho}\frac{\partial \overline{p}}{\partial x_i} + \frac{\partial}{\partial x_j}\left[(\nu + \nu_t)\frac{\partial \overline{U}_i}{\partial x_j}\right]. \tag{2.7}$$

In the Boussinesq's correlation (Eq 2.6) the turbulent viscosity ν_t represents a scalar variable. The models relying on this correlation cannot capture the influence of the Reynolds stress anisotropy on the velocity field. This is one of the most important weaknesses of the eddy-viscosity model group. This weaknesses is especially manifested in the flow configurations exhibiting swirling and rotating effects, strong streamline curvature and stagnation regions. Some of these details will be discussed in following sections.

To determine the turbulent viscosity, Prandtl utilized the analogy of the concept of mean free path of molecules in the thermodynamics to the motion of the turbulent eddies and defined the turbulent viscosity (ν_t) to be proportional to their characteristic length (l_c) and velocity scales (u_c).

$$\nu_t \propto u_c l_c \tag{2.8}$$

2.1.1 k-ϵ model

Jones and Launder (1972, [40]) adopted the model equations governing the kinetic energy (k) of turbulence and its dissipation rate (ϵ) proposed by

Hanjalić (1970, [30]) and formulated the well-known k-ϵ model of turbulence. These two turbulent quantities are used to determine the turbulent length ($k^{3/2}/\epsilon$) and velocity scales ($k^{1/2}$). Thus, the turbulent viscosity is formulated as

$$\nu_t = C_\mu \underbrace{k^{1/2}}_{u_c} \underbrace{\frac{k^{3/2}}{\epsilon}}_{l_c}. \tag{2.9}$$

k and ϵ are defined as follows:

$$k = \frac{1}{2}\overline{u_i' u_i'}$$

$$\epsilon = 2\nu \overline{\frac{\partial u_i'}{\partial x_j}\frac{\partial u_j'}{\partial x_i}}.$$

These two turbulent properties are calculated by the following transport equations:

$$\frac{Dk}{Dt} = \frac{\partial k}{\partial t} + \overline{U}_j \frac{\partial k}{\partial x_j} = P_k - \epsilon + \frac{\partial}{\partial x_j}\left[\left(\nu + \frac{\nu_t}{\sigma_k}\right)\frac{\partial k}{\partial x_j}\right], \tag{2.10}$$

$$\frac{D\epsilon}{Dt} = \frac{\partial \epsilon}{\partial t} + \overline{U}_j \frac{\partial \epsilon}{\partial x_j} = C_{\epsilon_1}\frac{P_k}{k}\epsilon - C_{\epsilon_2}\frac{\epsilon^2}{k} + \frac{\partial}{\partial x_j}\left[\left(\nu + \frac{\nu_t}{\sigma_\epsilon}\right)\frac{\partial \epsilon}{\partial x_j}\right]. \tag{2.11}$$

Where, P_k is the production term defined as $P_k = 2\nu_t \left|\overline{S}_{ij}\right| \left|\overline{S}_{ij}\right|$; it should be emphasized that the production rate represents an exact term $P_k = -\overline{u_i' u_j'}\partial U_i/\partial x_j$, requiring no modeling when applying a Reynolds stress model of turbulence; however, within the eddy-viscosity model group even this term is modeled; it represents the next important weakness of this modeling concept.

The standard k-ϵ model is formulated without concerning the viscous effect in the near wall region. Thus, the utilization of the so-called wall function (see Launder and Spalding, 1974, [53]) is necessary for the modeling the wall region; actually, by applying this concept the immediate wall vicinity will be bridged, the next-to-the-wall grid cells is located in the logarithmic region.

Aiming at integrating these equations to the wall itself (no need for the wall functions), thus accounting for the near-wall effects - primarily the viscosity effects, Jones and Launder (1972, [40]) and Launder and Sharma (1974, [52]) introduced necessary low Reynolds number extensions. This relates primarily to the damping function f_μ multiplying the turbulent

Table 2.1: Parameters of the RANS k-ϵ model

C_μ	C_{ϵ_1}	C_{ϵ_2}	σ_k	σ_ϵ
0.09	1.4	1.9	1	1.3

viscosity in order to dampen it appropriately when approaching the solid wall; the viscous effects are taken into account by introducing the Reynolds number of turbulence ($Re_t = k^2/(\nu\epsilon)$) as the model parameter. In addition the destruction term in the equation governing the dissipation rate is appropriately suppressed. It is important to say that instead of employing the total viscous dissipation rate ϵ as the scale-supplying variable, Launder and Sharma introduced the homogeneous dissipation rate $\tilde{\epsilon}$ ($= \epsilon - 2\nu(\partial\sqrt{k}/\partial x_l)(\partial\sqrt{k}/\partial x_l)$):

$$\frac{Dk}{Dt} = \frac{\partial k}{\partial t} + \overline{U}_j \frac{\partial k}{\partial x_j} = P_k - \tilde{\epsilon} - 2\nu \frac{\partial\sqrt{k}}{\partial x_l}\frac{\partial\sqrt{k}}{\partial x_l} + \frac{\partial}{\partial x_j}\left[\left(\nu + \frac{\nu_t}{\sigma_k}\right)\frac{\partial k}{\partial x_j}\right], \tag{2.12}$$

$$\begin{aligned}\frac{D\tilde{\epsilon}}{Dt} = \frac{\partial\tilde{\epsilon}}{\partial t} + \overline{U}_j \frac{\partial\tilde{\epsilon}}{\partial x_j} &= C_{\epsilon_1}\frac{P_k}{k}\tilde{\epsilon} - f_{\tilde{\epsilon}} C_{\epsilon_2}\frac{\tilde{\epsilon}^2}{k} + 2\nu\nu_t \frac{\partial^2\overline{U_i}}{\partial x_k \partial x_l}\frac{\partial^2\overline{U_i}}{\partial x_k \partial x_l} \\ &\quad + \frac{\partial}{\partial x_j}\left[\left(\nu + \frac{\nu_t}{\sigma_\epsilon}\right)\frac{\partial\tilde{\epsilon}}{\partial x_j}\right].\end{aligned} \tag{2.13}$$

$$f_\mu = \exp\left[-3.1/(1 + k^2/(50\nu\tilde{\epsilon}))^2\right], \quad f_{\tilde{\epsilon}} = 1.0 - 0.3\exp\left[-\left(\frac{k^2}{\nu\tilde{\epsilon}}\right)^2\right]$$

The final formulation of the turbulent viscosity reads

$$\nu_t = C_\mu f_\mu \frac{k^2}{\tilde{\epsilon}} \quad . \tag{2.14}$$

The model constants of the k-ϵ model are listed in Table (2.1)

2.1.2 k-ζ-f model

Instead of applying a damping function f_μ determined empirically within a 'trial-and-error' procedure, Durbin (1991, [13]) proposed a damping function based on the velocity scale represented by the normal-to-the-wall

Reynolds stress components $\overline{v^2}$, because this component is mostly affected by the near-wall anisotropy. He formulated a relevant transport equation governing the corresponding variable representing actually a scalar quantity. In this transport equation, he introduced the elliptic relaxation function f to integrate the pressure-strain term aiming at capturing the relevant near-wall effects without having to 'empirically' modify it when approaching the solid wall. Thus, the near-wall asymptotic behavior of all Reynolds stress components can be correctly captured.

Further, Hanjalić et al. (2004, [31]) reformulated the $\overline{v^2}$ equation by dividing it by the kinetic energy of turbulence k. By doing so they introduced the ratio of $\overline{v^2}$ to k (denoted by ζ). This formulation contributes significantly to the stabilization of the numerical procedure by weakening the model dependency on the wall distance y: the boundary condition for the elliptic function f was transformed from $f_{wall} \propto y^{-4}$ pertinent to the Durbin's $\overline{v^2}$-f model to $f_{wall} \propto y^{-2}$ pertinent to the k-ζ-f model.

The model formulation for the turbulent viscosity of the k-ζ-f model corresponds to

$$\nu_t = C_\mu^\zeta \zeta k T, \tag{2.15}$$

Following four transport equations are to be solved:

$$\frac{Dk}{Dt} = \frac{\partial k}{\partial t} + \overline{U}_j \frac{\partial k}{\partial x_j} = P_k - \epsilon + \frac{\partial}{\partial x_j}\left[\left(\nu + \frac{\nu_t}{\sigma_k}\right)\frac{\partial k}{\partial x_j}\right] \tag{2.16}$$

$$\frac{D\epsilon}{Dt} = \frac{\partial \epsilon}{\partial t} + \overline{U}_j \frac{\partial \epsilon}{\partial x_j} = \frac{1}{T}(C_{\epsilon_1} P_k - C_{\epsilon_2}\epsilon) + \frac{\partial}{\partial x_j}\left[\left(\nu + \frac{\nu_t}{\sigma_\epsilon}\right)\frac{\partial \epsilon}{\partial x_j}\right] \tag{2.17}$$

$$\frac{D\zeta}{Dt} = \frac{\partial \zeta}{\partial t} + \overline{U}_j \frac{\partial \zeta}{\partial x_j} = f - \frac{P_k}{k}\zeta + \frac{\partial}{\partial x_j}\left[\left(\nu + \frac{\nu_t}{\sigma_\zeta}\right)\frac{\partial \zeta}{\partial x_j}\right] \tag{2.18}$$

$$L^2 \nabla^2 f - f = \frac{1}{T}\left(c_1 + c_2 \frac{P_k}{\epsilon}\right)\left(\zeta - \frac{2}{3}\right) \tag{2.19}$$

In which, L and T are the turbulent length and time scales formulated in a way providing a switch between the integral turbulent properties and the Kolmogorov scales:

$$T = \max\left[\min\left(\frac{k}{\epsilon}, \frac{0.6}{\sqrt{6}C_\mu^\zeta |\overline{S}_{ij}|\zeta}\right), C_T\left(\frac{\nu}{\epsilon}\right)^{\frac{1}{2}}\right],$$

Table 2.2: Parameters of the RANS k-ζ-f model

C_μ^ζ	C_{ϵ_1}	C_{ϵ_2}	c_1	c_2	C_T	C_η	C_L	σ_k	σ_ϵ	σ_ζ
0.22	$1.4(1+0.045/\sqrt{\zeta})$	1.9	0.4	0.65	6	85	0.36	1	1.3	1.2

$$L = C_L \max\left[\min\left(\frac{k^{\frac{3}{2}}}{\epsilon}, \frac{\sqrt{k}}{\sqrt{6}C_\mu^\zeta |\overline{S}_{ij}|\zeta}\right), C_\eta\left(\frac{\nu}{\epsilon}\right)^{\frac{1}{4}}\right].$$

The model constants are listed in Table (2.2).

In this work, the k-ζ-f model is adopted as the reference RANS model mimicking the sub-scale model in both presently employed Hybrid LES/RANS methods PANS and VLES.

2.2 Large Eddy Simulation (LES)

Instead of utilizing the averaging technique, LES applies low wave number filtering, i.e. for the properties corresponding to the low wave number range, the features are captured directly, whereas the physical properties are estimated by the models in the high wave number region, see Fig 2.2(a). For the turbulent features, the filter width indicates the size of smallest resolved eddies and has the explicit dependency on the filter function. As it is introduced by Leonard (1975, [54]), the filtered variable $\tilde{\phi}$ is defined as

$$\tilde{\phi}(x) = \int \phi(x-\gamma)G(\gamma, x)d\gamma,$$

where the filter function $G(\gamma, x)$ satisfies the normalization condition:

$$\int G(\gamma, x)d\gamma = 1.$$

In regard to CFD applications, the sharp truncated filter is usually employed. This method assumes all the Fourier modes larger than the cutoff wavenumber (κ_c) having no effect on the low wavenumber modes. An illustration of the relevant turbulent energy spectrum is exemplarily displayed in Fig 2.2(b)

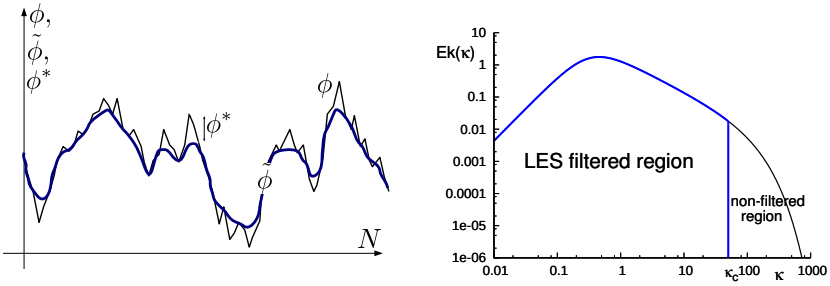

(a) Principle of LES filtering

(b) LES filtering on energy spectrum

Figure 2.2: Illustration of filtering principles

with the cutoff wavenumber κ_c defined as

$$\kappa_c = \frac{\pi}{\Delta},$$

where Δ represents the filter width being equivalent to the numerical grid size. In other words, the smallest filtered properties have the lengthscale identical to the applied grid size.

To derive the transport equations in the LES framework, the filter function provides the physical properties being decomposed into the filtered ($\widetilde{\phi}$) and residual parts (ϕ^*). Here, the principles of statistical averaging operations (pertinent to RANS method) are not valid at all. As it is shown in Eq 2.20, these decomposition method results in the necessity to model the residual properties.

$$\begin{aligned} \phi &= \widetilde{\phi} + \phi^*, \\ \widetilde{\phi^*} &\neq 0. \end{aligned} \tag{2.20}$$

Nevertheless, the governing equations in the LES mode take a form similar to that encountered within the RANS framework. Accordingly, the continuity and momentum equations based on the filtering principle for the incompressible, Newtonian fluid read:

$$\frac{\partial \widetilde{U}_i}{\partial x_i} = 0, \tag{2.21}$$

$$\frac{D\widetilde{U}_i}{Dt} = \frac{\partial \widetilde{U}_i}{\partial t} + \widetilde{U}_j \frac{\partial \widetilde{U}_i}{\partial x_j} = -\frac{1}{\rho}\frac{\partial \widetilde{p}}{\partial x_i} + \frac{\partial}{\partial x_j}\left(\nu \frac{\partial \widetilde{U}_i}{\partial x_j} - \widetilde{\tau}_{ij}\right). \tag{2.22}$$

where $\widetilde{\tau}_{ij}$ denotes the stress tensor associated with the residual motion,

$$\widetilde{\tau}_{ij} = \widetilde{U_i U_j} - \widetilde{U}_i \widetilde{U}_j \quad . \tag{2.23}$$

For a comprehensive overview, Leonard (1975, [54]) decomposed the residual stress tensor τ_{ij} into the combination of three contributions: Leonard, Cross and subgrid-scale Reynolds stress tensor.

$$\begin{aligned}
\widetilde{\tau}_{ij} &= L_{ij} + C_{ij} + R_{ij} \\
L_{ij} &= \widetilde{U}_i \widetilde{U}_j - \widetilde{\widetilde{U}_i \widetilde{U}_j} \\
C_{ij} &= \widetilde{u_i^* \widetilde{U}_j} + \widetilde{u_j^* \widetilde{U}_i} \\
R_{ij} &= \widetilde{u_i^* u_j^*}
\end{aligned}$$

The Leonard tensor (L_{ij}) is representative of the interaction among the large scales, which contains only the filtered velocity components. The cross tensor (C_{ij}) describes the interaction between the large and the small scales, and the subgrid-scale Reynolds stress tensor denotes the interaction among the non-filtered, unresolved scales, see Fig 2.3 .

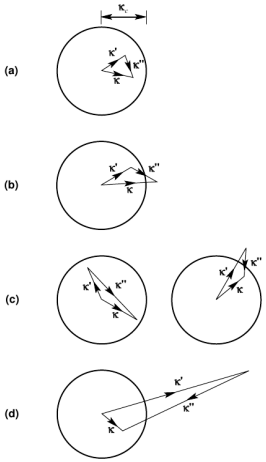

Figure 2.3: Illustrations of the turbulent stress contributions in LES mode[72], (a) Resolved, (b) Leonard, (c) Cross, (d) SGS Reynolds stress

2.2.1 Smagorinsky Subgrid-Scale Model

To evaluate the residual stress tensor $\widetilde{\tau}_{ij}$, Smagorinsky and Manabe (1962, [81]) assumed the equality between the turbulent production and the dissipation rate in the fine structure region according to the Kolmogorov hypothesis and proposed the first subgrid-scale model relying on the Prandtl's mixing length concept. Accordingly, a formulation of the subgrid scale turbulent viscosity (ν_u) has been proposed. Furthermore, Smagorinsky supposed the unresolved characteristic length scale being directly proportional to the filter width (corresponding conventionally to the grid spacing), and the velocity scale proportional to both the filter width and the 'filtered-velocity' gradient $\widetilde{S}_{ij}$. Thus, the representation of $\widetilde{\tau}_{ij}$ becomes:

$$\widetilde{\tau}_{ij} = -2\nu_t \widetilde{S}_{ij} + \tfrac{1}{3}\widetilde{\tau}_{kk}\delta_{ij}, \quad \widetilde{S}_{ij} = \frac{1}{2}\left(\frac{\partial \widetilde{U}_i}{\partial x_j} + \frac{\partial \widetilde{U}_j}{\partial x_i}\right),$$

Consequently, the subgrid scale turbulent viscosity(ν_u) takes the following form

$$\nu_u = (C_s\Delta)^2 \left|\widetilde{S}_{ij}\right|, \quad \left|\widetilde{S}_{ij}\right| = \left(2\widetilde{S}_{ij}\widetilde{S}_{ij}\right)^{\frac{1}{2}}, \tag{2.24}$$

Here, the numerical cell size(Δ) is adopted as the filter width, defined as the cube root of a cell volume ($(\Delta x \Delta y \Delta z)^{1/3}$). The Smagorinsky constant(C_s) is calibrated in accordance with satisfying the slope pertinent to the inertial sub-region of the turbulent spectra ($\kappa^{-5/3}$); accordingly, the constant C_s takes the values in the range between 0.1 and 0.2.

Since the fine structure turbulence is in equilibrium state ($P_u = \epsilon$), the applied grid spacing (Δ) should be adjusted to fulfill this assumption. In general, the filter width should have the same order as the lengthscale at the end of the inertial subrange, which corresponds to at least 80% of the resolved fraction of the energy spectrum (according to Pope, 2000, [72]; see also chapter 1.1).

If a too coarse mesh is applied (spectral cut-off is close to the productive region where $P_u < \epsilon$) the subgrid scale turbulent properties will be underestimated and the eddy structures obtained numerically will become less diffusive; as a characteristic outcome the energy spectrum slope within inertial subrange will be larger than $-5/3$, see Fig 2.4. It doesn't comply with the underlying physics of turbulence. Finally, there will be too many small vortices appearing in the computational domain, which do not correspond to the realistic picture of turbulence.

If the assumptions are satisfied the Smagorinsky SGS model is based upon, the subgrid scale turbulent kinetic energy (k_u) and dissipation rate

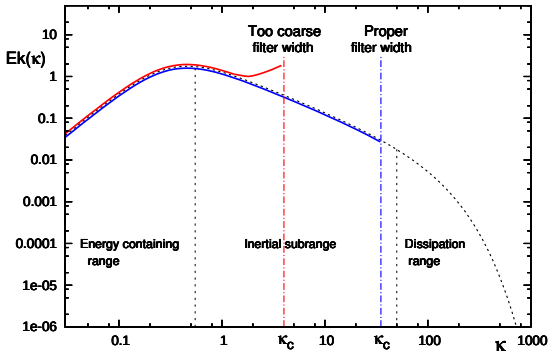

Figure 2.4: Influence of mesh resolution on the velocity fluctuation with respect to Smagorinsky relevant zero-equation LES models

(ϵ_u) can be correctly estimated. By analyzing the Smagorinsky LES model along with the one equation residual stress model suggested by Deardorf (1974, [12]), the subgrid scale turbulent kinetic energy can be estimated as

$$k_u = \left(\frac{C_s^2}{C_D}\right)^2 \Delta^2 \left|\widetilde{S}_{ij}\right|^2, \quad C_D = 0.1 \tag{2.25}$$

The residual dissipation rate (ϵ_u) is directly dependent on k_u and Δ. According to analysis given in [72], ϵ_u can be estimated by applying the Kolmogorov energy spectrum model:

$$\epsilon_u = \frac{C_E k_u^{3/2}}{\Delta}, \quad C_E = 0.9 \sim 1.1 \tag{2.26}$$

An interesting outcome arising from these formulations with respect to the turbulent length scale built up by the unresolved properties k_u and ϵ_u in Eq 2.26 is, that the largest modeled length scale ($k_u^{3/2}/\epsilon_u$) has the same order as the filter width; their ratio(C_E) tends towards unity.

$$\frac{k_u^{\frac{3}{2}}}{\epsilon_u} \backsimeq \Delta \tag{2.27}$$

2.3 RANS-based, Eddy-resolving Models of Turbulence

The fine spatial and temporal resolutions required by an LES method represent a big obstacle for its regular use in the industrial practice. It is especially the case with the high Reynolds number flow configurations, frequently encountered in industrial environment. In order to satisfy the conditions discussed previously when talking about the LES method and associated subgrid-scale models, appropriate numerical grid has to be generated. Accordingly thorough mesh studies for the grid convergence are necessary within the LES procedure. In the case of an industrially relevant complex geometry, this demand is strongly correlated with the high computational costs. Relevant highly resolved LES is difficult to achieve.

The basic purpose of developing the hybrid LES/RANS eddy-resolving turbulence models is to compensate these shortcomings by applying transport equations also for solving the residual turbulent properties (we recall the zero-equation subgrid-scale models applied conventionally in the LES framework). The (correspondingly) large scale flow structures are resolved by solving the momentum equation (similar as in LES), but the subgrid scales, or in general sub-scale turbulent properties are estimated by utilizing a RANS-based turbulence model. The structural properties of the latter models are on a much higher level compared to conventional LES-related SGS models. Accordingly, in the case of coarser grid resolutions corresponding to the spectral cut-off situated in the sub-inertial region pertinent to the lower frequency range (even in the productive region of the energy spectrum) such a model can much better mimics the relevant flow properties not resolved by the grid used. The mathematical background of RANS-based eddy-resolving models is the same as LES: the physical properties are also filtered by an appropriate filter function. In the 'critical' flow regions meshed by a grid being too coarse for a conventional LES, as e.g. in the near-wall regions, higher fraction of the modeled turbulence is expected; in accordance with the previous discussion, a RANS-based sub-scale model can better cope with such circumstances.

Regarding the underlying transport equations, hybrid eddy-resolving models have very similar equation structure as in the RANS framework, however the procedure of making them adaptive to finally describe the residual turbulence pertinent to the given eddy-resolving method can be very different. In general, according to the underlying fluctuating velocity field, the intensity of unresolved turbulent quantities estimated by a

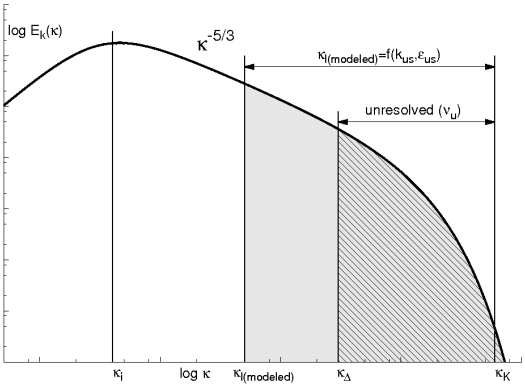

Figure 2.5: General challenge of hybrid turbulence modeling, gray region: turbulent properties modeled by RANS in unsteady mode (subscript: us), slashed region: the subgrid scale properties (subscript: u)

RANS-based sub-scale model is usually higher than the one which would be obtained by an LES subgrid-scale model (see Fig 2.5). It is in accordance with a correspondingly larger filter width compared to the one which is defined only by the grid size. Accordingly, the dependency of numerical results on the grid resolution is not explicit as it would be the case with an LES method. The hybrid LES/RANS methods aim finally at operating with larger filter widths. The correct representation of the turbulent flow field can be obtained despite a large filter width.

2.3.1 Partially Averaged Navier-Stokes (PANS) Approach

The PANS method is proposed by Girimaji (2006, [22]). He assumed that the subgrid scale turbulent properties are analog to those captured in a RANS framework. He proposed a RANS model modification to account for the residual stress coping with the grid applied. Accordingly, he introduced the ratios of unresolved-to-total turbulent kinetic energy (f_k) and unresolved-to-total dissipation rate (f_ϵ):

$$k_u = f_k k, \tag{2.28}$$

$$\epsilon_u = f_\epsilon \epsilon. \tag{2.29}$$

The unresolved turbulent properties are governed by the equations taking the same basic form as in the standard k-ϵ model. The resulting transport equations of the unresolved, subgrid scale turbulent kinetic energy and dissipation rate read:

$$\frac{Dk_u}{Dt} = f_k \frac{Dk}{Dt} = f_k \left(P_k - \epsilon\right) + f_k \frac{\partial}{\partial x_j}\left[\left(\nu + \frac{\nu_t}{\sigma_k}\right)\frac{\partial k}{\partial x_j}\right],$$

$$\frac{D\epsilon_u}{Dt} = f_k \frac{D\epsilon}{Dt} = f_\epsilon \left(C_{\epsilon 1}\frac{P_k}{k\epsilon} - C_{\epsilon 2}\frac{\epsilon^2}{k}\right) + f_\epsilon \frac{\partial}{\partial x_j}\left[\left(\nu + \frac{\nu_t}{\sigma_\epsilon}\right)\frac{\partial \epsilon}{\partial x_j}\right].$$

Here, it was assumed that the production (P_u) and destruction (ϵ_u) terms (pertinent to the unresolved turbulence) in the transport equation of k_u are equivalent to their difference multiplied by f_k within the RANS framework. Thus,

$$P_u - \epsilon_u = f_k \left(P_k - \epsilon\right), \tag{2.30}$$

and

$$P_u = 2\nu_u \left|\widetilde{S}_{ij}\right| \left|\widetilde{S}_{ij}\right|, \quad \widetilde{S}_{ij} = \frac{1}{2}\left(\frac{\partial \widetilde{U}_i}{\partial x_j} + \frac{\partial \widetilde{U}_j}{\partial x_i}\right)$$

Hence, the transport equations of k_u and ϵ_u have the form similar to that encountered in the RANS framework:

$$\frac{Dk_u}{Dt} = \frac{\partial k_u}{\partial t} + \widetilde{U}_j \frac{\partial k_u}{x_j} = P_u - \epsilon_u + \frac{\partial}{\partial x_j}\left[\left(\nu + \frac{\nu_t}{\sigma_k^*}\right)\frac{\partial k_u}{\partial x_j}\right], \tag{2.31}$$

$$\frac{D\epsilon_u}{Dt} = \frac{\partial \epsilon_u}{\partial t} + \widetilde{U}_j \frac{\partial \epsilon_u}{\partial x_j} = C_{\epsilon_1}\frac{P_u}{k_u}\epsilon_u - C^*_{\epsilon 2}\frac{\epsilon_u^2}{k_u} + \frac{\partial}{\partial x_j}\left[\left(\nu + \frac{\nu_t}{\sigma_{\epsilon^*}}\right)\frac{\partial \epsilon_u}{\partial x_j}\right]. \tag{2.32}$$

The key issue here is the modification of the model coefficient multiplying the destruction term in the dissipation rate equation,

$$C^*_{\epsilon 2} = C_{\epsilon 1} + \frac{f_k}{f_\epsilon}\left(C_{\epsilon 2} - C_{\epsilon 1}\right) \tag{2.33}$$

Accordingly, the unresolved, subgrid scale turbulent viscosity is formulated as follows

$$\nu_u = C_\mu \frac{k_u^2}{\epsilon} \tag{2.34}$$

Aiming at determination of the parameter σ_k^* and σ_ϵ^* appearing in the diffusion coefficients in both k_u and ϵ_u equations, Girimaji et al. (2003, [23])

introduced the concept of zero transport(ZT) and maximal transport(MT) to describe the relevant diffusion rates. For the situations, in which the resolved fluctuation does not contribute to the residual energy transport, ZT is defined as:

$$\sigma_k^* = \sigma_k \frac{f_k^2}{f_\epsilon}, \qquad \sigma_\epsilon^* = \sigma_\epsilon \frac{f_k^2}{f_\epsilon};$$

The maximal transport(MT) assumes that the transport is proportional to eddy viscosity of resolved fluctuation, i.e.

$$\sigma_k^* = \sigma_k, \quad \sigma_\epsilon^* = \sigma_\epsilon$$

Principally, the partially-averaged method represents a seamless bridging technique from RANS to DNS depending on the ratio f_k and f_ϵ. For $f_k, f_\epsilon \to 1$, RANS dominates in the computational domain; the equations governing the residual properties (denoted by subscript u) reduce to those governing the fully-modeled turbulence; all model parameters are consistent with those of the RANS methodology; here, the principles of the statistical averaging apply. In contrast, if $f_k \to 0$, the modeled turbulence fraction vanishes entirely due to the significantly reduced $C_{\epsilon 2}^*$ coefficient becoming finally equal to $C_{\epsilon 1}$; the equation system corresponds to the DNS principles.

Accordingly, the crucial element in the PANS framework is the determination of the ratios f_k and f_ϵ. Expectedly, if the cutoff wavenumber lays within the inertial sub-range, the subgrid scale dissipation rate (ϵ_u) is equal to the total dissipation rate (ϵ) according to the hypothesis of Kolmogorov (1991, [45]), i.e. f_ϵ can be regarded as unity.

For the determination of f_k, different options were published in the last years. Schiestel and Dejoan (2005, [77]) defined this parameter in the framework of their PITM method by applying the concept of Kolmogorov energy spectrum, and summarized the approximation of f_k as:

$$f_k \approx \frac{3}{2} C_K \left(\frac{\pi \Lambda}{\Delta} \right)^{-2/3}, \tag{2.35}$$

where C_K represents the Kolmogorov constant taking the value of 1.5 [72] and Λ is the integral turbulent lengthscale:

$$\Lambda = \frac{k^{3/2}}{\epsilon}.$$

Girimaji and Abdol-Hamid (2005, [24]) assumed that the smallest resolved lengthscale (corresponding to the representative grid spacing Δ)

should be proportional to the Kolmogorov lengthscale based on subgrid scale turbulent viscosity:

$$\Delta \approx \left(\frac{\nu_u^3}{\epsilon}\right)^{\frac{1}{4}} = \left[\frac{\left(C_\mu f_k^2 k^2/\epsilon\right)^3}{\epsilon}\right]^{1/4}.$$

Finally f_k is formulated as

$$f_k = \frac{1}{\sqrt{C_\mu}}\left(\frac{\Delta}{\Lambda}\right)^{\frac{2}{3}}. \tag{2.36}$$

Furthermore, the PANS concept is extended by utilizing the k-ω model of turbulence as the background model, see e.g. [48]. In the PITM framework, a subgrid scale model based on the differential Reynolds stress model has also been applied (see e.g., [10], [77] and [17]) to account for the complex physical details. Finally, Basara et al.(2011, [5]) applied the principle of the PANS methodology to the k-ζ-f model to better account for the near-wall turbulence phenomena. By deriving the relevant equation governing the ζ_u quantity, the dependency on the resolution parameter f_k is preserved. This model formulation reads:

$$\frac{Dk_u}{Dt} = \frac{\partial k_u}{\partial t} + \widetilde{U}_j\frac{\partial k_u}{\partial x_j} = P_u - \epsilon_u + \frac{\partial}{\partial x_j}\left[\left(\nu + \frac{\nu_u}{\sigma_k^*}\right)\frac{\partial k_u}{\partial x_j}\right], \tag{2.37}$$

$$\frac{D\epsilon_u}{Dt} = \frac{\partial \epsilon_u}{\partial t} + \widetilde{U}_j\frac{\partial \epsilon_u}{\partial x_j} = C_{\epsilon_1}\frac{P_u}{k_u}\epsilon_u - C_{\epsilon_2}\frac{\epsilon_u^2}{k_u} + \frac{\partial}{\partial x_j}\left[\left(\nu + \frac{\nu_u}{\sigma_\epsilon^*}\right)\frac{\partial \epsilon_u}{\partial x_j}\right]. \tag{2.38}$$

$$\frac{D\zeta_u}{Dt} = \frac{\partial \zeta_u}{\partial t} + \widetilde{U}_j\frac{\partial \zeta_u}{\partial x_j} = f_u - \frac{P_u}{k_u}\zeta_u + \frac{\zeta_u}{k_u}\epsilon_u\left(1 - f_k\right) + \frac{\partial}{\partial x_j}\left[\left(\nu + \frac{\nu_u}{\sigma_\zeta^*}\right)\frac{\partial \zeta_u}{\partial x_j}\right], \tag{2.39}$$

$$L_u^2\nabla^2 f_u - f_u = \frac{1}{\tau_u}\left(c_1 + c_2\frac{P_u}{\epsilon_u}\right)\left(\zeta_u - \frac{2}{3}\right). \tag{2.40}$$

$$T_u = \max\left[\frac{k_u}{\epsilon_u}, C_\tau\left(\frac{\nu}{\epsilon_u}\right)^{\frac{1}{2}}\right], \quad L_u = C_L\max\left[\frac{k_u^{1.5}}{\epsilon_u}, C_\eta\left(\frac{\nu^3}{\epsilon_u}\right)^{\frac{1}{4}}\right]. \tag{2.41}$$

Table 2.3: Parameters of PANS-k-ζ-f model

C_μ^ζ	c_1	c_2	C_T	C_η	C_L	σ_k	σ_ϵ	σ_ζ
0.22	0.4	0.65	6	50	0.36	1	1.3	1.2

in which ,

$$C_{\epsilon 1} = 1.4\left(1 + 0.045/\sqrt{\zeta_u}\right), \quad C^*_{\epsilon 2} = C_{\epsilon 1} + f_k\left(C_{\epsilon 2} - C_{\epsilon 1}\right).$$
$$\sigma_k^* = \sigma_k f_k^2, \quad \sigma_\epsilon^* = \sigma_\epsilon f_k^2, \quad \sigma_\zeta^* = \sigma_\zeta f_k^2,$$

The expression for the subgrid scale turbulent viscosity takes the following form

$$\nu_u = C_\mu^\zeta \zeta_u k_u^2/\epsilon_u.$$

The grid resolution parameter f_k (Eq 2.36) is formulated by applying the k-ζ-f model as follows:

$$f_k = \frac{1}{\sqrt{C_\mu^\zeta \zeta}}\left(\frac{\Delta}{\Lambda}\right)^{\frac{2}{3}}, \tag{2.42}$$

where Λ is the integral lengthscale, consisting of the resolved ($_{\mathrm{res}}$) and modeled ($_{\mathrm{u}}$) turbulent kinetic energy (and the corresponding dissipation rate), see Eq 2.43. Here, the information of the resolved turbulent kinetic energy (k_{res}) is evaluated in the framework of the time-averaging (in the case of the steady mean flow) or the phase-averaging (pertinent to the periodically unsteady mean flow as in the case of internal combustion engines) procedure during the calculation:

$$\Lambda = \frac{\left(k_{\mathrm{res}} + k_u\right)^{\frac{2}{3}}}{\epsilon_u} \qquad k_{\mathrm{res}} = \frac{1}{2}\left(\widetilde{U}_i - \overline{U}_i\right)^2 \tag{2.43}$$

The parameters of the PANS computational scheme based on the k-ζ-f model of turbulence are summarized in Table (2.3).

In the present work, the thorough validation of the PANS method is carried out by computing flow configurations of different complexity to demonstrate its predictive capabilities.

2.3.2 Very Large Eddy Simulation (VLES)

Instead of modifying the modeling parameters in the transport equations of the subgrid scale turbulent properties, the concept of the VLES computational strategy is to handle appropriately the turbulent viscosity in the momentum equation directly. This methodology is first proposed by Speziale (1998, [83]), who suggested to apply the fully-modeled Reynolds stress tensor but multiplied by a build-in function F_r to adjust the filtering concept to the eddy-resolving methodology. Accordingly, the Reynolds stress, estimated within the RANS framework, is suppressed by the filter function F_r as follows

$$\widetilde{\tau}_{ij} = F_r \tau_{ij}^{\mathrm{RANS}},$$

with

$$F_r = \left[1.0 - \exp\left(\frac{-\delta\Delta}{\eta}\right)\right]^n.$$

Here, δ and n are unspecified parameters, Δ and η are the representative grid spacing and the Kolmogorov lengthscale.

For $\Delta/\eta \to 0$, F_r tends to 0; all relevant scales are resolved, and the modeled stresses take zero values approaching the DNS concept. If $\Delta/\eta \to \infty$, F_r approaches 1 and the VLES method reduces to the RANS method in the entire computational domain. This concept has been followed further by Fasel et al. (2003, [18]) and Magnient et al. (2001, [60]). Furthermore, Han and Krajnović (2012, [28]) validated the original formulation proposed by Speziale. In their work, they found that the numerical realizations are too diffusive and suggested the F_r function being determined by applying following expression

$$F_r = \left[1.0 - \exp\left(\frac{-\delta\Delta}{\eta}\right)\right]^n \Big/ \left[1.0 - \exp\left(\frac{-\delta\Lambda_{us}}{\eta}\right)\right]^n, \tag{2.44}$$

where $\Lambda_{us} = k_{us}^{3/2}/\epsilon_{us}$ is the lengthscale defined by the turbulent kinetic energy k_{us} and dissipation rate ϵ_{us} calculated from the corresponding transport equations. The subscript '$_{us}$' relates to the Unsteady RANS flow field. By applying Taylor series expansion to Eq 2.44, F_r can be approximated as

$$F_r \to \left(\frac{\Delta}{\Lambda}\right)^n. \tag{2.45}$$

Here n is the exponent taking different values in the published literature, for instance $n = 4/3$ in Magnient et al. (2001, [60]) and Langhe et al. (2005, [50]) and $n = 2$ in Peltier and Zajaczkowski (2001, [70]).

Concerning the reproduction of eddy structures resolved by computing corresponding momentum equation, the diffusion term plays a crucial role in determining the level of turbulence fluctuations. In the LES mode, a sharp truncated filtering function defines that the smallest resolved length-scale should be equal to the numerical grid size. Accordingly, a question arises, how large should be the modeled lengthscale, providing the smallest lengthscales being equal to the underlying grid spacing?

This issue has been discussed in Chumakov (2007, [11]), Ghosal et al. (1995, [21]) and Johansen et al. (2004,[39]). Johansen et al. (2004, [39]) assumed that the subgrid scale turbulent kinetic energy (k_u) and its dissipation rate (ϵ_u) build identical properties as the Smagorinsky LES model if the requirements towards the mesh resolution in LES mode are fulfilled. A parameter χ is defined, representing the ratio of the grid spacing (Δ) to the modeled (unresolved) subgrid lengthscale ($\Lambda_u = k_u^{3/2}/\epsilon_u$), according to the following formulation

$$\chi = \frac{\Delta}{\Lambda_u} = \sqrt{0.3}\frac{C_s}{C_\mu}, \quad C_\mu = 0.09 \quad \text{(pertinent to a } \; k\text{-}\epsilon \text{ model formulation).} \tag{2.46}$$

Lilly (1967, [56]) applied the sharp spectral LES filter to simulating the homogeneous isotropic turbulence. Under the assumption that $\overline{S^3} \approx (\overline{S^2})^{\frac{2}{3}}$, the Smagorinsky constant C_s takes the value 0.17. Applying this value to Eq 2.46, χ becomes close to unity. This corresponds to Eq 2.27 and is approved by Schumann (1975, [78]), Yoshizawa (1985, [98]) and Johansen et al. (2004, [39]).

Extending this conclusion, the ratio of subgrid scale turbulent properties to the ones estimated by a RANS-related model in conjunction with the fluctuated flow field, can be assumed by adopting the resolution parameters analog to those defined within the PANS framework:

$$k_u = F_k k_{us}, \quad \epsilon_u = F_\epsilon \epsilon_{us},$$

Since χ is approximately close to 1, and the ratio of the subgrid scale dissipation rate to the total one (ϵ_u/ϵ) can be taken as unity if the cutoff lays in inertial sub-range, the formulation of F_k can be derived from

$$\Delta = \frac{k_u^{3/2}}{\epsilon_u} = \frac{(F_k k_{us})^{3/2}}{F_\epsilon \epsilon_{us}}, \quad F_\epsilon = 1.$$

Thus,

$$F_k = \left(\frac{\Delta}{\Lambda_{us}}\right)^{2/3}, \quad \text{and} \quad F_r = F_k^2 = \left(\frac{\Delta}{\Lambda_{us}}\right)^{4/3}. \tag{2.47}$$

In the flow regions where the modeled lengthscale (Λ_{us}) is smaller than the grid spacing, the filter function F_k cannot be larger than 1; it implies that actually the RANS formulation of ν_u will be applied. Such circumstances can appear, for instance, in the near-wall region, where the prescribed filter width is not appropriately fine to resolve the flow field. But, the utilization of a sophisticated RANS model can cope successfully with this problem.

This built-in, filter function (F_r) represents in a certain sense the explicit scaling of the turbulent properties according to the ratio of the modeled lengthscale to the filter width. Concerning the filtering principles in general, the lengthscale has significant influence on the computationally captured eddy structures: for lengthscales originating from the momentum equation being larger than the filter width, too diffusive numerical representation can be the consequence, i.e. the smallest eddies are much smaller than they should be. In the VLES concept, the introduction of the built-in function corrects such a behavior by suppressing the modeled turbulent lengthscale towards the representative grid-spacing Δ. Once the turbulent stress tensor in the momentum equation is appropriately suppressed, the eddy structures can be properly resolved.

The estimation of modeled turbulent properties is done by using the RANS-based model equations, i.e. the computational results depend strongly on the employed RANS model. For the purpose of capturing correctly the near-wall phenomena (and for the possibility to directly compare the VLES results with those obtained by the RANS and PANS methods, using k-ζ-f model as the background model) k-ζ-f model is here also adopted as the underlying RANS model formulation. Accordingly, the transport equation system valid in VLES, based on the k-ζ-f model reads:

$$\frac{Dk_{us}}{Dt} = \frac{\partial k_{us}}{\partial t} + \widetilde{U}_j \frac{\partial k}{\partial x_j} = P_{us} - \epsilon_{us} + \frac{\partial}{\partial x_j}\left[\left(\nu + \frac{\nu_u}{\sigma_k}\right)\frac{\partial k_{us}}{\partial x_j}\right], \tag{2.48}$$

$$\frac{D\epsilon_{us}}{Dt} = \frac{\partial \epsilon_{us}}{\partial t} + \widetilde{U}_j \frac{\partial \epsilon_{us}}{\partial x_j} = \frac{1}{T_{us}}(C_{\epsilon_1} P_{us} - C_{\epsilon_2}\epsilon_{us}) + \frac{\partial}{\partial x_j}\left[\left(\nu + \frac{\nu_u}{\sigma_\epsilon}\right)\frac{\partial \epsilon_{us}}{\partial x_j}\right]. \tag{2.49}$$

$$\frac{D\zeta_{us}}{Dt} = \frac{\partial \zeta_{us}}{\partial t} + \widetilde{U}_j \frac{\partial \zeta_{us}}{\partial x_j} = f_{us} - \frac{P_{us}}{k_{us}}\zeta_{us} + \frac{\partial}{\partial x_j}\left[\left(\nu + \frac{\nu_u}{\sigma_\zeta}\right)\frac{\partial \zeta_{us}}{\partial x_j}\right], \quad (2.50)$$

$$L_{us}^2 \nabla^2 f_{us} - f_{us} = \frac{1}{T_{us}}\left(c_1 + c_2 \frac{P_{us}}{\epsilon_{us}}\right)\left(\zeta_{us} - \frac{2}{3}\right). \quad (2.51)$$

with P_{us} defined in terms of the unresolved eddy viscosity ν_u,

$$P_{us} = 2\nu_u \left|\widetilde{S}_{ij}\right| \left|\widetilde{S}_{ij}\right| \quad F_r = \min\left[1, \left(\frac{\Delta}{\Lambda_{us}}\right)^{4/3}\right].$$

The unresolved, residual turbulent viscosity is finally formulated as

$$\nu_u = F_r C_\mu^\zeta \zeta k_{us} T_{us}, \quad (2.52)$$

The corresponding time and length scale switches are formulated as follows

$$T_{us} = \max\left[\frac{k_{us}}{\epsilon_{us}}, C_\tau \left(\frac{\nu}{\epsilon_{us}}\right)^{\frac{1}{2}}\right], \quad L_{us} = C_L \max\left[\frac{k_{us}^{\frac{3}{2}}}{\epsilon_{us}}, C_\eta \left(\frac{\nu^3}{\epsilon_{us}}\right)^{\frac{1}{4}}\right].$$

The model constants are identical to those pertinent to the RANS k-ζ-f model and are summarized in Table (2.2).

3 Numerical Procedure

A numerical approach is employed to solve the equation system obtained in the previous chapter. Since the governing phenomena are all described by 2^{nd} order partial differential equations, exact solutions cannot be obtained in general. Nevertheless, solutions can be approached by utilizing numerical methods. Due to progressing computational technology, the numerical procedure can be employed under affordable costs. In general, Finite Volume Method (FVM) is the most commonly applied methodology when dealing with fluid dynamical problems. Hence, numerical handling of partial differential equation system is addressed in this chapter.

Finite Volume Method (FVM)

The principle of FVM is to discretized the solution domain into various control volumes. Each of the control volume obtains its own physical properties, which results in a complex matrix system for the whole domain. By solving the matrix system with respect to the governing equations, the properties of every control volume are obtained. A general transport equation for the scalar variable ϕ is given by the time derivative term(T), convection term(C), source term(S) and diffusion term(D) as follows

$$\underbrace{\int_{\delta V} \frac{\partial \phi}{\partial t} dV}_{T} + \underbrace{\int_{\delta V} u_i \frac{\partial \phi}{\partial x_i} dV}_{C} = \underbrace{\int_{\delta V} f dV}_{S} + \underbrace{\int_{\delta V} \frac{\partial}{\partial x_i} \left(\alpha \frac{\partial \phi}{\partial x_i} \right) dV}_{D},$$

where ∂V denotes the volume of each control volume, and α is the diffusion constant, e.g. the viscosity of a Newtonian fluid, the heat conductivity, etc.

By applying the Gauss's theorem, the convective (C) and diffusive (D) terms are transformed from the volume integral to a surface integral. Thus, the transport equation can be written as

$$\underbrace{\int_{\delta V} \frac{\partial \phi}{\partial t} dV}_{T} + \underbrace{\int_{\delta S} \phi u_i n_i dS}_{C} = \underbrace{\int_{\delta V} f dV}_{S} + \underbrace{\int_{\delta S} \left(\alpha \frac{\partial \phi}{\partial x_i} \right) n_i dS}_{D}, \tag{3.1}$$

where δS denotes the surfaces of the control volume. For the numerical procedure, every characterized term (T,C,S,D) is handled separately.

3.1 Temporal Discretization

The general handling of time derivation is summarized by the Runge-Kutta method of the order m. This method is also categorized in explicit and implicit treatment. For the explicit method, the value of the next time step is calculated as a function of the previous and the current time step, while the implicit method solves the matrix system by applying future time steps and values.

Taking into account a time-dependent variable ϕ being known as a function $\Psi(t, \phi)$, where ϕ takes the value ϕ_n according to the time step t_n, the Runge-Kutta method of m^{th} order approximates ϕ at the time t_{n+1} as follows:

$$\phi_{n+1} = \phi_n + \sum_{i=1}^{m} b_i K_i,$$

where

$$K_i = \Psi \left(t_n + c_i \Delta t, \phi_n + \sum_{j=0}^{m} a_{ij} K_j \right) \Delta t.$$

The parameters a_{ij}, b_i, c_i are defined in the so-called Butcher's array.

c_1	a_{11}	a_{12}	$\dots$	a_{1m}		c_1	0				
c_2	a_{21}	a_{22}	$\dots$	a_{2m}		c_2	a_{21}	0			
c_3	a_{31}	a_{32}	$\dots$	a_{3m}		c_3	a_{31}	a_{32}			
$\vdots$	$\vdots$	$\vdots$	$\ddots$	$\vdots$		$\vdots$	$\vdots$	$\ddots$	$\ddots$	$\ddots$	
c_m	a_{m1}	a_{m2}	$\dots$	a_{mm}		c_m	a_{m1}	a_{m2}	$\dots$	a_{mm-1}	0
	b_1	b_2	$\dots$	b_m			b_1	b_2	$\dots$	b_{m-1}	b_m

Table 3.1: Butcher's array of implicit(left) and explicit(right) Runge-Kutta method

The explicit method takes the left-down triangle of Butcher's array and leaves the rest to 0, see Table (3.1)(right), which implies that the values of future time steps are not taken into consideration. The implicit method, on the other hand, takes the whole matrix into account and the solution

is obtained by solving the matrix system over previous, current and future time steps. Thus, the computational cost increases considerably.

Time derivative methods for commercial applications

Within the frame of CFD, the most frequently applied methods are the Euler explicit and implicit scheme. These belong to the simplest formulation of the Runge-Kutta method of the order one. With respect to Table (3.1) for explicit Runge-Kutta of the first order, the explicit Euler method is written as

$$\phi_{n+1} = \phi_n + \Delta t \Psi(t, \phi_n),$$

whereas the implicit method, also called Euler backwards, has the representation

$$\phi_{n+1} = \phi_n + \Delta t \Psi(t, \phi_{n+1}).$$

Apart from the first order implicit and explicit Euler method, the Crank-Nicolson method is also utilized in CFD applications. This method employs the features of both Euler forwards and backwards methods and is defined as a second order time derivative method according to

$$\phi_{n+1} = \phi_n + \Delta t \left(\frac{1}{2} \Psi(t, \phi_{n+1}) + \frac{1}{2} \Psi(t, \phi_n) \right).$$

Euler forwards, Euler backwards and Crank-Nicolson have the corresponding Butcher's arrays shown in Table (3.2).

0	
	1

1	1
	1

0	0	0
1	1/2	1/2
	1/2	1/2

Table 3.2: Implicit(left), explicit(middle) Euler and Crank-Nicolson(right) time derivative method

From the perspective of numerical simulation, the Euler backwards method delivers a more accurate solution compared to the explicit method. Additionally, the time step size of implicit methods is not restricted by the Courant number, which is thus more suited for the application to complex calculation systems.

3.2 Discretization of Convective and Diffusive Terms

The numerical handling of convective and diffusive terms is categorized by the concept of flux, see Eq 3.1. Considering one single control volume in a two-dimensional domain, see Fig 3.1, the flux is integrated over all the faces, thus yielding

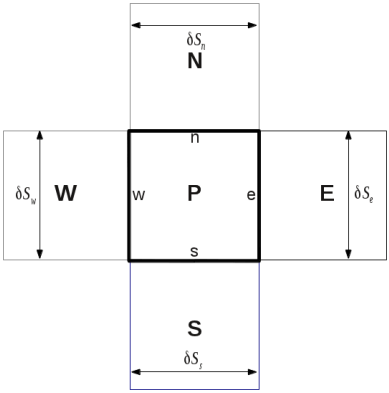

Figure 3.1: A two-dimensional control volume

$$\int_{\partial S} \left(u_i \phi - \alpha \frac{\partial \phi}{\partial x_i} \right) n_i dS = \sum_f u_i \phi_f n_f \delta S_f - \sum_f \alpha \left(\frac{\partial \phi}{\partial x_i} \right)_f n_f \delta S_f, \tag{3.2}$$

where f denotes the faces (e, w, n, s) of the considered cell.

3.2.1 Convective Flux

The numerical procedure regarding the convective flux focuses on two subjects: the determination of variables on the surface of the control volume and the handling of mesh deformation.

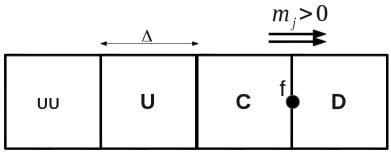

Figure 3.2: Illustrated one-dimensional control volumes. For the value of face f, the cells are taken for Upstream (U), Center(C), Downstream (D)

Interpolation scheme

To determine the value of the variable ϕ on the cell surface f, different interpolation schemes can be applied. Among these, the most-known are the Upwind Differencing Scheme (UDS) and the Central Differencing Scheme (CDS); the latter represent a linear interpolation method. The combination of these two schemes in a form of a blending scheme, with the basic schemes being differently weighted, is a most-widely used hybrid scheme in an engineering practice. UDS is the simplest interpolation method, which detects the mass flow direction and takes the values from the upstream node. Considering the illustrated one-dimensional uniform control volumes as shown in Fig 3.2, the value ϕ defined by UDS on the surface f is formulated as:

$$\begin{aligned} \phi_f &= \phi_C \quad \dot{m}_f > 0, \\ \phi_f &= \phi_D \quad \dot{m}_f < 0. \end{aligned}$$

Since ϕ_f is defined by the information of only one cell, UDS is categorized as a first order method.

Compared to UDS, CDS is a second order interpolation method which takes the information of both upstream and downstream nodes into account. With respect to the cells shown in Fig 3.2, CDS has the representation of

$$\phi_f = 0.5(\phi_C + \phi_D),$$

where 0.5 is used due to the uniform grid size.

In general, CDS yields a more accurate solution than UDS due to its 2^{nd} order interpolation character. However, it can also lead to numerical instability. As mentioned in [3], CDS can generate numerical oscillations and yield unbounded and non-monotonic solutions.

Blending Factor

To overcome potential stability problems, a linear combination of both CDS and UDS solutions is usually applied. Therefore, the blending factor β is defined as the fraction of CDS results. The solution is then given by:

$$\phi_f = \phi_f^{\mathrm{UDS}} + \beta(\phi_f^{\mathrm{CDS}} - \phi_f^{\mathrm{UDS}}), \quad 0 < \beta < 1.$$

For $\beta = 1$, CDS is applied, while pure UDS is used if $\beta = 0$.

Higher Order Linear Interpolation Schemes

Higher order linear interpolation schemes are usually applied for the combination of limited differencing methods, which take the value of upstream(U), center(C) and downstream(D) into consideration. The most general formulation of the higher order differencing method for the one-dimensional uniform control volumes shown in Fig 3.2 can be written as

$$\phi_f = \phi_c + \frac{1}{2}\left[(\frac{3}{4} - \psi)(\phi_D - \phi_C) + (\frac{1}{4} + \psi)(\phi_C - \phi_U)\right]. \tag{3.3}$$

Linear Upwind Differencing Scheme (LUDS) is a second order interpolation method, where the parameter ψ is defined as 3/4. This method uses the value of two cells in the upstream direction and linearly interpolates to the respective surface, thus yielding

$$\phi_f^{\mathrm{LUDS}} = \phi_C + 0.5(\phi_C - \phi_U), \quad \text{for} \quad \dot{m}_j < 0.$$

For Quadratic Upwind Interpolation for Convective Kinematics (QUICK), ψ is defined as 0. This method uses the information of all three cells and weights to estimate the value on the concerning surface, therefore being regarded a 3^{rd} order interpolation method.

$$\phi_f^{\mathrm{QUICK}} = \phi_C + 0.5[0.75(\phi_D - \phi_C) + 0.25(\phi_C - \phi_U)], \quad \text{for} \quad \dot{m}_j < 0.$$

Non-linear interpolation schemes

The idea of non-linear interpolation schemes is to apply limiters to bound the solution field in a realistic range. Therefore, a limiter function γ is defined by applying the variable in the upstream (U), center (C) and downstream (D) cell in Fig 3.2 as:

$$\gamma = \frac{\phi_D - \phi_C}{\phi_C - \phi_U}. \tag{3.4}$$

The interpolated solution depending on γ can be written as

$$\phi_f = \phi_C + 0.5\Phi(\gamma)(\phi_C - \phi_U),$$

where Φ is a function of γ and is defined differently in each limited scheme. Among all the limited schemes, MINMOD and SMART are the most commonly applied methods. These methods bound the solution between CDS, LUDS, QUICK and UDS. The limiter of MINMOD and SMART are defined as

$$\Phi(\gamma) = \max[0, \min(\gamma, 1)] \qquad \text{MINMOD}$$

$$\Phi(\gamma) = \max[0, \min(2\gamma, 0.75\gamma + 0.25, 4)] \qquad \text{SMART}$$

For MINMOD, UDS is applied for $\Phi = 0$, the solution thus being 1^{st} order accurate. If $\Phi = 1$, LUDS dominates the solution, and pure CDS is applied for $\Phi = \gamma$.

SMART bounds the solution field between UDS($\Phi = 0$), QUICK($\Phi = 0.75\gamma + 0.25$) and Downwind method($\Phi = 2\gamma$). The graphical representations of both methods are shown in a normalized variable diagram in Fig 3.3.

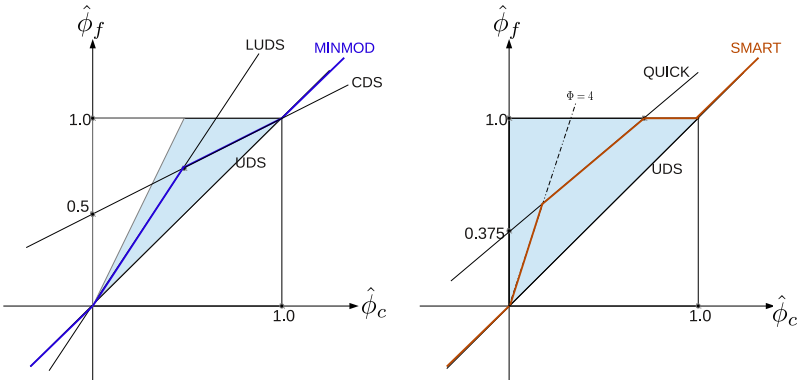

Figure 3.3: Normalized variable diagram of MINMOD (left) and SMART (right) method

Handling of mesh deformation

For cases where the numerical mesh is moving, i.e. the control volume deforms, the convective flux is the only term that needs to be considered additionally. Regarding a single cell shown in Fig 3.1, the flux of the cell surface should be considered as the relative velocity to the mesh movement. Thus, the convective flux has the representation of

$$\sum_f \phi \left(u_i - u_{Mi}\right) n_f \delta S,$$

where u_{Mi} denotes the mesh movement velocity of the respective cell surface.

The mesh movement velocity for every cell surface is governed by the spatial conservation law. This rule implies that the total volumetric change is obtained by the summation of mesh moving fluxes over every cell surface, which can be expressed as

$$\frac{d}{dt}\int_{\delta V} dV = \int_{\delta S} u_{Mi} n_i dS. \tag{3.5}$$

3.2.2 Diffusive Terms

The most commonly applied method regarding diffusive fluxes on the cell surface is the central differencing method, which takes the value in the neighboring cells into account. On a cell surface f, e.g., the derivation of the scalar ϕ in one direction is defined as

$$\left(\frac{\partial \phi}{\partial x}\right)_f = \frac{\phi_c - \phi_p}{x_c - x_p},$$

where c denotes the neighboring cell, which shares the surface f with the considered point p. Thus, the diffusive term for all faces in a two-dimensional cell can be written as

$$\begin{aligned}\sum_f \alpha n_f \left(\frac{\partial \phi}{\partial x_i}\right)_f \delta S = \quad & \alpha\left(\frac{\phi_E - \phi_p}{x_E - x_P}\right)\delta S_E - \alpha\left(\frac{\phi_W - \phi_p}{x_W - x_P}\right)\delta S_W \\ + \quad & \alpha\left(\frac{\phi_N - \phi_p}{x_N - x_P}\right)\delta S_N - \alpha\left(\frac{\phi_S - \phi_p}{x_S - x_P}\right)\delta S_S.\end{aligned}$$

3.3 Linear System Solver

With the time derivative method and the differencing schemes applied, the discretized transport equation of Eq 3.1 can be summarized to

$$a_p \phi_p - \sum_f a_f \phi_f = q_p, \tag{3.6}$$

where a_p and a_f are the coefficients of the considered point (p) and face (f). q is a representative for known values as e.g. source terms and properties from the previous time step. Assuming the whole computational domain consists of N cells, Eq 3.6 can be symbolized in the matrix form of

$$A\mathbf{\Phi} = Q, \tag{3.7}$$

where A and Q are the parameter matrices of N elements. The unknown property $\mathbf{\Phi}$ can be obtained by solving the matrix system directly or iteratively.

In the iteration algorithm, Eq 3.7 can be extended by adding $B\phi^k - B\phi^k$, yielding

$$B\mathbf{\Phi}^k - B\mathbf{\Phi}^k + A\mathbf{\Phi}^k = Q,$$

which has the form in the iterative procedure of

$$B\mathbf{\Phi}^{k+1} - B\mathbf{\Phi}^k + A\mathbf{\Phi}^k = Q,$$

i.e. the properties in the next iteration $k+1$ are obtained by solving the matrix system of

$$\mathbf{\Phi}^{k+1} = \underbrace{(I - B^{-1}A)}_{C}\mathbf{\Phi}^k + B^{-1}Q,$$

where C is the iteration matrix and determines the efficiency of the solution process.

Standard methods to determine B are the Jocobi, Gauss-Seidel and SOR methods, that use different parts of the A matrix. Detailed formulations regarding these methods are described in [76].

3.4 Pressure Velocity Coupling

Numerical handling of the pressure gradient of every control volume is approached iteratively by the methods of velocity-pressure coupling. For simulations where steady state results are expected, the Semi-Implicit Method

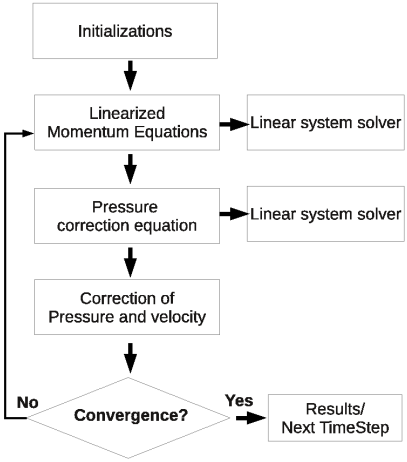

Figure 3.4: Flowchart of SIMPLE method

for Pressure Linked Equations (SIMPLE) is widely employed. This method can also be applied to transient calculations within one single time step.

SIMPLE method

In the SIMPLE method, a pressure correction function is introduced to calculate the pressure deviation depending on the uncorrelated mass flux along the cell surface. This pressure deviation has the relevant velocity component which corrects the existing velocity fields. A brief description of SIMPLE method is provided in the following:

Step 1. Guess a pressure field p^k for the k^{th} iteration. This value is normally taken from the previous iteration, time step or initial condition. The pressure gradient $\partial p^k/\partial x_i$ can thus be estimated.

Step 2. Solve the momentum equation using the given pressure gradient $\partial p^k/\partial x_i$, which results in an uncorrelated velocity field u_i^k.

Step 3. Employ the velocity field u_i^k into the continuity equation. A mass flux m_j is generated instead of the the continuity equation being fulfilled.

Step 4. Solve the pressure correction equation according to the mass flux m_j. This leads to a deviation pressure field p''.

Step 5. Calculate the relation of deviation pressure p'' and velocity u_i''. Update the pressure and velocity fields by employing under-relaxation fac-

tors.

$$p^{k+1} = p^k + p''$$
$$u_i^{k+1} = u_i^k + u_i''$$

Step 6. Repeat the procedure starting from Step 2 until the residual reaches convergence, which implies that the calculated velocity fulfills both the continuity and momentum equations.

Step 7. Proceed to the next time step.

An overview of the complete flowchart in shown in Fig 3.4.

4 Preliminary Validation of Eddy Resolving Models

In this chapter, the hybrid eddy resolving models PANS and VLES are validated by computing some generic test cases to check preliminary the model behavior for general aerodynamic applications. The flow configurations computed are: natural decay of homogeneous isotropic turbulence for capturing correctly the fluctuating flow field, the plane channel flow for the validation of the near-wall model features and the flow over a curved continuous surface for the checking the model performances in capturing the flow separation by analyzing the size of recirculation zone, drag and pressure coefficients, etc.

4.1 Decay of Homogeneous Isotropic Turbulence (DHIT)

The purpose of simulating DHIT is to validate the model behavior in a fluctuated, time dependent velocity field without presence of the solid wall. From the statistical point of view, the flow over the whole domain presents in a homogeneous isotropic state, while the fluid particles in every single point have their own directions and velocity intensities.

For a proper LES simulation using Smagorinsky model, the grid cut-off wavenumber should be around the end of inertial sub-range to estimate the residual stress and capture flow velocity in a correct manner. For coarser grid resolutions, this LES model underestimates the residual stress and velocity field becomes less diffusive. To fulfill the required physics, hybrid unsteady models are conceptualized to obtain the turbulence features. On the one hand, the turbulent models should be able to capture the velocity field according to different grid resolution. On the other hand, the modeled turbulent characteristics should be estimated correctly.

Boundary and Initial conditions

The initial conditions of DHIT play the most important role executing the simulations. Since the flow is time dependent, turbulent features would not forget the initial state in the first certain time steps of decaying. In this work, the data-sets of homogeneous isotropic turbulence is taken from the contribution of Tavoularis et al. (1997, [85]). They carried out the DNS simulation of DHIT in the cube formed computational domain of $(2\pi)^3$ in the mesh resolution of 512^3. Initial condition is set for $Re_\lambda \sim 104$, which is calculated from the decay of synthetic velocity fluctuation of $Re_\lambda \sim 945$. Periodic boundary condition is set for all three Cartesian directions. The decay procedure was then carried out until $Re_\lambda \sim 54$.

For the validation of filter cutoff LES models, the truncation interpolated initial velocity field of mesh resolution 128^3 is offered. In this section, further interpolations to coarser resolutions (64^3, 32^3) were made as initial conditions of velocity field for the validation of PANS and VLES.

The determination of unresolved turbulent characteristics for the initial condition is critical. Since the fluctuated velocity field is not in equilibrium state, the method of frozen velocity[64] is not possible. Turbulent properties accumulate when the velocity field is fixed, convergence of calculation is very difficult to reach; this is also recognized in the report of Ma et al. (2011, [58]). However, their suggestion by using the formulation of Smagorinsky LES model to estimate k_u and ϵ_u is also not suitable for coarse grid resolution of respective Re_λ, to which the grid resolution does not fit. i.e. Regarding the given case, this method would lead to underestimation of modeled turbulent kinetic energy and the overestimation of dissipation rate in coarse mesh $(32^3, 64^3)$. These initial conditions force momentum equations to resolve more in the velocity field, and model less in the subgrid scale. The simulation results will become nonobjective. As a compromise, the initial condition of k_u and ϵ_u in this work are taken from the cut-off of DNS spectrum as constant value in the whole domain, which are defined as:

$$k_u = \int_{\kappa_c}^{\infty} Ek(\kappa) d\kappa$$
$$\epsilon_u = 2\nu \int_{\kappa_c}^{\infty} \kappa^2 Ek(\kappa) d\kappa,$$

where κ_c is the critical wave-number related to the numerical grid spacing defined as π/Δ.

A crucial question validating DHIT is the essence of fluctuated turbulent properties for initial condition. Since the initial condition dominates

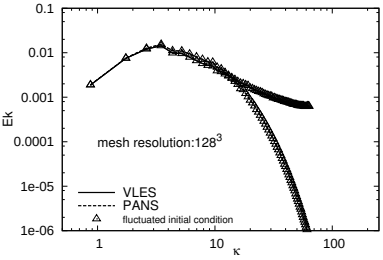

(a) Energy cascade at $t = 1.45sec$

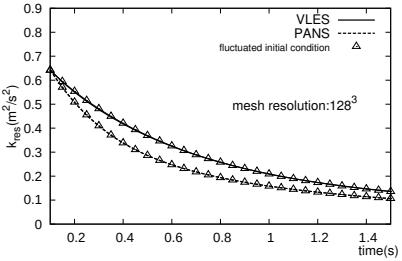

(b) Time evolution of resolved turbulent kinetic energy(k_{res})

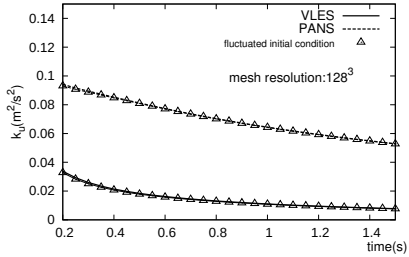

(c) time evolution of modeled turbulent kinetic energy(k_u)

Figure 4.1: Influence of turbulent initial condition

the calculation results, the determination of modeled turbulent properties must be handled carefully. Besides, based on the formulation of transport equations, every turbulent model can have different behavior. To approve this issue, correct datasets of fluctuated turbulent properties are needed. One can apply LES in the sufficient mesh resolution and estimated the turbulent properties to gain the required data.

As it is announced, Smagorinsky LES model is able to deliver the correct realization for a proper mesh resolution (128^3), see Fig 4.2, 4.3 and 4.5. After 0.1 seconds physical time (20 time steps) of LES simulation, the fluctuated turbulent properties are taken as initial field for PANS and VLES calculations. Also, the averaged values of turbulent properties over the whole domain are set to check to dependency of essence of fluctuated turbulent initial condition. The comparison are shown in Fig 4.1 in the representations of energy spectrum (Fig 4.1(a)), the time evolution of re-

solved (Fig 4.1(b)) and modeled turbulent kinetic energy (Fig 4.1(c)). It can be recognized that the fluctuated initial turbulent properties have no influence on the simulation employing PANS and VLES k-ζ-f models.

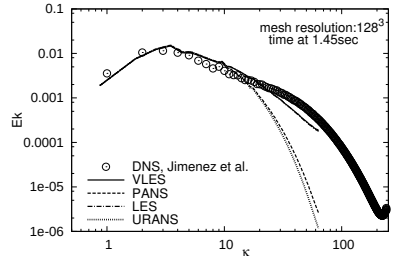

(a) Energy cascade at $t = 1.45sec$

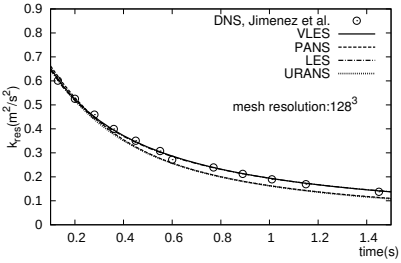

(b) Time evolution of resolved turbulent kinetic energy (k_{res})

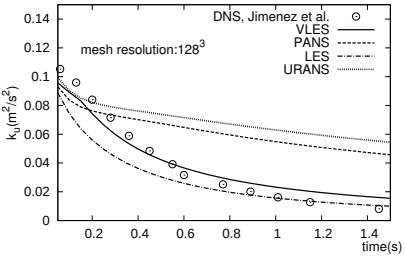

(c) Time evolution of modeled turbulent kinetic energy (k_u)

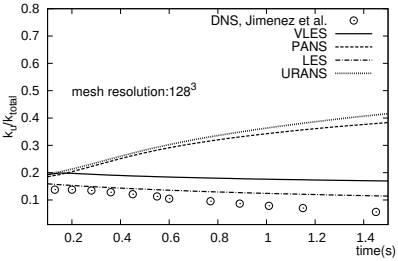

(d) Time evolution of ratio of unresolved to total turbulent kinetic energy (k_u/k_{total})

Figure 4.2: Result of DHIT, mesh resolution: 128^3

Computational Procedures

Regarding to PANS method, the modeled-to-total turbulent kinetic energy ratio (f_k) is determined by Eq 2.36. It is supposed that the flow is in homogeneous isotropic state, so the resolved turbulent kinetic energy can be estimated as

$$k_{res} = \frac{1}{2}(\widetilde{U}_i\widetilde{U}_i), \tag{4.1}$$

which builds the lengthscale which Eq 2.43 requires.

The calculation results are presented in energy cascade, which represents the capability of capturing the eddy sizes and distribution according to the velocity field. Also, the time evolution of resolved, modeled and the ratio of modeled-to-total turbulent kinetic energy of different grid resolutions are compared to the standard unsteady k-ϵ model and Smagorinsky LES model.

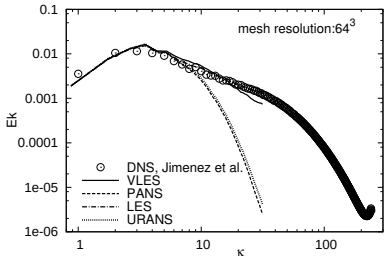

(a) Energy cascade at $t = 1.45sec$

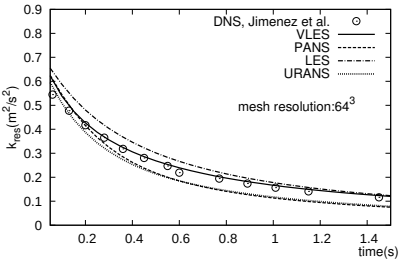

(b) Time evolution of resolved turbulent kinetic energy (k_{res})

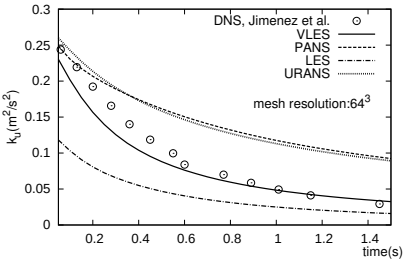

(c) Time evolution of modeled turbulent kinetic energy (k_u)

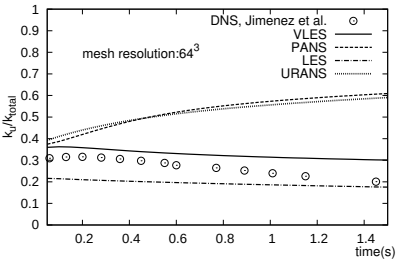

(d) Time evolution of ratio of unresolved to total turbulent kinetic energy (k_u/k_{total})

Figure 4.3: Result of DHIT, mesh resolution: 64^3

Results and Discussion

The first impression of this flow field is the velocity fluctuation over the calculation domain shown in Fig 4.4 for the iso-contour of $Q = 2.5$ at the end time step (t = 1.5sec), where Q is the second invariant of velocity

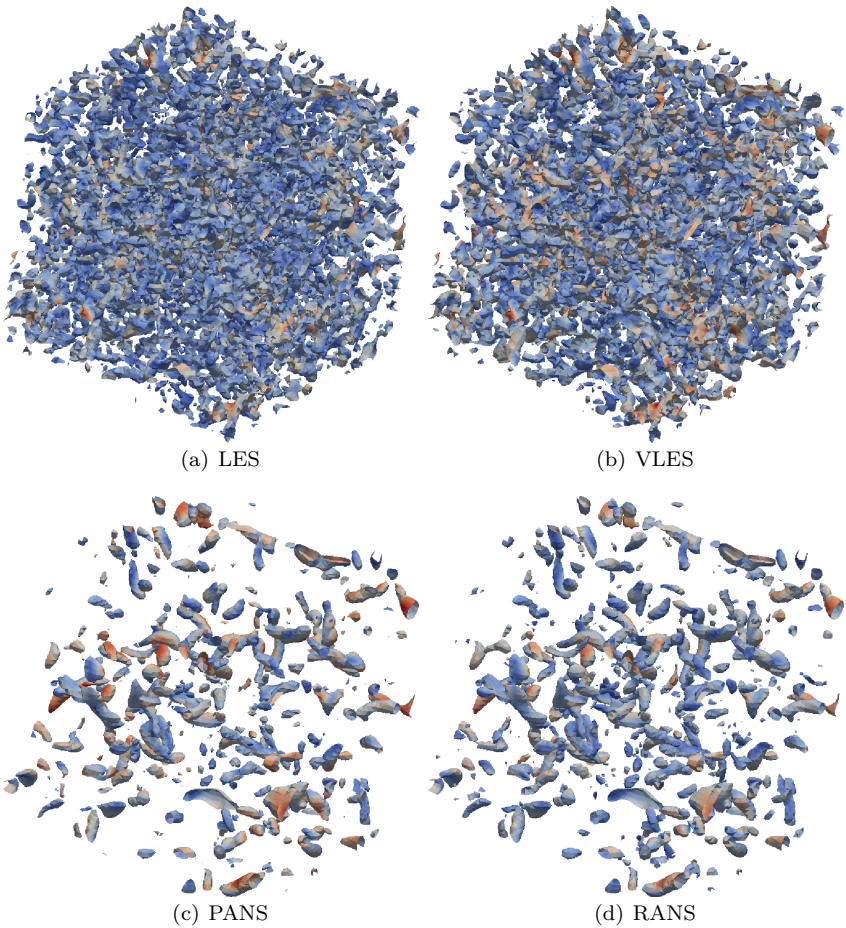

(a) LES (b) VLES

(c) PANS (d) RANS

Figure 4.4: Q invariant of instantaneous velocity field, $Q = 2.5$, mesh resolution: 64^3

gradient tensor and is defined as

$$Q = \frac{1}{2}(\widetilde{\Omega}_{ij}\widetilde{\Omega}_{ij})(\widetilde{S}_{ij}\widetilde{S}_{ij}). \tag{4.2}$$

In which, $\widetilde{\Omega}_{ij}$ and $\widetilde{S}_{ij}$ are the rotational and deformation velocity tensor defined in Eq 2.5.

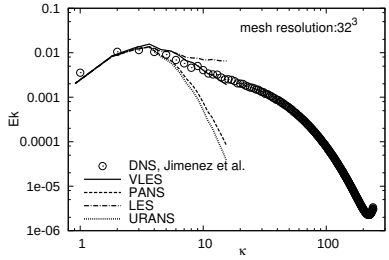

(a) Energy cascade at $t = 1.45sec$

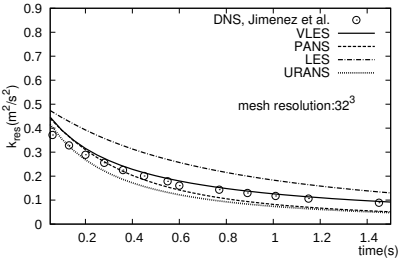

(b) Time evolution of resolved turbulent kinetic energy (k_{res})

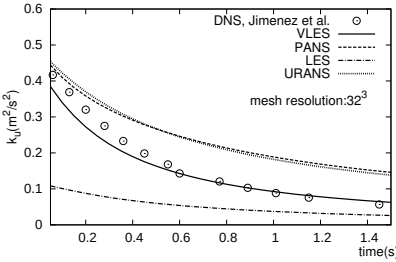

(c) Time evolution of modeled turbulent kinetic energy (k_u)

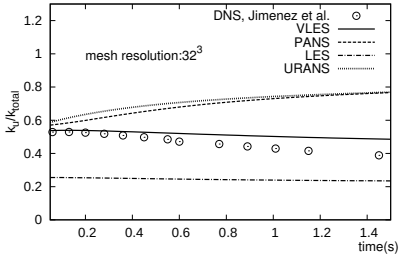

(d) Time evolution of ratio of unresolved to total turbulent kinetic energy (k_u/k_{total})

Figure 4.5: Result of DHIT, mesh resolution: 32^3

Physically speaking, Q values show the representation of eddy structures. It is recognized that LES and VLES have similar order and their resolutions are finer than the realizations of PANS and RANS.

For a more detailed analysis, the computational results comparing to DNS data according to different mesh resolution ($128^3, 64^3, 32^3$) are shown in Fig 4.2, 4.3 and 4.5. As is can be recognized in the DNS database with respect to energy spectrum, three physical ranges (energy containing range, inertial sub-range and dissipation range) are clearly represented. The critical cut-off wave number of mesh 128^3 corresponding around the end of inertial sub-range, which is sufficient for the LES Smagorinsky model, see Fig 4.2. For coarser mesh, Smagorinsky model underestimates k_u, see Fig 4.2(c) and Fig 4.5(c). This is mainly due to the insufficiency of LES assumption, that the turbulent production is not in the equilibrium state as

the dissipation rate for too coarse mesh. The ratio of model-to-total is then underestimated, see Fig4.3(d) and Fig 4.5(d). Especially for the mesh of 32^3, critical cut off wave number lays in the beginning of inertial subrange, by which the improper velocity scale forces the momentum equation to resolve more. The velocity field becomes less diffusive, which denotes the small eddies appear abnormally, and the slope of inertial sub-range tends larger than $-5/3$.

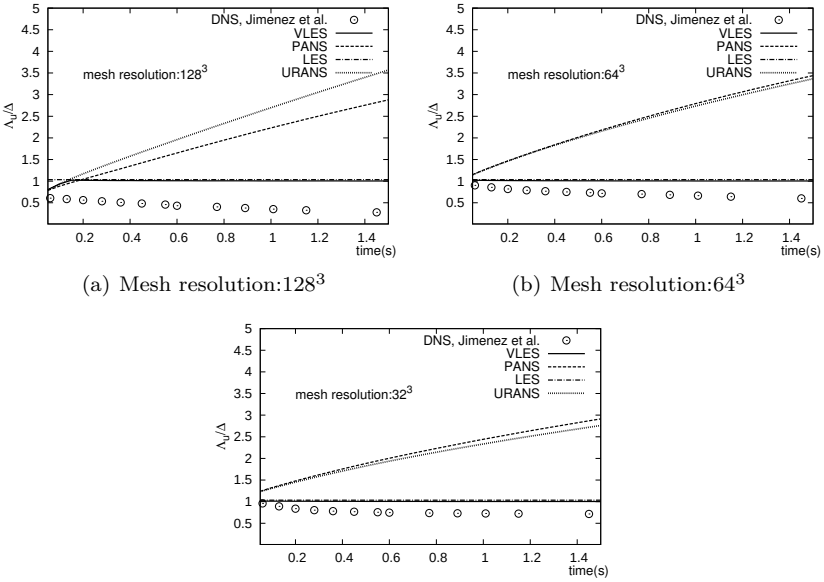

(a) Mesh resolution:128^3

(b) Mesh resolution:64^3

(c) Mesh resolution:32^3

Figure 4.6: Ratio of subgrid length scale to grid spacing

RANS in unsteady mode has also deficits simulating DHIT. As it is shown in all three mesh resolutions, this modeling strategy presents too diffusive realizations and the slope of inertial sub-range is smaller than the reference data. i.e. The fluctuations disappear and the subgrid turbulent scales are overestimated, see Fig 4.2(c), 4.3(c) and 4.5(c).

In principle, eddy resolving models are conceptualized to fulfill the lacking information of LES in coarse mesh resolution. While VLES is able to reproduce the physical properties in a correct manner, the realizations of PANS show similar representation as RANS, which overestimates the

model part and resolves less than the mesh requests. This phenomenon could be lead by the formulation of f_k (Eq 2.36), the assumption of smallest resolved lengthscale should be considered and calibrated in the careful way.

Comparing the ratio of modeled lengthscale to grid size, see Fig 4.6, LES and VLES obeys the rule of Eq 2.27 to unity, whereas the ratios raise during the calculation applying PANS and RANS models.

Generally speaking, DHIT shows a plausible representation for flows in statistical homogeneous and isotropic states, where the filter width has the same order as the subgrid lengthscale if the grid cutoff lays in the inertial sub-range. However, the system becomes more complicated in the complex system, the criterion should validated for the anisotropic features.

4.2 Plane Channel Flow of $Re_\tau \sim 395$

Plane channel flow is the most validated test case of turbulent modeling. Geometrically speaking, the flow is only bounded in normal direction, streamwise and spanwise dimensions are defined as infinite long and wide, which means the effects of wall dominate the flow characteristics. For the validation, turbulent models should be able to produce the proper near wall physics, i.e. log-law of averaged velocity field, auto-correlation, etc. In the unsteady mode, two points correlation of instantaneous fluctuations are also required to demonstrate the capability of turbulence model.

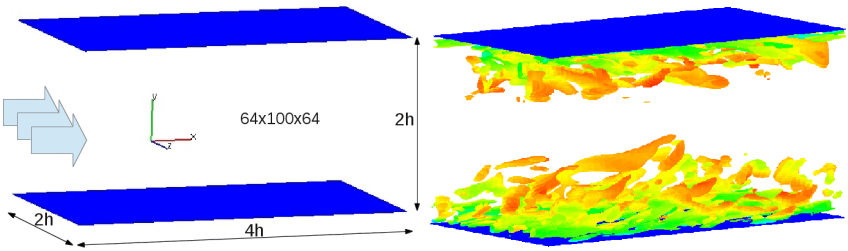

(a) Computational domain (b) Flow structure, $Q = 0.005$

Figure 4.7: Illustrations of plane channel flow

Most steady RANS models have been validated successfully. Since the flow characteristics is statistically steady and homogeneous in streamwise and spanwise directions, calculation can be realized in normal direction for

one dimensional mesh domain. For the unsteady state, this simplification is not valid at all. Calculations should be applied in three dimensional mesh with periodic boundary condition in streamwise and spanwise direction to capture the instantaneous features.

However, since plane channel does not obtain geometrical changing in all three Cartesian dimensions, fluctuated state is difficult to achieve. Even for DNS, perturbations are needed as initial field to generate the velocity fluctuation. Once the fluctuations occur after certain flow-through-times, turbulent flow will forget the initial state, the initial condition becomes no more important.

The feature of classical RAN models in the unsteady mode for this configuration is the absence of unsteadiness representing the velocity components. Mostly, the fluctuations die out during the calculation. The simulation results in steady state due to the Reynolds averaging principles. Also, the steady realizations have identical quantity as the the results in the steady mode; i.e. the realistic instantaneous representation can not be captured by classical RANS models in the unsteady mode regarding the plane channel geometry.

Large Eddy Simulations are conceptualized to resolve the eddy structure, which show velocity fluctuations in the calculation domain. i.e. LES represents the unsteadiness and inhomogeneity of flow structures. However, capturing the near wall properties in a correct manner is very challenging due to the requirement of very fine mesh resolution. This issue becomes extreme in the high Re condition. Recently, WALE[66], CSM[44] and some dynamic LES models[20][21] are proposed to deal with such problems. Nevertheless, grid requirement of LES simulation remains a tough issue dealing with turbulent physics in the near wall region.

Comparing to the classical RANS and LES, hybrid ER methods show the advantages dealing with unsteadiness and near wall properties. On the one hand, hybrid models can resolve the eddy structure according to the given grid size; on the other hand, RANS models are applied to estimate the near-wall turbulent features in a proper manner.

Computational Details

The validations of plane channel flow in this section is carried out by applying the hybrid model PANS and VLES for $Re_\tau \sim 395$. Numerical domain is applied of maximal y^+ for 0.9 in $64 \times 100 \times 64$ of streamwise, normal and spanwise directions for maximal Δ/η of 16 in the near wall region, where η denotes the Kolmogorov lengthscale. Calculation results are shown in ve-

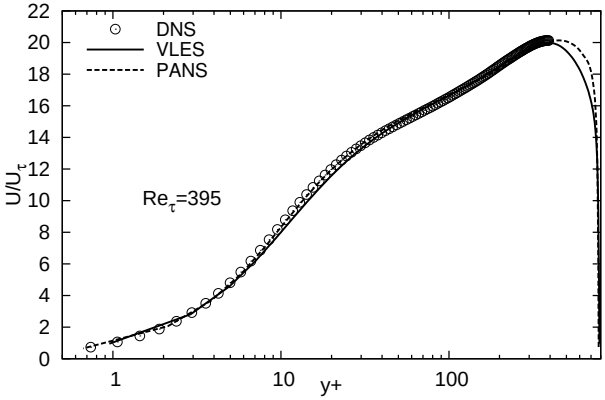

(a) Mean velocity profile

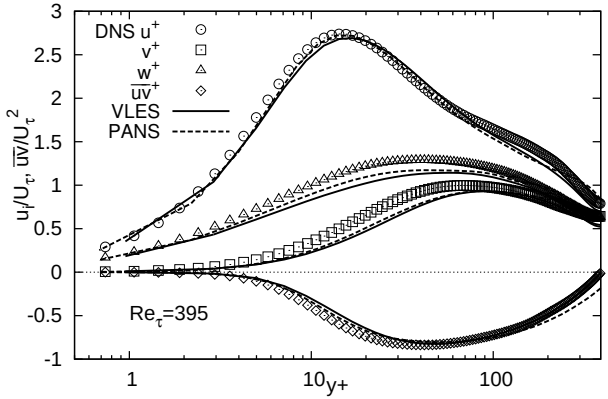

(b) Reynolds stress components

Figure 4.8: Averaged velocity and auto-correlation components, VLES and PANS

locity profile corresponding to log-law, auto-correlation and the fluctuated two-points correlation in streamwise and spanwise direction in the middle of the plane channel comparing to the DNS data contributed by Moser et al. (1999, [65]).

Results and Discussion

Statistical characteristics of turbulent feature are the most concerned representations of plane channel flow. For this issue, the averaged velocity profile and Reynolds stress components of both models show quantitative good agreements comparing to DNS data, see Fig 4.8(a) and 4.8(b). While the representations of RANS k-ζ-f model show the identical sequence of auto-correlation $\overline{uu}$, $\overline{vv}$, and $\overline{ww}$ along the normal direction due to the assumption of isotropic turbulent properties applied in EVM, this characteristics is then shrunk by the unsteady feature in the simulation employing ER models. The resolved velocity fluctuation in ER method become the dominant part building the auto-correlation.

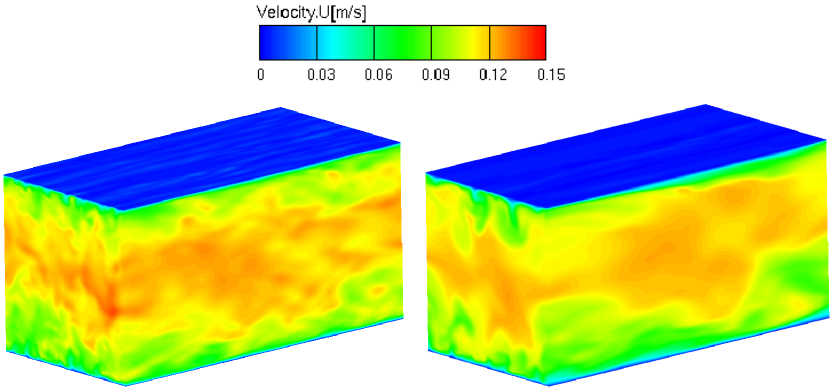

(a) PANS (b) VLES

Figure 4.9: Instantaneous velocity contour

Regarding the fluctuation intensity, Fig 4.9(a) and 4.9(b) show the instantaneous velocity field in the computational domain, which the representation of both models show the unsteady and inhomogeneous flow features. This denotes the eddy structures are captured during the calculation. Comparing to VLES, PANS shows a very fine resolution in the near wall area.

The two-points correlation of velocity fluctuations represents the distribution of eddy structures captured by the momentum equation. Fig 4.10(a) and Fig 4.10(b) show the correlation of both models in streamwise and spanwise directions in the middle of plane channel. As it is illustrated, the representation of both models match the reference data in a realistic

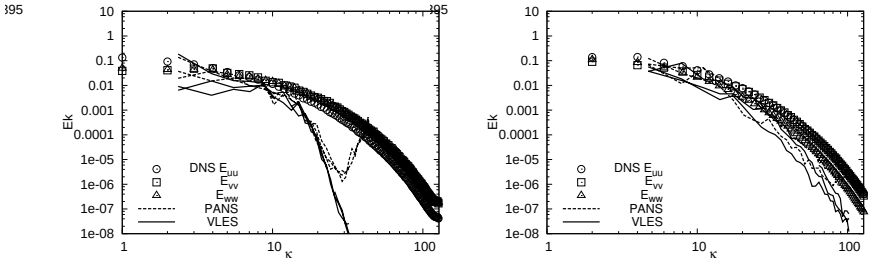

(a) Streamwise direction (b) Spanwise direction

Figure 4.10: Energy Spectrum in the middle plane of channel

manner, which indicates that the velocity fluctuations are well captured by the momentum equation in the filtered based mode. The peak in the high wave number region of PANS in the streamwise spectrum might be interpreted as the excessive resolving of momentum equation, or simply the numerical instability. An arbitrary conclusion can not be made.

Concerning the behavior of turbulence model, Fig 4.11 shows the proportion of modeling, which is defined by the ratio of modeled-to-total turbulent kinetic energy in the computational domain. As it is shown, the ratio of both models raise in the near wall area towards unity, which means more modeling part is applied in this region. By employing distinguishing feature of based RANS model, the hybrid ER method is then capable to approach the near wall properties in a correct manner. This representation varies with different RANS models, e.g. Han and Krajnović (2012, [28]) validated the k-ϵ and k-ω based VLES method. A hybrid ER model can be properly applied, if both the hybrid coupling method and the feature of based RANS model are suitable for the aimed flow configuration.

The deeper discussion of the modeling technique can be focused on the comparison of modeling factor f_k (PANS) and F_k (VLES) to their total modeling ratio (k_u/k_{total}). It can be recognized in Fig 4.11 that both modeling factors have the same tendency following their total modeling ratio. However, due to the assumption in the modeling procedure, they are not really identical to each other. In both realization of PANS and VLES, the modeling factors (f_k, F_k) are both larger than the modeling ratio in the near wall region. This is also one of the general criteria for hybrid turbulence models, which apply the ratio of the turbulent properties.

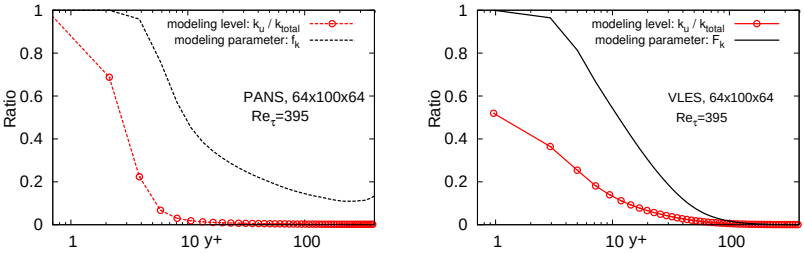

(a) PANS (b) VLES

Figure 4.11: Comparison of modeling level (k_u/k_{total}) and modeling parameter (PANS:f_k, VLES:F_k)

4.3 Turbulent Flow of Two-dimensional Hills

Turbulent flow in the geometry of two dimensional hill is one of the standard generic cases validating the turbulence model with respect to the separation shear layer. Geometrically speaking, the fluid is supposed to flow over several identical hills. The spanwise direction is assumed to have no influence on the flow, so the geometrical changing in the normal direction becomes the only effect on the flow characteristics. Phenomenologically speaking, fluid particles pass through a narrowing and expanding wall, which induce the flow acceleration and deceleration. After that, the characteristics recover, and the flow repeats the same procedure for the another hill. These conditions can be applied in the numerical domain as periodic boundary condition in the streamwise and spanwise direction, see Fig 4.12.

Due to the sudden expansion, the flow separates on the hill top and generates a recirculation zone in the downstream of hill side. Depending on the flow velocity and the geometrical changing, the length of the recirculation zone varies accordingly. For the issue of separated shear layer and flow recirculation, experimental measurements was investigated by Almeida et al. (1993, [2]) under several Re_H, which it is defined by bulk velocity, hill height and the kinematic viscosity of the fluid.

In the statistical representations, the flow presents in a steady state; so the most RANS models are applied in the two dimensional mesh; i.e. one cell in the spanwise direction. Temmerman et al. (2003, [86]) carried out the LES simulation for $Re \sim 10,595$, which is widely taken as the reference data for the model validation. However, most RANS models fail by cap-

turing the length of recirculation zone and the turbulent properties. Jang et al. (2002, [38]) discovered the strong variation of separation and reattachment point in the configuration, which causes the most RANS models being not able to estimate the shear stress in the correct manner around the separation region. Once the shear stress is underestimated, the length of recirculation zone is overestimated.

Another factor of improper turbulence approach is the applied assumption. As it is mentioned in the previous chapter, Boussinesq's assumption takes the linear dependency of strain rate, which denotes the isotropic feature of turbulent properties. The neglected information contains the rate of rotational tensor and its higher order combinations, which obtain the turbulent anisotropy and the description of main rotational features. This lacking information not only lead to the improper estimation of the Reynolds stress tensor, but also the improper realizations of velocity components, e.g. the absence of recirculation in the rotational channel system, and the overestimation of the central recirculation zone in the swirling configuration, etc.

For the proper realization, the ER models should be capable to capture the instantaneity and turbulent anisotropy by shrinking the modeling ratio. Correspondingly, the domain have to be employed in three dimensional, and the calculation is carried out in the unsteady mode.

Calculation Details

The numerical domain, illustrated in Fig 4.12, is 9 times hill height(h) in streamwise and $4.5h$ in spanwise direction. Upper and lower side are bounded with respect to the plane wall. The height on the hill to upper wall is $2h$, see Fig 4.12. Details of the geometrical configuration are described in [http://www.ercoftac.org/].

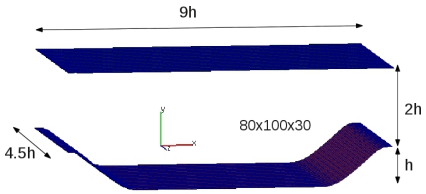

Figure 4.12: Computational domain of two-dimensional hills

For the validation of hybrid ER models, simulations of two Re_H (10600,

37000) applying PAN, VLES and RANS are carried out. The calculation results are compared with reference experimental and LES data. For the applied numerical mesh, the standard mesh of $80 \times 100 \times 30$ in streamwise, normal and spanwise direction is employed. The realizations are averaged over 30 flow-through-times and spanwise direction presented in mean velocity, drag coefficient and Reynolds stress components for 10 cross sections over the streamwise direction.

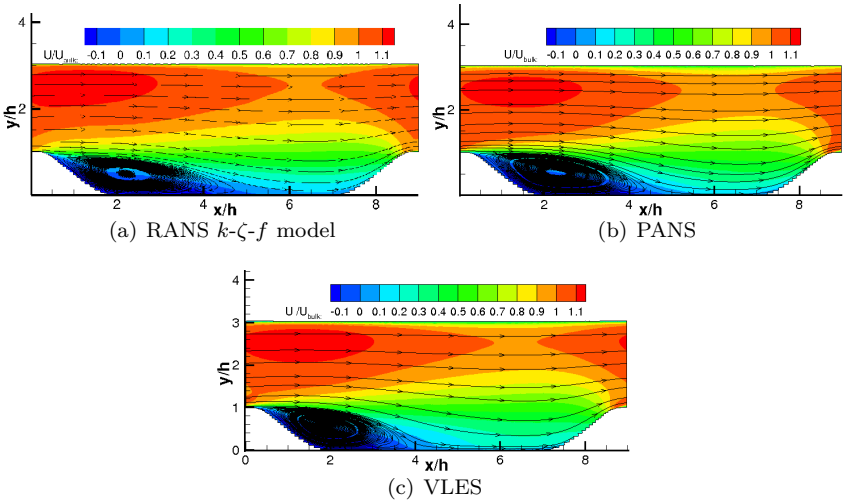

(a) RANS k-ζ-f model

(b) PANS

(c) VLES

Figure 4.13: Streamlines and velocity contour

Results and Discussion

The time averaged stream lines of RANS, PANS and VLES based on the k-ζ-f model are shown in Fig 4.13. In streamwise direction, flow separates at $0.2h$ and reattaches at $4.7h - 5h$ according to different models. In this region, mean flow decelerates outside of recirculation zone. The flow then recovers for more than $2h$ long and accelerates towards the hill upstream. The detail reattachment position can be recognized in Fig 4.14 of the curve of drag coefficient cross over the zero line.

The approximation of recirculation zone is various by applying different modeling techniques. While the length is overestimated as several literature

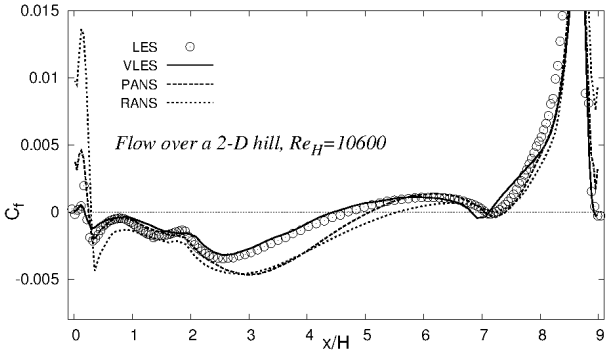

Figure 4.14: Drag coefficient

.

reported e.g. [38] for RANS realization, PANS has already better approximated length than RANS. By comparison, VLES shows the $4.7h$ for the reattachment position which matches very well to the reference data. This might lead to an assumption by observing the modeling ratio shown in Fig 4.17(a) and Fig 4.18(a), where there are smaller values in VLES realization than in PANS in the downstream region of hill, so the length of recirculation zone is better estimated for the low modeling ratio for the critical region where the EVM assumption is not fit to. For a concrete understanding, this arbitrary assumption should still be investigated in a deeper manner.

For the comparison of Reynolds stress components in cross plots, see Fig 4.16, the hybrid ER models deliver a more precise representations in velocity profile and Reynolds stress components than the RANS representations. For the turbulent shear stress on the separation point is mentioned in [38], the PANS realization is also underestimated, which causes the overestimation of recirculation zone as it is previously described.

Generally, the deficit of RANS modeling are minimized by reducing model portion in the simulations employing hybrid ER models. This forces the momentum equation to resolve more velocity fluctuations which dominate the approximation of auto-correlation. However, the model portion of PANS seems to be too large for building the proper shear stress, see Fig 4.17(a), which is not enough to be able to trigger the fluctuation dominating in the critical region.

For the simulation of high $Re_H \sim 37000$, it is demonstrating that the hybrid ER models also show very realistic representations on the coarse

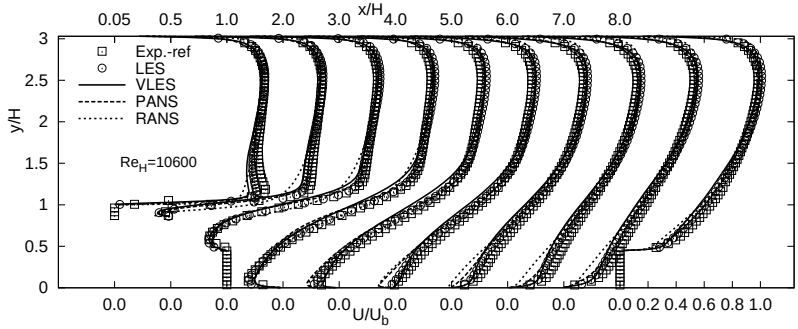

(a) Velocity profile

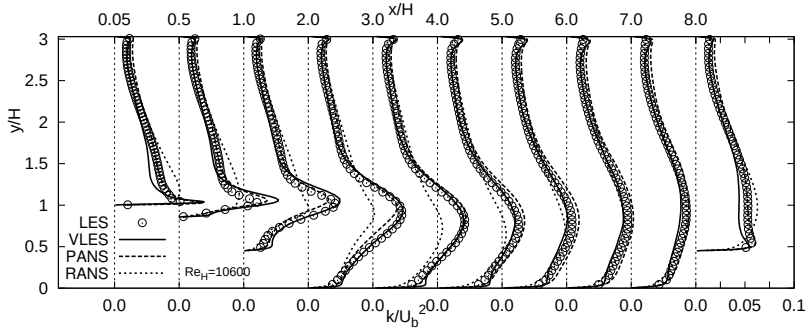

(b) Turbulent kinetic energy

Figure 4.15: Cross plots of velocity and turbulent kinetic energy, $Re_H \backsimeq 10,600$

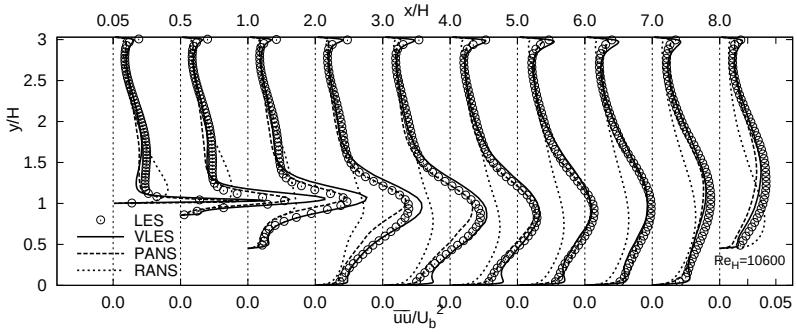

(a) Reynolds stress component, $\overline{uu}$

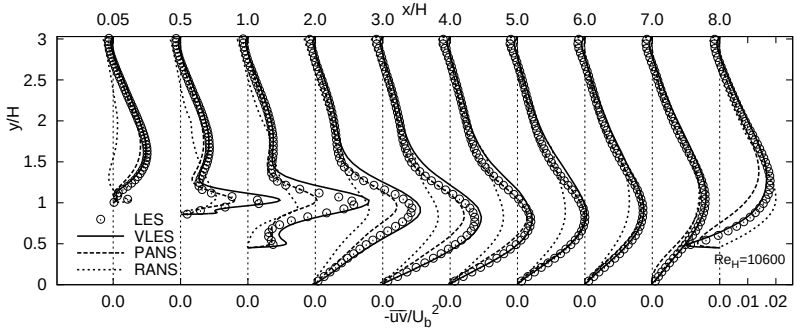

(b) Reynolds stress component, $\overline{uv}$

Figure 4.16: Cross plots of Reynolds stress components, $Re_H \backsimeq 10,600$

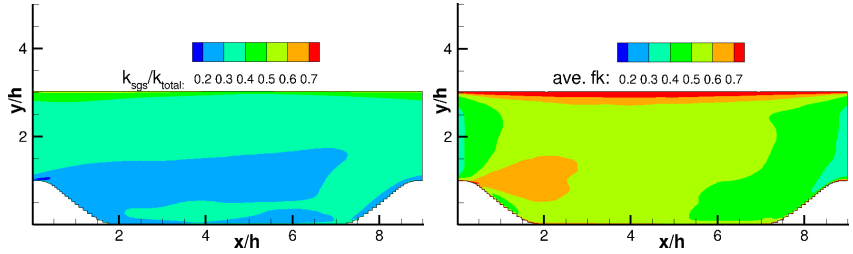

(a) Modeling ratio(k_u/k_{total}) (b) Modeling parameter(f_k)

Figure 4.17: PANS realization, $Re_H \backsimeq 10,600$

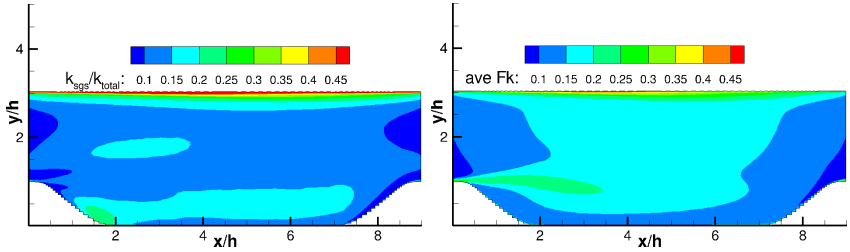

(a) Modeling ratio(k_u/k_{total}) (b) Modeling parameter(F_k)

Figure 4.18: VLES realization, $Re_H \backsimeq 10,600$

grid, see Fig 4.19. Comparing to a competent LES realization, which requires very fine mesh resolution in the whole domain, the ER models show a enormous advantage adapting the flow condition for coarser grid, which the simulations of complex system generally request.

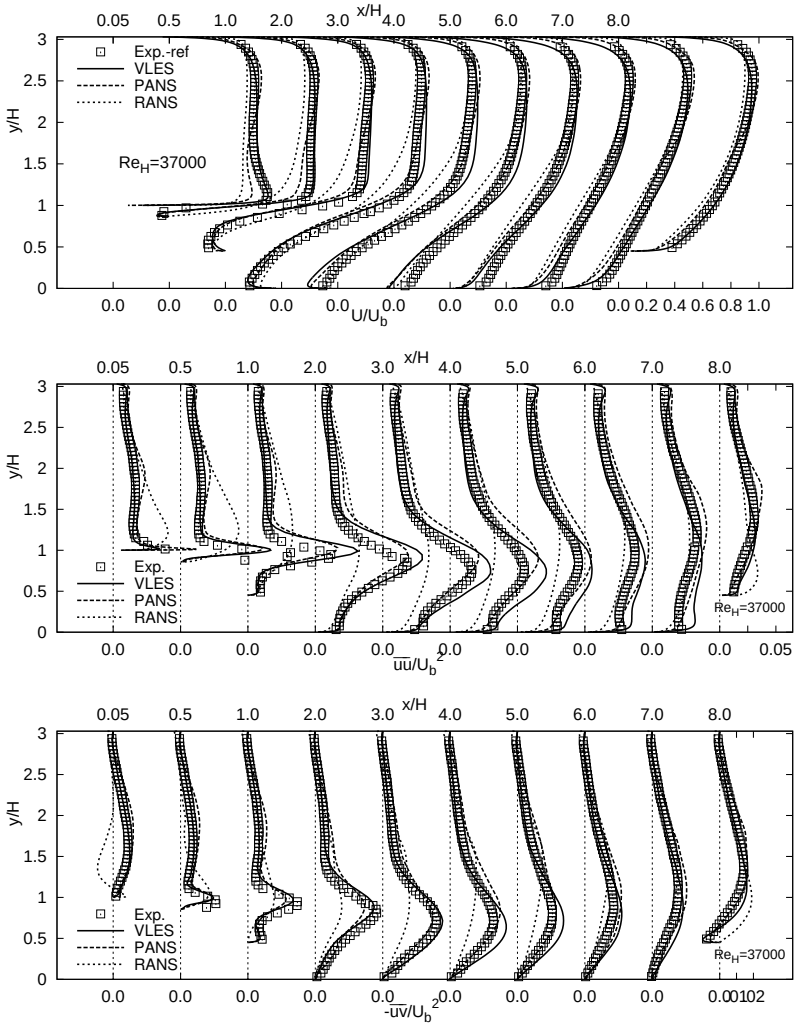

Figure 4.19: Velocity and Reynolds stress components, $Re_H \sim 37,000$

5 Application of Turbulent Models with respect to ICE relevant Generic Configurations

Swirling flows and tumbling motion are the dominant phenomena appearing in the internal combustion engine system. These aerodynamic effects have determinative influence on the fuel gas mixing behavior. At the end of the compression stroke right before the ignition begins, the fine structured, well distributed eddies contribute the combustion process in the good burning efficiency. However, the turbulence obtained in such configurations is instantaneous and highly anisotropic, which is not possible to describe by using RANS method. In contrast, eddy resolving method, which captures the velocity fluctuation, fulfills these requests and should be capable to realize the flow in the unsteady manner .

In this chapter, relevant aerodynamic features occurring in the ICE are taken into consideration, mainly the swirling flow and the generation, as well as the compression of turbulent tumbling motions. The validation of hybrid eddy resolving models is carried out to take a deeper glance in the purpose of their capability regarding the rotational configurations.

5.1 Helical Swirling Flow in Vortex Tube

Not only for the internal combustion engine system, the understanding of swirling flow phenomenon becomes economically important also due to the commonly applications in fields of furnace and jet-engine. Referring to the mixing process in the combustion chamber, Roback and Johnson (1983, [74] applied the swirling co-axial jet as inlet condition to the observation domain to examine the effects of swirling motion on the mixing characteristics. They recognized the presence of central recirculation zone. Also, the peak momentum turbulent transport rates are approximately the same as the one of non-swirling flow condition. These results indicate that the mixing process for swirling flow is accomplished in one-third of the length it requires for the non-swirling condition. The Roback and Johnson exper-

iment is taken as the standard data base for further numerical validation with respect to the turbulent swirling flow configuration.

One significant phenomenon in the swirling configuration is the large coherent structure, which is observed in the near axis vortex break down region described by Wang et al. (2004, [95]). This statical helical structure, which is analyzed by Alekssenko et al. (1999, [1]), depends in the geometrical swirl number, outlet eccentricity and its helical frequency. In the investigation of Paschereit et al. (1999, [69]), the helical structure is noticed attributing to the flow unsteadiness. Among the experimental works with respect to swirling characteristics, Shtork et al. (2005, [80]) employed cylinder vortex tube without bounded space and observed the dipole helical structure around the nozzle output. The dipole structure is formed by the precession of central mono-polar vortex accompanying with secondary vortices in the opposite directions. Similar phenomena are also noticed in the experimental work of Grundmann et al. (2012, [27]).

Several numerical investigations involving swirling flow in combustion chambers have been carried out during recent years.[68]. Concerning the Robak and Johnsen case, Lin (1998, [57]) validated the Durbin's $\overline{v^2}$-f model and got a good agreement to experiment due to the proper turbulent energy transfer modeled by the elliptic relaxation function. Leschziner and Hogg (1989, [55]) applied the modeling strategy of Reynolds stress modeling. They also compared with the results of k-ϵ model and analyzed the weakness of the common eddy viscosity modeling technique.

In general, as it is summarized by Wang et al. (2004, [95]), Escudier et al. (2006, [16]), etc., the classical two-equation RANS models fail by realizing the swirling characteristics due to the neglected rotational motion and turbulent anisotropy. Simulations applying RSM and ARSM have realistic results and show better agreement to the experimental data. However, the large structure obtains strong unsteadiness of flow state, which is still difficult to be captured in the classical RANS regime. For these reasons, filtered based ER models become the upcoming strategy realizing such flow configuration.

Flow Configuration

The current test case is experimentally investigated by Grundmann et al. (2012, [27]). They designed a generic vortex tube with tangential double inlet swirl generator conducted by the diffuser, see Fig 5.1. Deionized water was taken as medium, which enters the inlet pipe upstream of the diffuser with a constant diameter of $25.4mm$ and a length of $157mm$. This

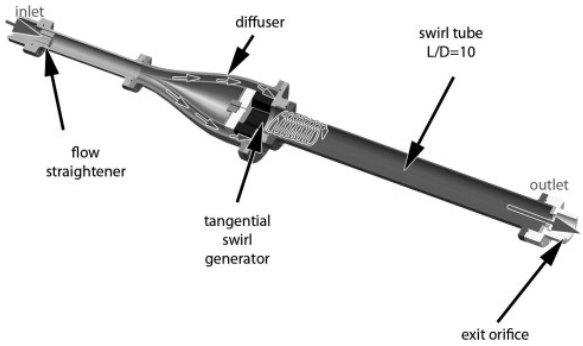

Figure 5.1: Abstraction of experimental configuration

annular diffuser supplies the swirl generator with a uniform flow. The swirl generator generates the swirl flow under the implementation of two tangential inlets. Each inlet has the cross sectional area of $29.33mm \times 8.8mm$. A detailed sketch of the swirl generator is given in Fig 5.2(a).

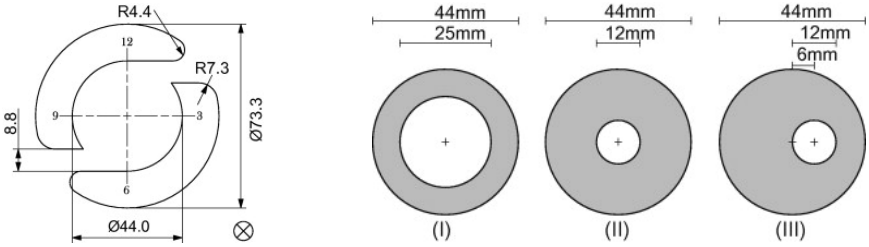

(a) Swirl generator configuration

(b) Outlet orifices geometries

Figure 5.2: Experimental setups: swirl generator and outlet configuration

The swirl tube has a length-to-diameter (L/D) ratio of 10. The tube's inner diameter(D) is $44mm$. All axial positions are given as the dimensionless parameter z/D, where $z/D = 0$ is at the end of the swirl generator and $z/D = 10$ denotes the outlet or exit orifice position.

At the end of the swirl tube, three different types of orifice are applied, illustrated in Fig 5.2(b). The experiments are carried out with $Re = 15000$, which is defined by the axial bulk velocity in the swirl tube, the tube diameter and kinematic viscosity of water at 20^oC. This corresponds to the

flow rate provided by the pump of 31.05 l/min. The regarding flow configuration, which belongs to the large length-to-diameter category of King's classification[43], presents a strong circumferential interaction between tube wall and vortex flow.

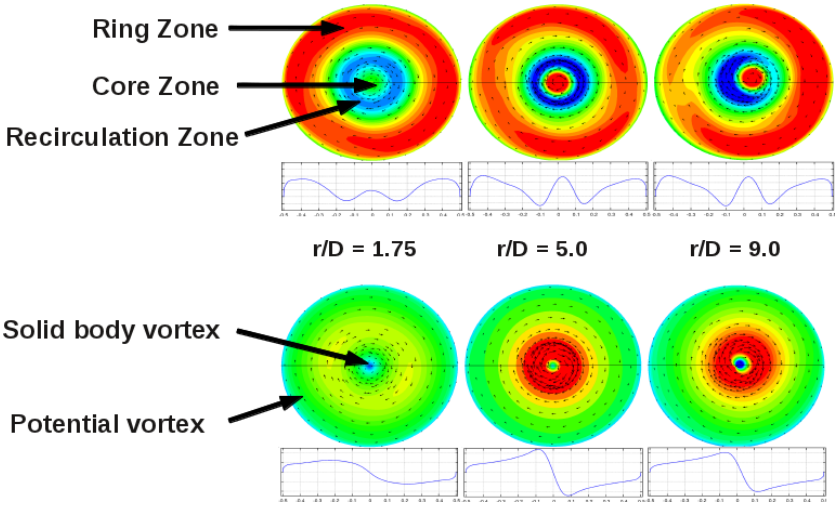

Figure 5.3: Illustration of flow structures, axial (upper) and tangential (lower) velocity, large orifice, LES realizations

The experimental investigation shows some significant phenomena in the vortex tube cross section. For the centric geometry, three different velocity zones can be classified, *ring zone*, *recirculation zone* and *core zone*, see Fig 5.3. In the *ring zone*, the axial velocity tends to maximum in the near wall region, spiraling in the left handed helical structure. The *core zone* appears in the middle of the vortex tube, where the axial velocity achieves its peak, this builds into a jet in the axial direction towards the outlet orifice. The *recirculation zone*, in which the axial velocity goes to negative due to the vortex break down for large swirl number conditions. In the representation of tangential velocity, these three velocity zones can be interpreted as the overlaps of solid body vortex and potential vortex.

For the eccentric outlet geometry, similar zones in the cross section are also observed. Significantly, the core jet performs in the helical curve due to the outlet eccentricity. The helical structure of ring zone is formed in the right-handed, which is countered to the stream line, helical direction,

see Fig 5.18.

Computational Details

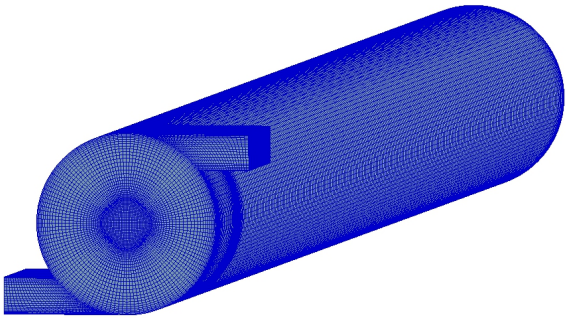

Figure 5.4: Computational domain, small orifice

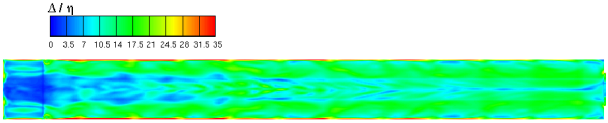

Figure 5.5: Grid resolution, Δ/η, LES, small orifice

orifice type	large	small	eccentric
total cells	$1,197,768$	$1,267,272$	$1,294,920$
max. Δ/η	49.72	44.96	41.36
max. y^+	4.71	6.32	6.27

Table 5.1: Details of numerical mesh quality.

The computational domain is constructed corresponding to the experimental settlements and simplified by applying two tangential inlet ducts connecting to the swirl tube instead of implementing the diffuser in the experimental setups. Each inlet duct is meshed by $25 \times 20 \times 40$ in streamwise, normal, and spanwise directions. The inner domain of vortex tube is

meshed by around 1.2 million hexahedron cells obtaining 160 cells in axial direction, see Fig 5.4. Between the inlet ducts and cylinder, interpolation is taken to avoid the high aspect ratio of cell geometry. The maximal y^+ on the tube wall is less than 10. The mesh resolution in the computational domain is qualified by the value Δ/η for maximal value in the near wall region less than 50. Details of three different geometries are listed in Table (5.1).

For the settlements of boundary condition, the fixed mass flow value of $0.258kg/s$ is given for each inlet surface. The physical properties are averaged for 5 seconds physical flow time, which corresponds to 6 flow-through times, after the turbulence is fully developed.

Results and Discussion

Centric Orifices

The first impression of the flow characteristics is the instantaneous velocity fields, shown in Fig 5.6 for the configuration of large outlet orifice. It can be noticed that not only the instantaneity is presented, the three-layer structure can be well observed in the unsteady representations.

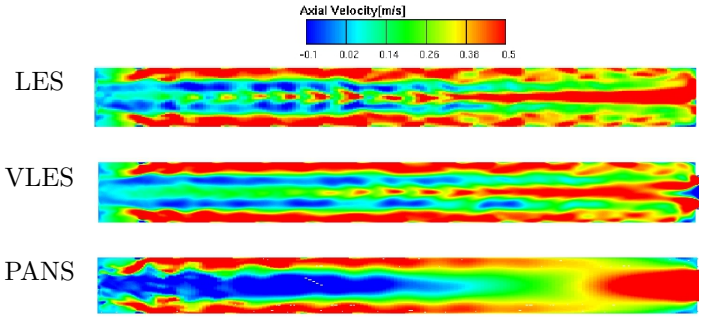

Figure 5.6: Instantaneous axial velocity fields, large orifice

For the averaged flow features, calculation results of LES, RANS, PANS and VLES are presented in Fig 5.8, 5.11, and 5.17. In the tube cross sections, three different velocity zones can be well observed in the realizations of LES and VLES, while PANS and RANS are not capable to capture the

core zone, where the recirculation zone dominates over the cross section and the outlet stream forms as pipe first at the end of the vortex tube.

In the axial direction, the intensity of core jet increases towards the outlet orifice. Regarding the helical structure, for the configuration of centric orifice, the ring zone and streamline represent both in a left-handed direction, which is produced by the swirl generator, see Fig 5.12. These realizations show good qualitative agreement comparing to experimental data.

Quantitatively, the intensity of the core jet is underestimated by LES and VLES, see Fig 5.8. The velocity profiles seem to achieve the intensity level shown in the experiment first in middle of the vortex tube. This can be also observed concerning the right-handed ring structure in the eccentric configuration, see Fig 5.18. These derivation may be caused by applying too coarse grid resolution. For this interest, a finer mesh of 3.3 millions cells with its maximal Δ/η value around 30 is applied and the comparison shows the improvement of result quality, see Fig 5.14. The competent mesh for the regarding configuration can be expected by keeping refining the mesh resolution. Nevertheless, the aim is of this work is to validate the turbulent models with the corresponding physical phenomena and take a deeper look into the characteristics of the eddy resolving turbulent approach.

With respect to the modeling technique, Fig 5.13 is the comparison of modeling level concerning LES, VLES, PANS and RANS in the illustration of ν_t/ν. These representations show that VLES and VLES results are in the same order, while PANS has very high modeling levels as the RANS realizations. Following this aspect, it is expected that VLES(F_k) tends to apply very small modeling parameters, and much higher f_k values dominate in the PANS simulation, see Fig 5.9.

It seems that the high f_k value obstructs the momentum equation to resolve more velocity fluctuation in the PANS method. However, the PANS calculation doesn't show improvement in the quality of results on the refined mesh, either, see Fig 5.19. The core jet can still not be captured at all. This phenomenon shows the weakness of PANS method, for which the f_k value tends to be overestimated in the outlet region, where the based RANS model is not capable to predict the flow in a correct manner, also the flow presents in a statistical steady state. Thus, the over-predicted f_k values lead the numerical realization to the RANS-like results.

Eccentric Orifice

The flow characteristics in the eccentric orifice configuration have similar representations as the centric one, three layer structure is also observed in

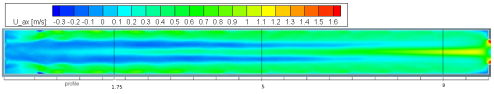

(a) axial

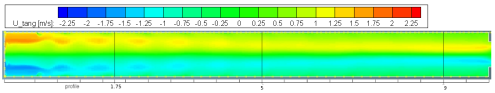

(b) tangential

Figure 5.7: Velocity contour, large orifice, LES realization

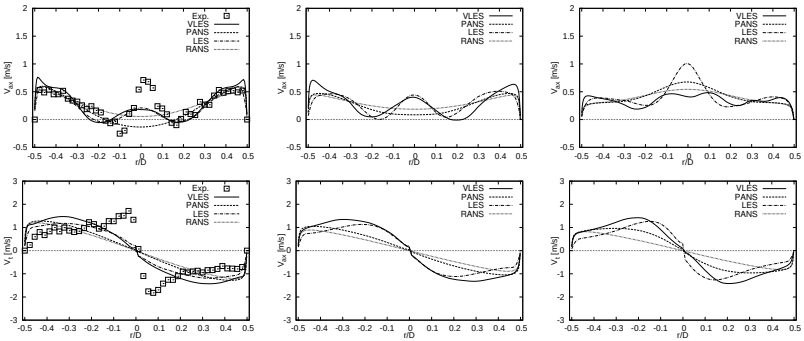

Figure 5.8: Large centered exit orifice - axial (upper) and tangential (lower) velocity profiles at $z/D = 1.75$(left), 5(middle), 9(right)

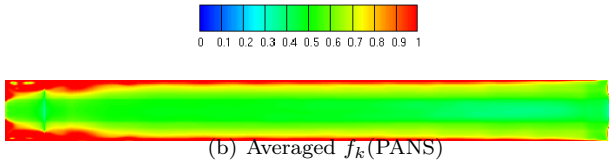

(b) Averaged f_k(PANS)

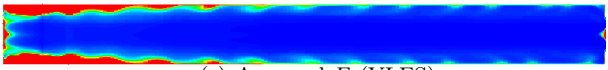

(c) Averaged F_k(VLES)

Figure 5.9: Distribution of modeling parameter f_k(PANS) and F_k(VLES), large orifice

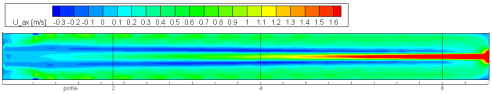

(a) Axial velocity

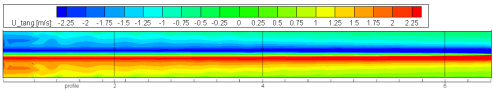

(b) Tangential velocity

Figure 5.10: Velocity contour, small orifice, LES realization

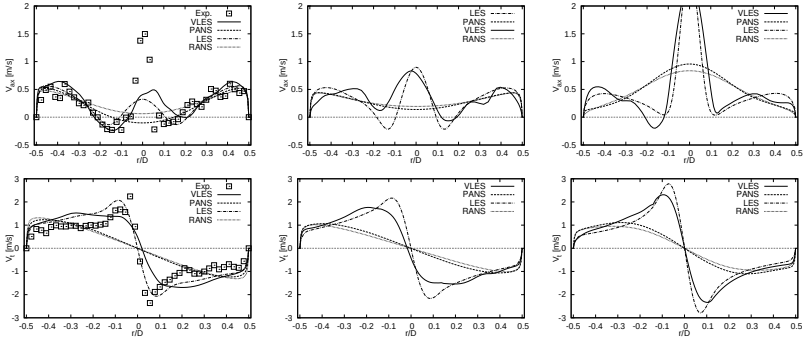

Figure 5.11: Small centered exit orifice - axial (upper) and tangential (lower) velocity profiles at $z/D = 1.75$(left), 5(middle), 9(right)

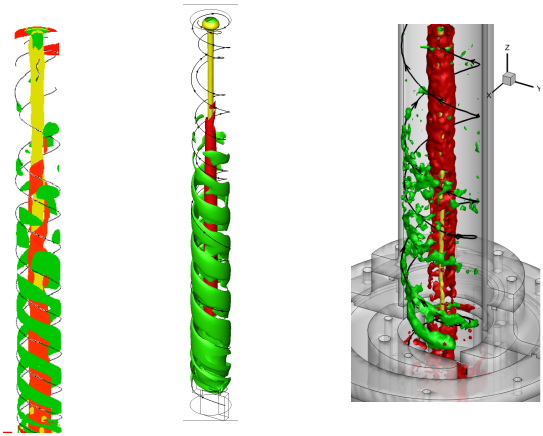

Figure 5.12: Iso-velocity contour of axial velocity, small orifice, VLES(left), LES(middle), Exp.(right)

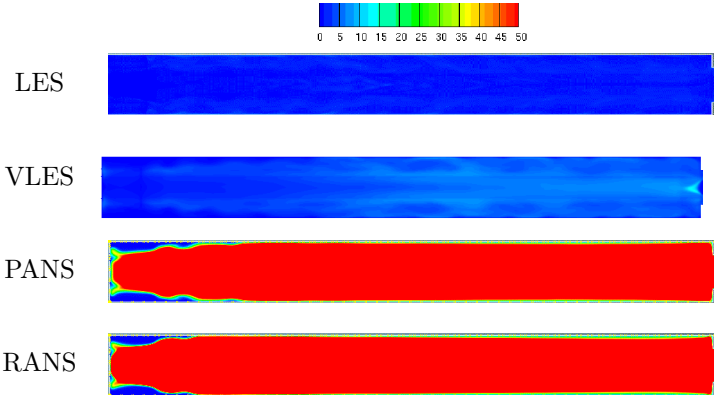

Figure 5.13: Modeling level (ν_t/ν) of applied turbulence models, large orifice

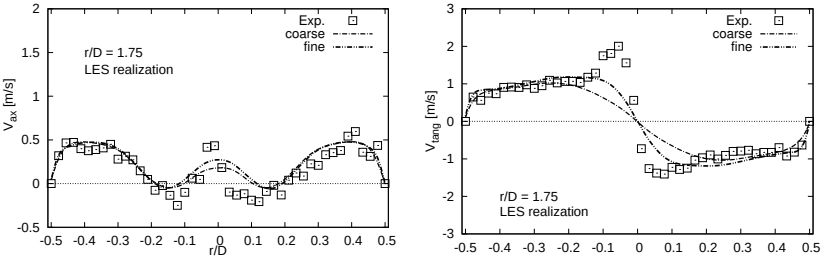

(a) Axial Velocity (b) Tangential Velocity

Figure 5.14: Mesh resolution study, LES, large orifice

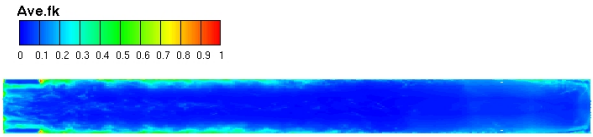

Figure 5.15: Modeling parameter f_k, PANS, eccentric orifice

the numerical realizations. The interesting phenomenon of helical vortex structure can be seen in the simulation results,that the the stream lines in the left-handed helical direction as the centric cases, and the ring zone in a right-handed direction due to the outlet eccentricity, see Fig 5.18. Besides, core jet and recirculation zone are built in a right hand helical form, which is captured by all filter based models.

In contrast to the former representations, the simulation utilizing PANS has very good agreement to the experimental data, where the three-layer structure is well captured as VLES and LES. Concerning the f_k value, Fig 5.15 shows a much smaller representation comparing to the one of large orifice, even though the mesh resolution of eccentric orifice has similar quality as the centric one. This can be interpreted as the pressure induced velocity fluctuation generated by the asymmetric outlet geometry, which can be regarded as geometric forcing for the flow system. Once the velocity fluctuation is strong, highly resolved turbulent kinetic energy is established and the f_k value reduces. The momentum equation is then able to capture more structure in the computational domain.

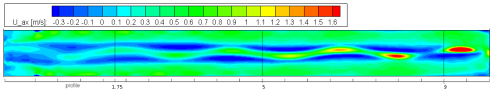

(a) Axial velocity

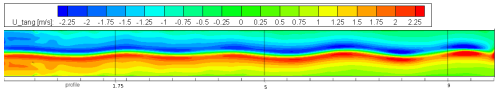

(b) Tangential velocity

Figure 5.16: Velocity contour, eccentric orifice, LES realization

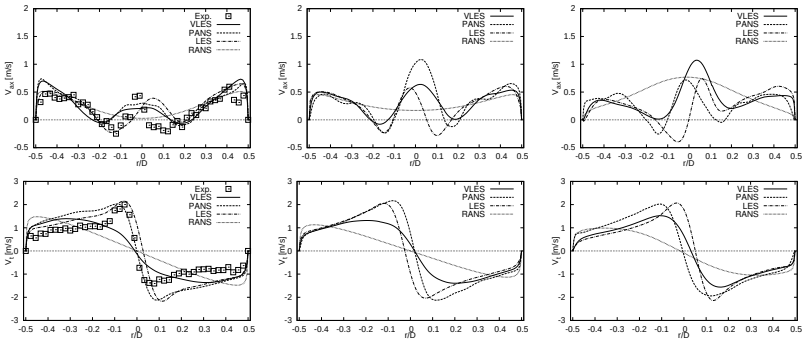

Figure 5.17: Eccentric exit orifice - axial (upper) and tangential (lower) velocity profiles at $z/D = 1.75$(left), 5(middle), 9(right)

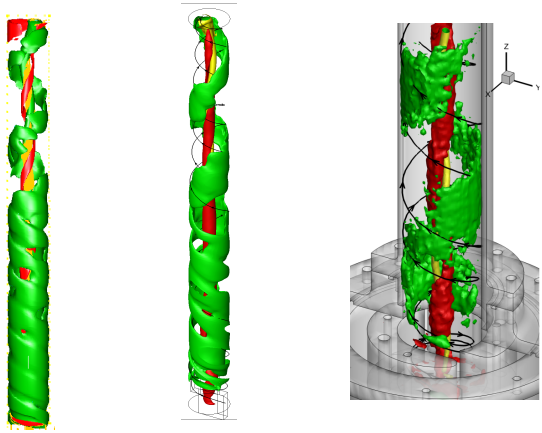

Figure 5.18: Iso-velocity contour of axial velocity, eccentric orifice, VLES(left), LES(middle), Exp.(right)

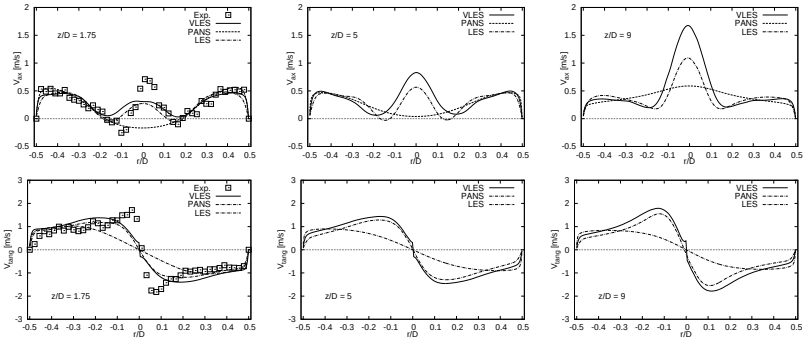

Figure 5.19: Refined mesh, large orifice - axial (upper) and tangential (lower) velocity profiles at $z/D = 1.75$(left), 5(middle), 9(right)

Summary

Concerning the flow features, the configurations of centric and eccentric orifice are very different. While the turbulent flow tends to a stable state in the centric geometry, it reaches an unstable condition in the outlet region due to the asymmetry shape in the configuration applying eccentric orifice. These characteristics have great influence on the evaluation of modeling parameter.

Generally speaking, the RANS k-ζ-f model is not capable of capturing the swirling properties due to the high anisotropy of turbulent characteristics. The k-ζ-f based hybrid eddy resolving model is supposed to adjust the characteristic velocity scale depending on the filtered or modeled length-scale. Comparing to the PANS realizations, the VLES applies the explicit suppression method to force the modeled length scale to be in the order of grid spacing, which is the main reason for similar results between VLES and LES regarding the velocity profiles.

PANS method works well if the geometric forcing is dominant in the flow configuration. In the region where unsteadiness is expected, PANS triggers the momentum equation to resolve more flow structure and the realization tend to be more towards the LES regime. On the contrary, this method tends to a stable state flow condition, where the resolved turbulent characteristics are small and modeled parts dominate. The calculation results then in RANS-like representations.

Results of LES and VLES are similar, where the LES results match even

better than VLES for the mean velocity profiles. To interpret this phenomenon, two conditions have to be concerned. 1st. the employed mesh is not fine enough for the LES Smagorinsky model, which denotes the tiny vortices appear in the numerical realization. These vortices are vanished when the mean values is evaluated, which declares the good agreement of LES results. 2nd. regarding the VLES method, the based RANS model is not capable to predict the swirling feature. This denotes the turbulent properties are out of estimation, including the lengthscale. Since the modeled lengthscale is not correctly predicted, the modeling parameter (F_k) obtains error of RANS model automatically. Nevertheless, since VLES method shrinks the modeling level explicitly in the momentum equation, the numerical results still show qualitative good agreement to the experimental data.

5.2 Generation and Destruction of Turbulent Tumbling Motions

The second significant phenomenon in the ICE is tumble, which is created due to the piston movement. The utilization of the tumbling flow has the effect of raising the combustion efficiency. The mechanism is described as following: During the intake stroke, air is sucked by the piston into the chamber and flows along the cylinder wall forming into a large rotational structure. The axis of tumble is perpendicular to the piston movement direction. This large scale vortex is further pressed to different scales of vortices during the compression stroke, which denotes the raises of turbulence level at the same time. The high turbulence level enhances the homogeneity of air-fuel mixture and efficiency of chemical reaction for the combustion process.

However, the generation and disruption of tumbling motion also enhances the level of cycle-to-cycle (CCV) variation. This phenomenon accompanies the tumbling motion and presents in every engine cycle different flow evolution due to the fluctuation both in the previous engine cycle and in the intake process. In the general engine configuration, which also takes the combustion process into account, the CCV has determinative influence weather the condition in the combustion chamber is favorable for stable ignition and flame propagation or not, especially in the spark plug region. CCV may even lead to an incomplete combustion process if the fuel-air mixture is either too lean or too rich.

For the interest of tumbling effects, a comprehensive realization was investigated by Marc et al. (1997, [61]) and Borée et al. (2001, [8]). They designed a generic engine with a square chamber and observed the generation and breakdown of tumbling vortex by applying PIV measurements. In their report, a clear two dimensional tumble is shown at the end of the intake stroke presenting itself as a potential vortex. During the compression stroke, two three-dimensional separation regions appear in the chamber corners due to the adverse pressure gradient induced by the vortex. Meanwhile, the turbulent level raises. By analyzing the kinetic energy in the chamber, they noticed the superiority of turbulent kinetic energy compared to the mean kinetic energy when the compression ratio (CR) is less than 2. Also, the turbulent kinetic energy correlates with the large flow scale, which is then amplified by the compression. At the beginning of the expansion stroke, the turbulent characteristics become the dominant effect in the combustion chamber.

Numerical investigations of turbulent tumbling flows and vortex breakdowns began in the 1980s. Gosman et al. (1985, [26]) applied the RANS approach to study the influence of piston configuration on the tumbling motion. Further, Le Roy and Le Penven (1998, [75]) applied the RSM for the experimental configuration of Marc et al. (1997, [61]) and compared the results with the standard k-ϵ model realizations. They aware the better agreement utilizing RSM by regarding the vorticity and turbulent kinetic energy.

However, it is not possible to capture the cycle-to-cycle variation(CCV) with a RANS regime, summarized by Haworth (1998, [34]) and Celik et al. (2001, [9]). Instead, they suggested the methodology of LES for the realizations of internal combustion engine systems. Among the LES investigations carried out during last decades, Toledo et al. (2007, [87]) applied the LES for the experimental configuration of Borée et al. (2001, [8]) regarded the generation and breakdown of turbulent tumbling flows. They concluded as a good agreement to the experimental data capturing the specific flow features such as the oscillation of intake jet, vortex precession an the peak of turbulent kinetic energy in the vortex core region, etc.

The principle of the eddy resolving method is to capture the instantaneous velocity fluctuation. This methodology should also be capable to deliver the proper quality as LES with respect to ICE configuration. Compared to the LES, ER models allow a more flexible mesh resolution. This advantage is capable to release the computational costs in the field of industrial applications. From this point of view, Hasse et al. (2009, [32]) applied

the SST-DES model for the realization of Borée's configuration and compared its realizations with LES and RANS results. They concluded to good agreement to the LES results and much more resolved flow structure than RANS representations.

Flow Configuration Description

The experimental investigation contributed by Borée et al. (2001, [8]) is illustrated in Fig 5.20(a). They designed a square-cylinder (with the cross-section $b \times b = 100 \times 100mm^2$) compression machine equipped with a flat head piston as a generic engine configuration to realize the generation and breakdown of a tumbling motion. This simple geometry, in comparison with a realistic internal combustion engine, provides well defined boundary conditions and good optical access. Detailed PIV (Particle Image Velocimetry) data, which corresponds to the evolution of the vortex induced during the intake process and its consequent compression, were generated. The data set comprises fluctuating and phase-averaged velocity and turbulence fields measured in the central plane of the compression chamber over 120 cycles. Kinematics of the piston movement is described by a sinusoidal function as:

$$a(t) = b - \frac{V_p}{\Omega}(1 + cos(\Omega t)) \tag{5.1}$$

with the maximum piston velocity $V_p = 0.809m/s$ and the engine speed $\Omega = 206$rpm. Where the a and b are the piston position at time t and the Bottom-Dead-Center (BDC) and Ωt denotes then the crank angle (θ), see Fig 5.20(b).

The length of the square cylinder volume at the Top-Dead-Center (TDC) corresponds to a_{min} of $25mm$. The piston stroke, which denotes the way the piston covers until reaching the bottom dead center at the end of the intake stroke, i.e. at the beginning of the compression stroke, amounts $75mm$. Accordingly, the compression ratio (CR), which represents the ratio of the maximum chamber volume to the current one, yields the values between 4 at TDC and 1 at BDC. The inflow system represents a channel functioning as an "intake/outtake valve" in a four-stroke engine, being opened during the intake stroke and the exhaust stroke and closed in all remaining expansion and compression cycles, see e.g. Fig 5.21. The dimensions of this eccentrically positioned channel are ($300mm \times 10mm \times 96mm$) for (length$\times$ height$\times$ width).

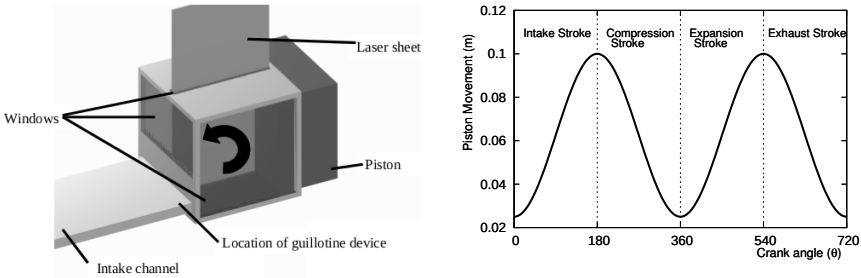

(a) Schematic of compression chamber (b) Piston displacement

Figure 5.20: Experimental setups of piston-cylinder assembly generic engine

The channel flow Reynolds number during the intake stroke corresponds approximately to 12000. It is assumed, according to the length/height ratio as 30, that the near-wall flow at the inlet of the compression chamber corresponds to the fully-developed turbulence.

Computational Details

Regarding the simulations, the computational domain (comprising the intake channel and compression chamber) corresponds closely to the experimental configuration. The channel was meshed by $253,080$ grid cells in total; the grid size of the compression chamber during the intake and exhaust strokes corresponds to $544,000$ cells (Nx, Ny, Nz=80, 85, 80), in which the mesh is refined in the y dimension in the region of inlet channel-compression chamber intersection. The chamber part of the solution domain accommodating the piston is deformable in accordance with the piston movement, see Fig 5.21. The maximum $y+$ values at the wall-next node along the chamber walls are between 0.7 and 0.9 (corresponding to $CA = 30^o$ and 180^o) and 1.3-1.6 (at $CA = 180^o - 360^o$). Fig 5.22(a) displays the field of the ratio of the characteristic grid spacing to the Kolmogorov length scale (Δ/η) representing one important grid quality assessment measure. This parameter takes the values well under 20.

For the settlement of boundary condition, atmospheric pressure was taken at the intake channel inlet plane. Regarding the filtering based models (PANS, VLES and LES), the initial velocity field was generated by

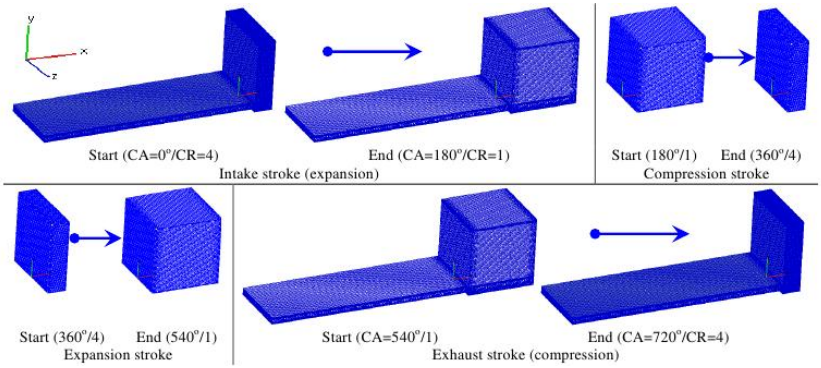

Figure 5.21: Illustration of calculation domain

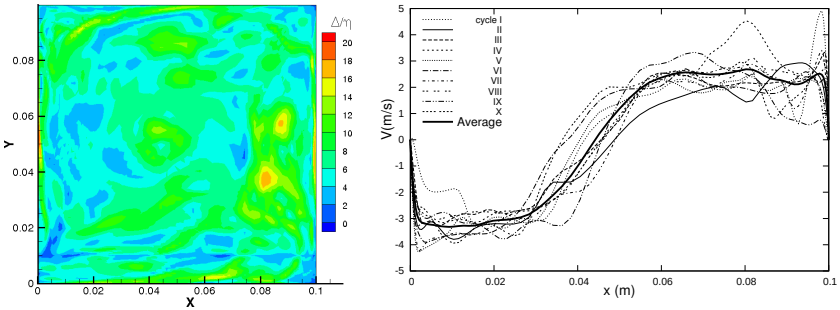

(a) Ratio of the characteristic grid spacing to the Kolmogorov length-scale at CA=180^o, LES

(b) Profiles of the instantaneous axial velocity and their phase-averaged counter part at CA=180^o, LES

Figure 5.22: Handling of computational setups

computing five full four-stroke cycles: intake stroke, compression stroke, expansion stroke and exhaust stroke. The phase-averaged results obtained by LES, VLES, and PANS methods correspond to ten further cycles; whereas, for the simulation employing RANS, only one cycle is regarded. Fig 5.22(b) illustrates the mean axial velocity obtained after phase-averaging of the instantaneous velocity field over ten cycles in the central vertical plane ($z = 0$). The results are compared and discussed as following:

Results and Discussion

Flow Structures

Five selected positions obtained by applying LES, VLES, PANS and RANS are taken for the abstraction of the generation and destruction of turbulent tumbling motion, shown in Fig 5.23, 5.25, 5.27, 5.29 and 5.31. The figures reveal a number of features typically associated with the highly-unsteady jet discharging from the inflow channel, separating from its sharp corners and transforming into a tumbling vortex being characterized by high velocity values. This tumbling motion occupies gradually the entire compression chamber.

After onset of the compression stroke, its systematic retardation takes place; the most intensive deceleration occurs along the chamber/piston walls propagating up to the vortex core; one notes the flattening of the velocity profiles in the largest portion of the cross-section. The profiles of all variables are depicted across the tumbling vortex core being characterized by the most intensive turbulence production. The maximum of the kinetic energy coincides with the position where the velocity components take zero value.

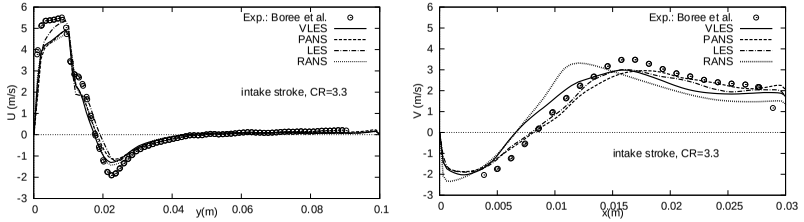

(a) Vertical cross profile (b) Horizontal cross profile

Figure 5.23: Velocity profiles cross over tumble core, Intake Stroke CR = 3.33

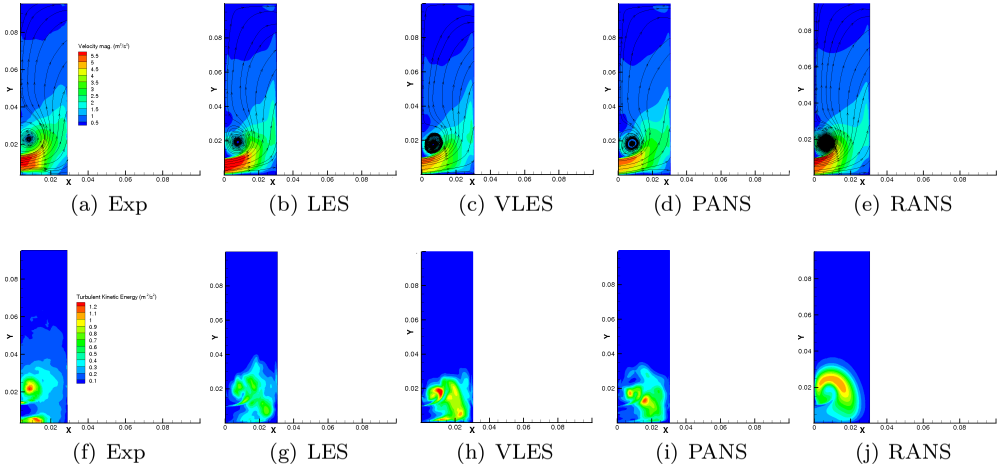

(a) Exp (b) LES (c) VLES (d) PANS (e) RANS

(f) Exp (g) LES (h) VLES (i) PANS (j) RANS

Figure 5.24: Velocity magnitude(upper) and turbulent kinetic energy(lower)

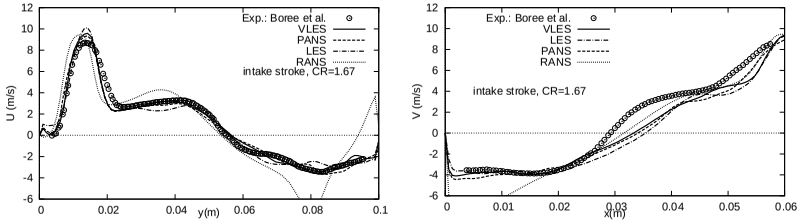

(a) Vertical cross profile (b) Horizontal cross profile

Figure 5.25: Velocity profiles cross over tumble core, Intake Stroke CR = 1.67

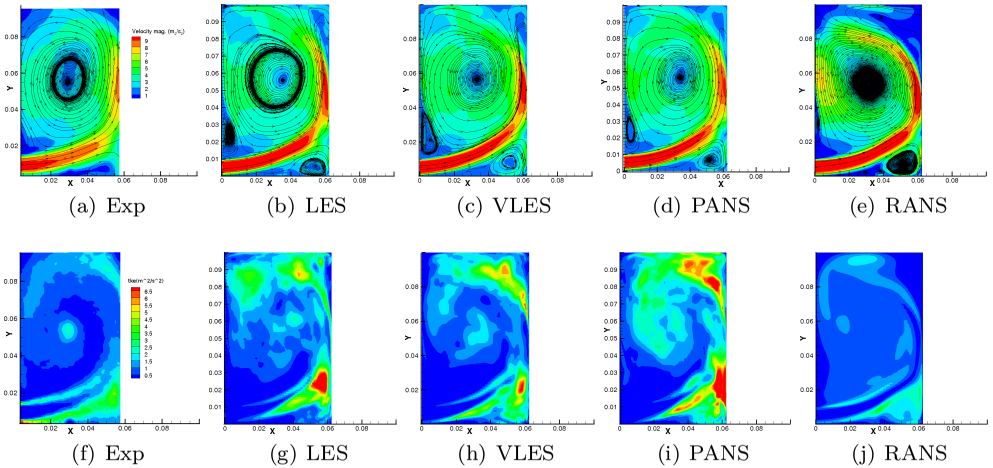

(a) Exp (b) LES (c) VLES (d) PANS (e) RANS

(f) Exp (g) LES (h) VLES (i) PANS (j) RANS

Figure 5.26: Velocity magnitude(upper) and turbulent kinetic energy(lower)

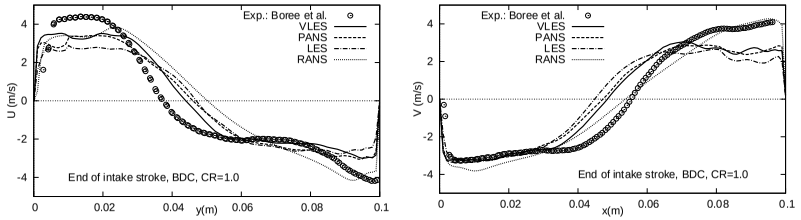

(a) Vertical cross profile (b) Horizontal cross profile

Figure 5.27: Velocity profiles cross over tumble core, Intake-Compression BDC, $CR = 1$

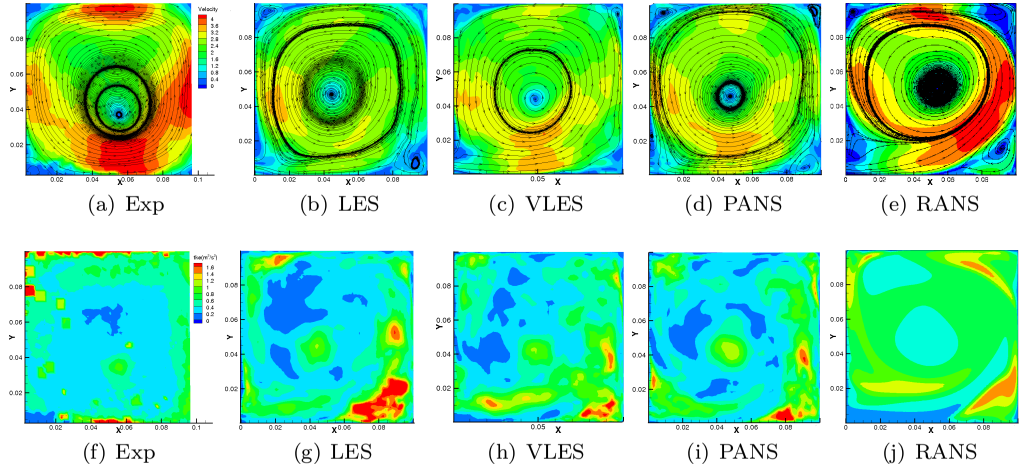

(a) Exp (b) LES (c) VLES (d) PANS (e) RANS

(f) Exp (g) LES (h) VLES (i) PANS (j) RANS

Figure 5.28: Velocity magnitude(upper) and turbulent kinetic energy(lower)

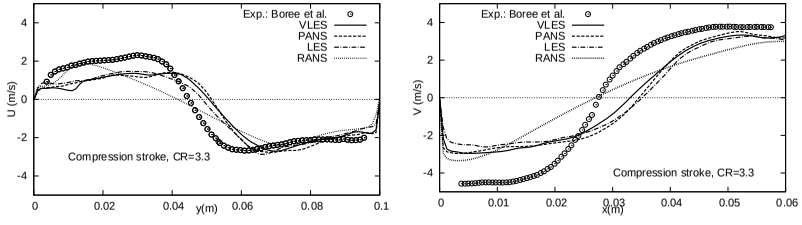

(a) Vertical cross profile (b) Horizontal cross profile

Figure 5.29: Velocity profiles cross over tumble core, Compression stroke, $CR = 1.67$

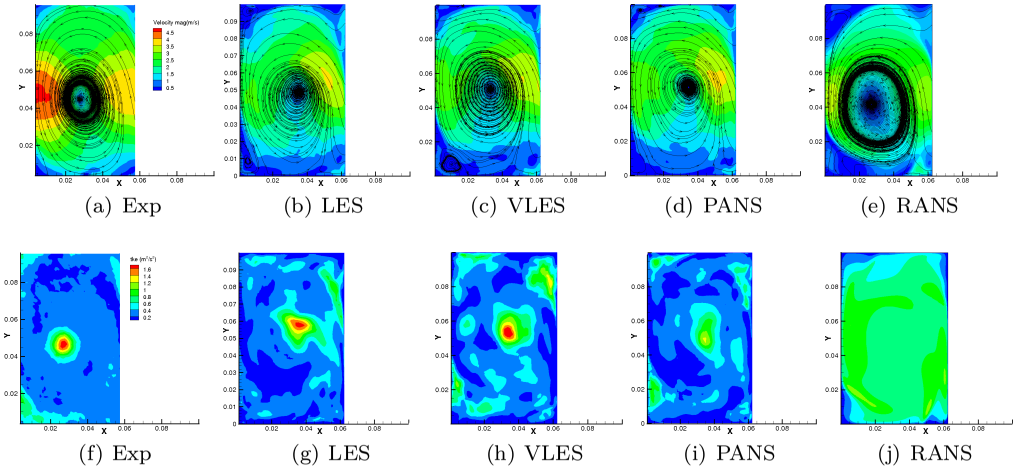

(a) Exp (b) LES (c) VLES (d) PANS (e) RANS

(f) Exp (g) LES (h) VLES (i) PANS (j) RANS

Figure 5.30: Velocity magnitude(upper) and turbulent kinetic energy(lower)

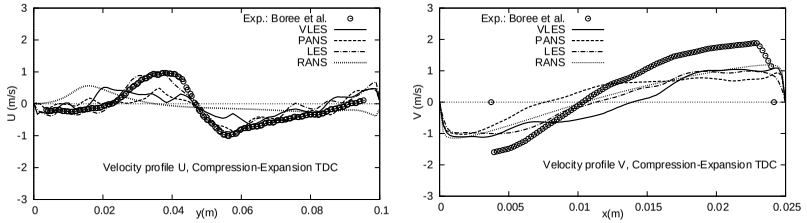

(a) Vertical cross profile (b) Horizontal cross profile

Figure 5.31: Velocity profiles cross over tumble core, Compression-Expansion TDC, $CR = 4$

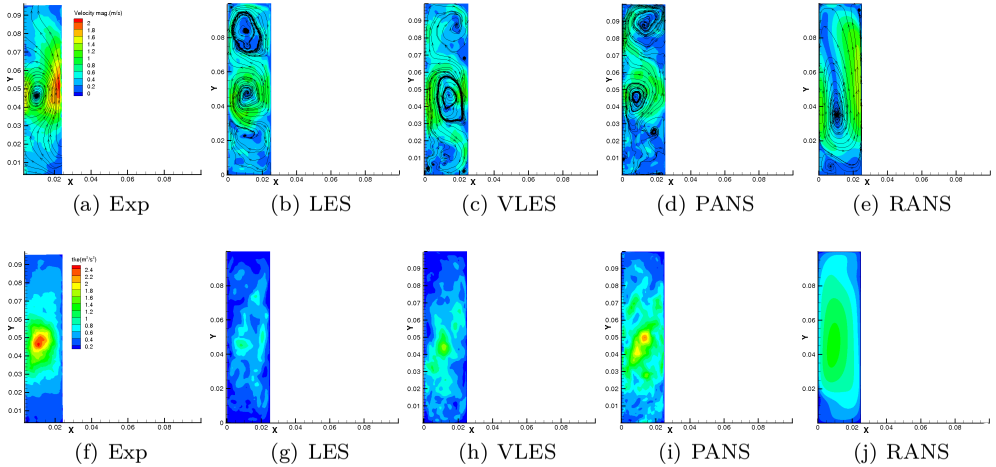

(a) Exp (b) LES (c) VLES (d) PANS (e) RANS

(f) Exp (g) LES (h) VLES (i) PANS (j) RANS

Figure 5.32: Velocity magnitude(upper) and turbulent kinetic energy(lower)

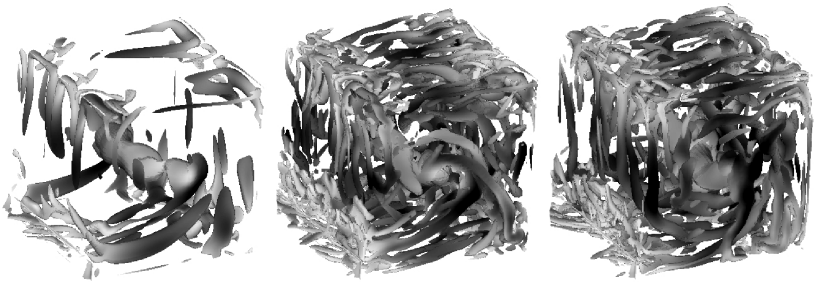

(a) RANS (b) PANS (c) VLES

Figure 5.33: 2^{nd} invariant of velocity gradient, $Q = 35,000$, end of intake stroke, $CR = 1.0$

Numerical Realizations

The first impression of numerical realizations is the captured velocity structures. Fig 5.33 shows the Q invariant of RANS, PANS and VLES at the end of the intake stroke. It is recognized that PANS and VLES are capable to resolve more structures than RANS. These fluctuating characteristics lead to the representation of cycle-to-cycle variations, which is build by the phase averaging of every realised cycle. Whereas, RANS method is only capable to realize the main structure due to the based modeling strategy.

Regarding the mean velocity profiles, the realizations of all the applied models have qualitative good agreement with the experimental data during the intake stroke, whereas the tumble core is captured in slightly different positions and is presented as shifts in the plots of the velocity profile. During the compression stroke, the qualitative agreement weakens where the averaged velocity profiles become very fluctuating at the end of compression stroke. This denotes that more realization cycles are needed for the phase averaging representation.

In the plots of turbulent kinetic energy, a peak can be noticed where the tumble core locates. This phenomenon is mainly the representation of cycle-to-cycle variations, where the position of the tumble core varies in every cycle due to the fluctuated flow structure both in the inlet pipe and in the chamber during the previous exhaust and intake stroke. However, this phenomenon can not be captured by RANS due to the applied averaging principles.

Concerning the modeling technique, Fig 5.34 shows that the modeling

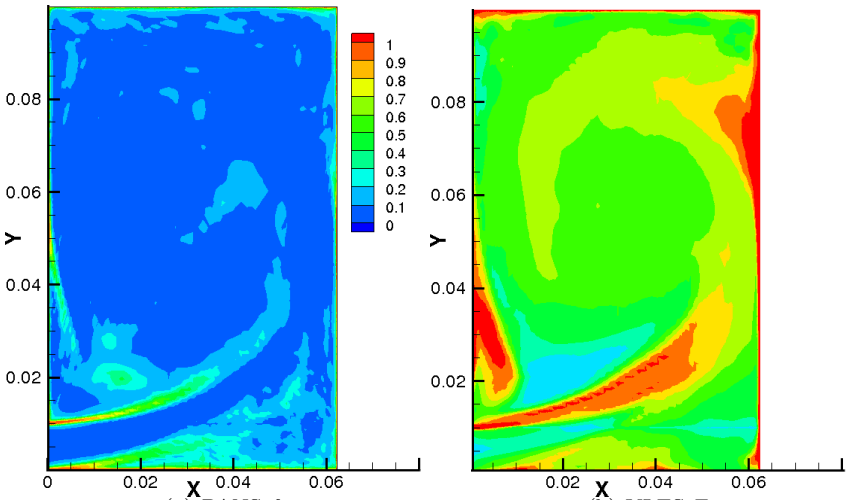

(a) PANS:f_k (b) VLES:F_k

Figure 5.34: Modeling parameter of ER models, intake stroke, $CR = 1.67$

parameters of the applied ER models tend to unity in the near wall region and decrease in the outer zone, which suits the general purpose of ER modeling method. A confusing phenomenon appears in the main flow structure zone during the intake stroke, where the f_k of PANS reaches very small values. This would be interpreted as the low required modeling level in the jet zone, whereas it is not really reasonable. The low f_k value of PANS calculation is mainly due to the improper estimation of averaged velocity $\overline{U}_i$ which is required in Eq 2.43. Since this term is taken as the time averaged values but not the phase averaged properties, any changes in the boundary condition or calculation system lead to the overestimation of resolved turbulent kinetic energy. f_k is then reduced to very small values.

A correct manner dealing with this issue is to apply the phase averaging for the estimation of f_k. However, carrying out this concept is extremely expansive because it requires many cycles to first generate the averaged velocity, which is not suitable for the general purpose developing ER models.

Another possibility is to apply the transport model for the resolved turbulent kinetic energy. Although this idea strains the calculation by solving one more transport equation, the costs are restricted and the calculation can keep its robustness, which seems as a reasonable way handling such is-

sues. Currently, this concept is still under development; a concrete solution is not available yet.

Comparing to PANS, VLES focus on the current modeled values to estimate the modeling factor. The requirement of averaged characteristics is then avoided. The representation of F_k shows relatively large values in the jet zone since the local Re raises during the intake stroke, for which higher modeling level is expected. This becomes a realistic compromise dealing with time dependent configuration concerning eddy resolving turbulence modeling strategy.

Summary

The cycle-to-cycle variation is the most significant phenomenon appearing in piston-like configurations, which is represented as a peak of turbulent kinetic energy in the tumble core region by applying the averaging procedure for single crank angle position. Generally, most turbulence models are capable to capture the velocity profiles in a qualitatively correct manner, whereas RANS cannot capture the variation in the tumble core region due to the ignorance of flow fluctuations in the inlet pipe and in the chamber during the exhaust and intake stroke. Besides, RANS yields high kinetic energy and lower turbulent kinetic energy during the intake and compression stroke, which may lead to higher error in the further applications, e.g. spray, combustion.

Filter based models are beneficial compared to the RANS method. Since the flow structures are captured, the cycle-to-cycle variations can be shown in the realization of the turbulent kinetic energy. The PANS and VLES apply the transport model for the subgrid-scale properties, which handle the critical regions by applying higher modeling ratios. These are the more reliable modeling strategies than the algebraic Smagorinsky model.

However, the PANS method in this work applies the improper averaged properties estimating the modeling parameter, which leads to extremely small f_k values in the main flow structure. This disadvantage may either lead to the instability of calculations or in the quality of results. Compared to this, VLES avoids the requirement of phase averaging properties, which can be regarded as a proper strategy dealing with the time dependent computational domain or boundary conditions.

6 Airflow in a realistic IC-Engine Configuration

As far as aerodynamics in the IC engine configuration, turbulent tumbling and swirling flow are the most significant phenomena is concerned, in which different scales of flow structure appear. These features induce the flow evolution varied for every single cycle, which is noticed as cycle-to-cycle variation(CCV).

The technical influence of CCV is briefly mentioned in the last chapter, that it can lead to the rise of fuel consumption and pollutant emission, or even misfire in fuel-air mixture that is too lean. Taking the whole engine system into account, every mechanism in the engine is responsible for CCV. These random variations are considered as noise in the combustion process which affects the stability of burning condition. From this aspect, numerous investigations are published to discuss this problem, e.g. Kaminski et al. (2004, [41]) traced the pressure variation and tried to estimate the noise level using analytical methods. Matsumoto et al. (2007, [62]) analyzed the pressure data during combustion and proposed the method to stabilize the pressure fluctuation.

Among the works of Heywood (1998, [36]), Ozdor et al. (1994, [67]), etc., Vermorel et al. (2009, [89]) summarized the causes of CCV in the SI engine system to the variation in ignition, fuel-air mixture, turbulence and mean flow pattern in the combustion chamber. All these phenomena are strongly coupled with each other, and dependent on the engine geometry and operation individually. In the review of Ozdor et al. (1994, [67]), he estimated a 10% rise of power output for the same fuel consumption if cyclic variations could be eliminated. Nowadays, cycle-to-cycle variation remains a difficult and important issue in the engine design.

Within all the possible conditions which causes cyclic variation, mixing, ignition, flame propagation, etc., are all based on the existing flow circumstance, i.e. air flow becomes the first assignment in the analysis of engine process. Once the aerodynamic effects are understood, further investigations regarding multiphase flow and chemical reaction are on the conceivable level.

For a thorough comprehension of in-cylinder flow and the related chemical process in a realistic engine geometry, several investigations are carried out. Voisine et al. (2011, [93]) focused on the tumbling motion and its corresponding CCV using PIV measurement. They stated that the tumbling jet structure develops along the cylinder wall and interacts with the moving piston during the intake stroke. In the beginning of the compression stroke, the flow along the piston diverges away from the impact region and roll-up, where a very strong CCV of vertical propagation is observed. During the breakdown process in the compression stroke, the tumbling vortex transforms to the large scale CCV and small scale turbulence. By applying the phase averaging method, the turbulent kinetic energy becomes dominant in the chamber, for which they showed that about 30% of the turbulent kinetic energy consist of the cycle-to-cycle variation at the compression-expansion TDC.

In the last decades, CFD was become a useful tool analyzing flow configurations. The three-dimensional realizations contribute to more possibilities in the field of engine design. However, the standard applied RANS modeling technique is incorrect when the cycle-to-cycle variation is under consideration, this is also referred to in the last chapter.

Instead of RANS, LES and relevant filtered modeling strategies become a promising method, analyzing IC engine relevant configurations. Several studies focused on LES have been conducted in the past. Vermorel et al. (2007, [89]) executed the calculation regarding combustion process. They recognized the qualitative and quantitative agreement capturing the CCV as in the experiment. Vitek et al. (2011, [92]) extended the numerical settlements and concluded that the boundary conditions are less important affecting the thermo- and CCV characteristics.

Concerning all the mechanism appearing in the IC engine, the numerical validation of single phase air flow should be first carried out for the further modeling of mixture and chemical reaction, Vitek et al. (2012, [91]), Goryntsev et al.(2009, [25]) and Vermorel et al. (2007, [90]) contributed in this subject but there were no experimental data available. Baumann et al. (2013, [7]) validated the configuration of Baum et al. (2013, [6]), where the agreement of numerical results to experimental data is highly convincing.

The utilization of hybrid turbulence model in engine geometry was carried out by Hasse et al. (2010, [33]). In their report, SST-DES is employed for air flow in the four-stroke SI-like engine. On the top of reaching matching numerical and experimental results, they also analyzed the applied turbulence model and recognized the modeling factors in the intake port

are very different as in the combustion chamber. In their results, RANS dominates in the near-wall region of the engine cylinder and in the intake port where the Reynolds number is very high due to the piston suction.

Nevertheless, the filter-based turbulence modeling technique provides a promising possibility to capture the flow configuration especially for complex computational domains, such as IC engines. Depending on the mesh resolution, the flow structure is either captured or modeled. Thus, multi-scale flow properties can be achieved by using this modeling technique.

6.1 Experimental Configurations

Thorough experimental measurements of air flow in the engine configuration are carried out by Baum et al. (2013, [6]). They designed the test bench to enable reproducible operations for large variations of measuring quantities. In the schematic shown in Fig 6.1(a), the air intake is modified by the mass controller (MFC) for the relative humidity of 1.8%. Then, a pneumatic valve (PV) and large plenum volume (P2) are applied to minimize the pressure perturbations caused by the single cylinder operation. After the air intake flows through the heater (H), two plenums (P3, P4) connected to the intake and exhaust port are utilized for the sound reduction.

For the engine system, the intake and exhaust ports are designed to provide the simplified boundary surface geometry, where the air flow separates due to the Y-shaped manifold as a dual-port intake system of the engine, see Fig 6.1(b). A single-cylinder SIDI optical engine is applied for the experimental measurement. The cylinder head is equipped with a side-mounted injector, which is inactive for the measurement. Also, a spark plug is replaced so the cylinder head surface remains flat, where the intake system is attached to generate the tumbling flow in the engine cylinder.

During the piston movement, the optical engine operates with a maximal geometric compression ratio of 8.5 with the engine speed of 800 rpm. The experimental data is averaged over 1800 cycles for the ensemble-averaging and standard variations. Details of the valve lifting configuration as well as the engine geometry and setup are listed in Table (6.1), Fig 6.2(a) and 6.2(b) .

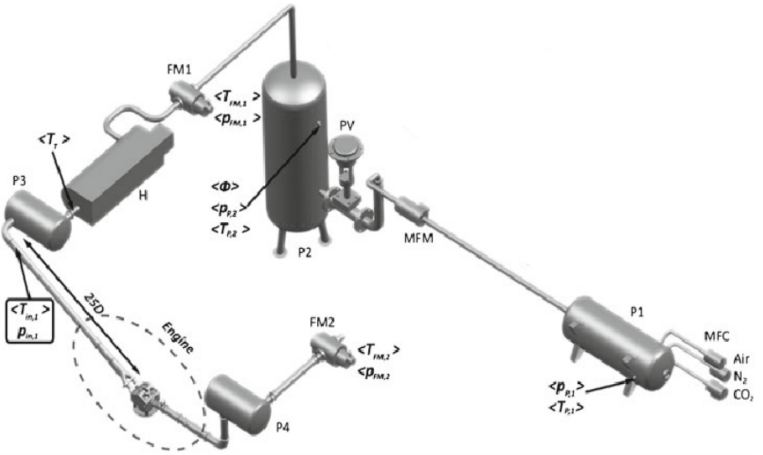

(a) Entire measurement system

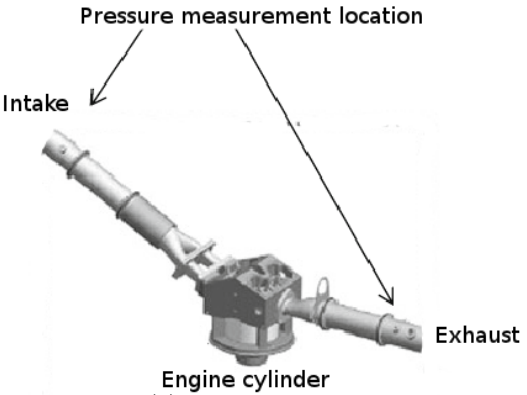

(b) Illustration generic engine

Figure 6.1: Schematic of experimental setups

6.2 Numerical Setups

Corresponding to the experimental configuration, the computational domain consists of the single engine cylinder with its intake and exhaust manifold in the same dimension. The manifolds are constructed from the

	value	unit
Bore	86	mm
Stroke	86	mm
Clearance height	2.6	mm
Conrod length	148	mm
Intake valve opening	325	CA^o aTDC
Intake valve closing	125	CA^o bTDC
Exhaust valve opening	105	CA^o
Exhaust valve closing	345	CA^o bTDC
Engine speed	800	rpm
Compression ratio	8.5	-
Intake pressure	95	kPa
Intake temperature	295	K

Table 6.1: Technical details of optical engine

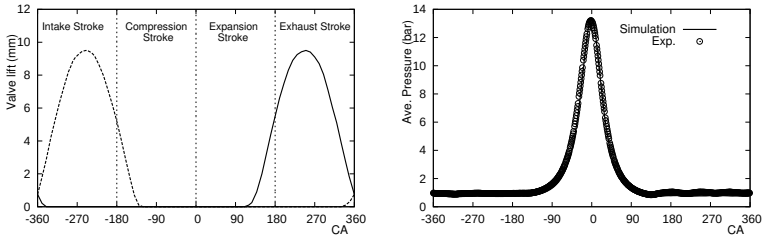

(a) Intake and Exhaust valve lifts (b) Averaged in-cylinder Pressure

Figure 6.2: Details of generic engine configuration[6]

location where the pressure measurement is carried out.

Computational domain

The generation of the computational domain is utilized by AVL Software package FAME Engine Plus, which establishes the moving numerical mesh in an unstructured manner with hexahedrol cells from the given CAD data. For the engine geometry, different levels of refinement are set as the realistic mesh generation, see Fig 6.4(a).

Regarding the moving domain, the generated meshes are saved for every 5 CA. Within this interval, the mesh cells are stretched according to the

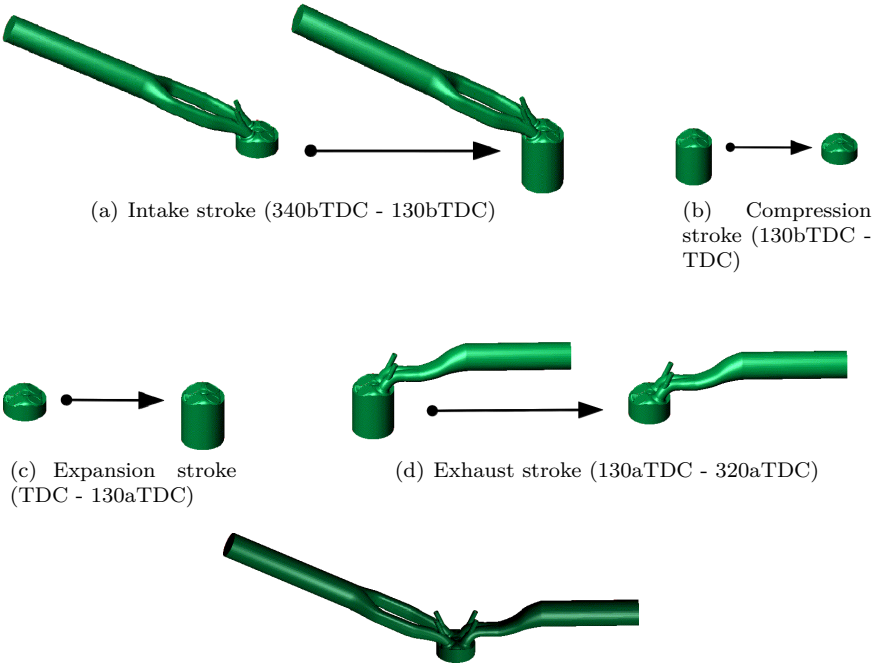

(a) Intake stroke (340bTDC - 130bTDC)

(b) Compression stroke (130bTDC - TDC)

(c) Expansion stroke (TDC - 130aTDC)

(d) Exhaust stroke (130aTDC - 320aTDC)

(e) Opened valves region (exhaust-intake 360bTDC)

Figure 6.3: Numerical domain of generic engine configuration

piston movement. The numerical procedures within the interval are carried out as the moving mesh as described in Chapter 3.2.1. After the interval region, the numerical results are interpolated for the next saved mesh and the same process keeps being carrying out .

Since the aerodynamics in the engine cylinder is the focus, the computational domain is reduced to the engine cylinder during the compression and expansion stroke, where the valves are closed. During the intake and exhaust stroke, the pipes are not taken into account, for which the corresponding valves are closed. A brief illustration is shown in Fig 6.3

The quality of mesh resolution is verified by the calculated y^+ and Δ/η value (e.g. Fig 6.5(a) and 6.5(b)) for several crank angle positions. Details of the computational domain are listed in Table (6.2).

The implicit Euler method and MINMOD are employed for the time

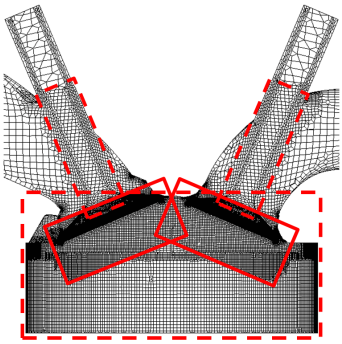

(a) Mesh refinement region

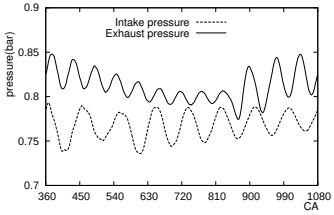

(b) Pressure boundary condition on intake and exhaust valve

Figure 6.4: Numerical construction

Crank Angle Degree	total cells	max. Δ/η	max. y^+
270 bTDC	2,564,878	55	11
90 bTDC	1,393,286	25	11
TDC	1,072,017	23	34
90 aTDC	1,393,438	16	8
270 aTDC	2,564,878	48	6

Table 6.2: Details of numerical mesh quality.

derivative term and differencing scheme as the regular computational setup respective to the engine configuration. The time step size is not restricted by the Courant number but rather by the numerical stability. Settlements of boundary conditions are taken from the modified pressure values, reported by Baumann et al. (2013, [7]), for the intake and exhaust valve, see Fig 6.4(b).

LES, PANS, VLES and RANS k-ζ-f model are applied for the configuration to ascertain the model's behavior and suitability. For the calculation, the LES realization after one engine cycle is taken as initial conditions. The averaging begins after one engine cycle execution of applied turbulence model for 13 cycles of filter-based models as well as one for RANS. The computational results are summarized in the representation of velocity and standard variations, which refers to the cycle-to-cycle variations, of dif-

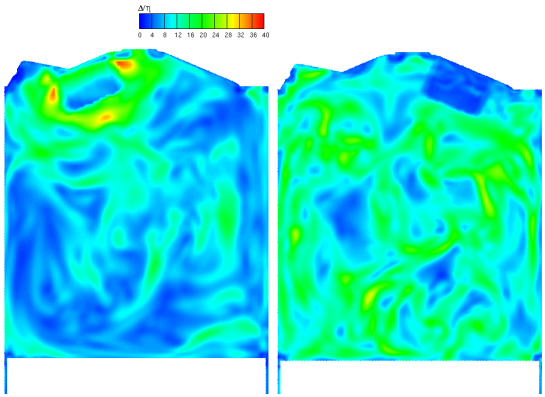

(a) 180^o bTDC (b) 180^o aTDC

Figure 6.5: Illustration of grid quality Δ/η

ferent positions in the engine geometry corresponding to the experimental data.

6.3 Results and Discussion

The first impression of numerical representation is the instantaneous flow structure captured by the momentum equation. As expected, the realizations of VLES and LES show very different scales of flow structure compared to RANS (Fig 6.6), where the calculation of PANS cannot reach the convergence within the first certain iterations. Therefore, none of the results of the PANS method can be presented.

6.3.1 Flow Structures

Since the computational system is time dependent, the phase-averaging procedure is the proper method to analyze computational results. Here, realizations of VLES, LES for 13 cycles and RANS for one cycle are compared with the experimental data in the representation of mean velocity profile and Reynolds stress components with respect to standard variation. Four crank angle positions are selected with respect to the intake, compression, compression-expansion TDC and exhaust stroke.

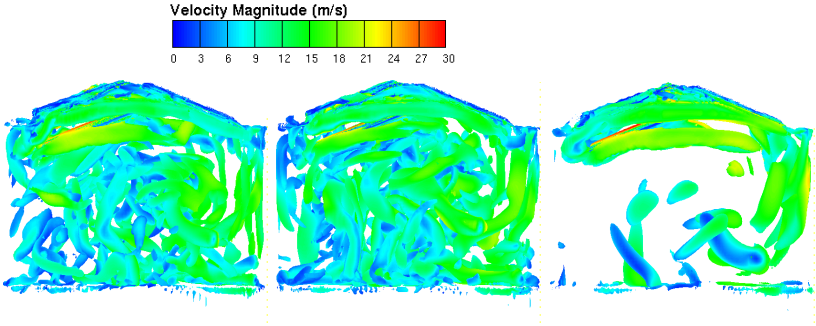

(a) VLES (b) LES (c) RANS

Figure 6.6: Iso-surface of Q invariant, $Q = 3 \times 10^6$, 270^o bTDC

270^o bTDC (Intake Stroke)

During the intake stroke, both the intake valves are opened. Air is sucked into the cylinder due to the piston movement, the high velocity structure builds in a jet form along the cylinder wall. This intake jet, which is induced by the thin cleft of opened valves and piston suction, extends to the piston top and generates a left handed tumbling motion on the central symmetric plane. The tumble core, which is depicted by a perforated red box, can be observed at the right side of the central axis, see Fig 6.7.

Since the valves and piston are both moving according to the crank angle, the corresponding intensity of intake jet in the valve region varies greatly. When the former intake jet, which is redirected by the piston top, encounters the later one, stagnation occurs. This phenomena can be observed as the deep blue colored area on the left of the tumble core in Fig 6.7.

The turbulent properties on the symmetric plane are represented in the Reynolds stress elements ($\overline{uu}$ and $\overline{vv}$) shown in Fig 6.9. In which, the most remarkable region appears in the stagnation zone. This denotes a high order of uncertainty when the later intake jet impinges the reversed flow.

Regarding the numerical results, cross plots along different y-lines on the symmetric plane are shown in Fig 6.8. In general, numerical representations of the velocity profile matches those of the experimental data; the tendencies of velocity evolution are well captured by VLES and LES. In this case, RANS underestimates the recirculation zone on the left side of cylin-

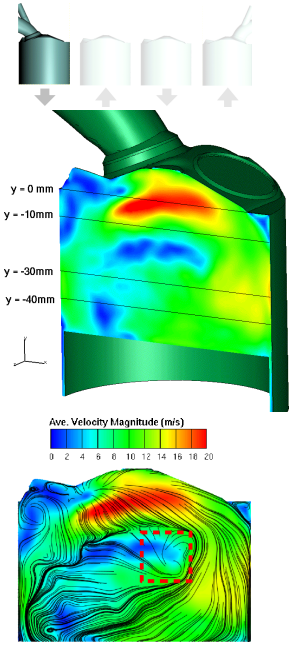

Figure 6.7: Contour of mean velocity magnitude

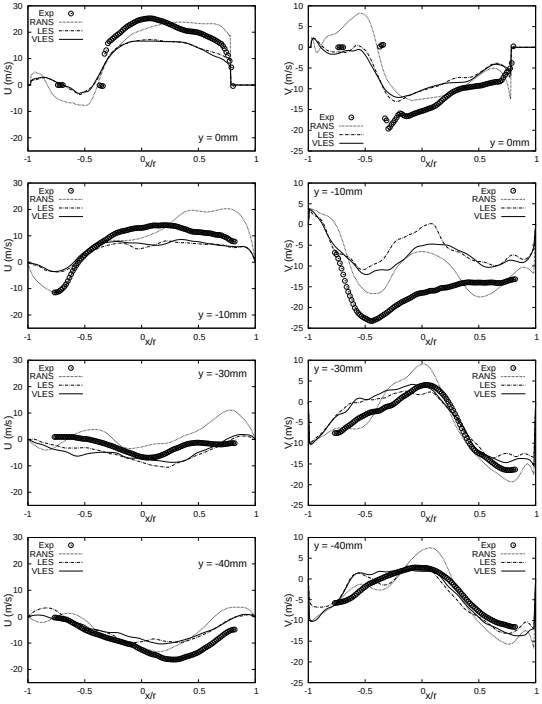

Figure 6.8: Mean velocity profile, intake stroke, 270^0 bTDC

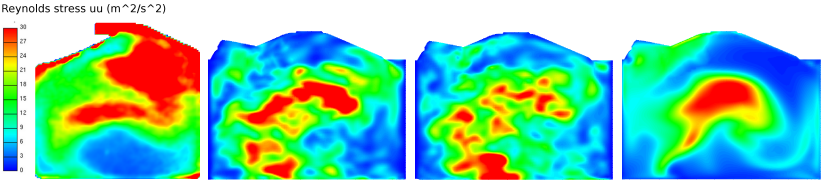

(a) Exp. (b) VLES (c) LES (d) RANS

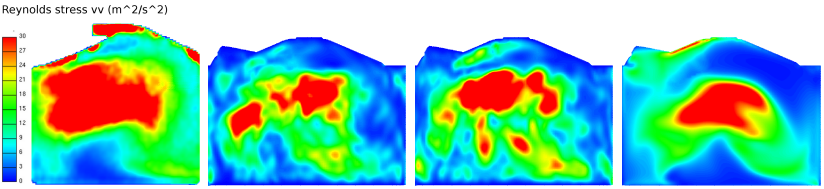

(e) Exp. (f) VLES (g) LES (h) RANS

Figure 6.9: Reynolds stress components $\overline{uu}$(upper) and $\overline{vv}$ (lower), intake stroke, 270^0 bTDC

der head and thus overestimates the tumble movement on the right part of symmetric plane. Regarding the Reynolds stress, results of VLES and LES are very fluctuated. This is mainly due to the insufficiently realized cycles, in which the numerical results are insufficient to build statistically competent representations. Nevertheless, the realizations on the symmetric plane show similar tendencies, which is also well captured by LES and VLES.

90^o bTDC (Compression Stroke)

During the compression stroke, all the valves are closed. The piston pressing movement becomes the characteristic factor effecting the flow structure. As in Fig 6.10, the tumbling motion remains on the side of the symmetric plane and the tumble core is shifted slightly more to the right. In general, the velocity magnitude in the compression stroke is much smaller than in the intake process. The highest velocity region becomes closed to the piston top since the geometric movement becomes the only forcing term in the domain. For the turbulent properties, the turbulent kinetic energy is more homogeneous in compression process than in the intake stroke, while the CCV is still noteworthy and has the maximum in the tumble core region.

In the numerical representations, the velocity profiles parallel to the X-axis match well with the reference data, where it is overestimated in the piston top region. A realistic representation of Reynolds stress components can also be seen in the VLES and LES results, although more samples are still needed though. However, the RANS method predicts totally different behavior compared to the filtered based models. The qualitative agreement is weak, see Fig 6.12.

In Fig 6.12, the cyclic variations can be observed on the right part of the symmetric plane, where the $\overline{uu}$ reaches the peak in the tumble core region. This phenomenon is well captured by VLES and LES with slightly varied tumble core position.

Compression-Expansion TDC

In most ICE systems, fuel-air mixture is ignited on the compression-expansion TDC or in the early expansion stroke, where the velocity magnitude and turbulent properties in the cylinder reach the most homogeneous state, see Fig 6.13(c). In this crank angle position, the large scale tumbling motion is almost collapsed into small scale vortices and the instantaneous velocity becomes very chaotic, see Fig 6.13(a). Here, a tumble core can still be

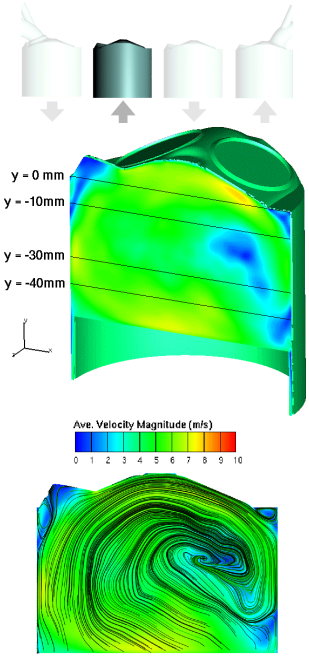

Figure 6.10: Velocity magnitude contour

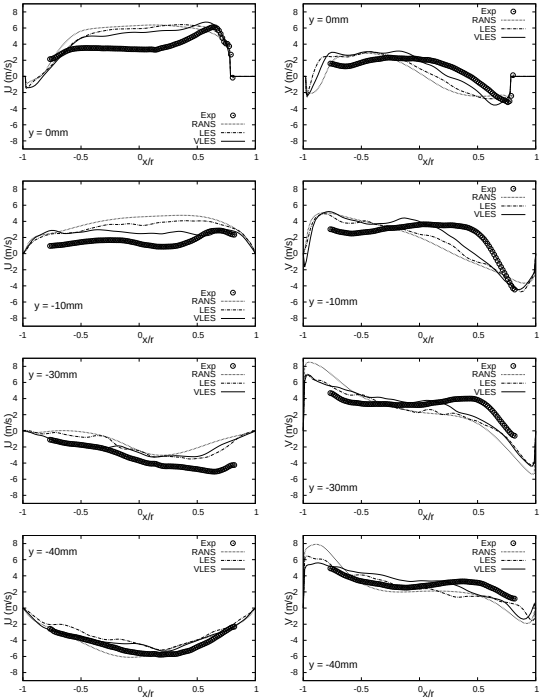

Figure 6.11: Mean velocity profile, compression stroke, 90^0 bTDC

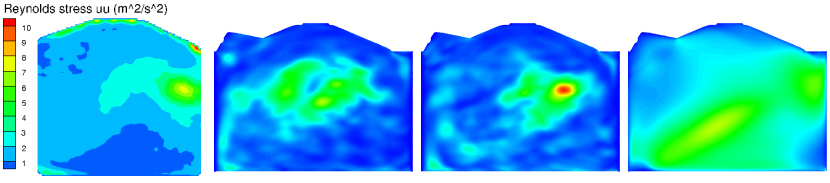

(a) Exp. (b) VLES (c) LES (d) RANS

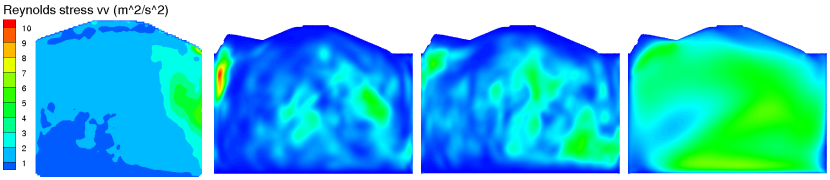

(e) Exp. (f) VLES (g) LES (h) RANS

Figure 6.12: Reynolds stress components $\overline{uu}$(upper) and $\overline{vv}$(lower), compression stroke, 90^0 bTDC

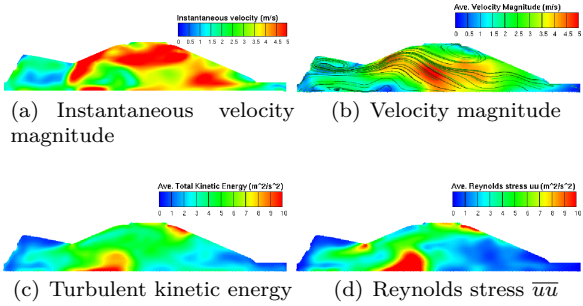

(a) Instantaneous velocity magnitude (b) Velocity magnitude

(c) Turbulent kinetic energy (d) Reynolds stress $\overline{uu}$

Figure 6.13: Velocity profiles (upper) and turbulent properties of TDC, VLES realization

recognized in the cylinder head region, since it is the only room for the reversed flow from the piston top. The velocity contour denotes that the flow structure does not depend on the intake stroke at all.

Cyclic variations are realized in Fig 6.13(d), where the Reynolds stress $\overline{uu}$ is remarkable in the cylinder head region around the tumble core. This might have great influence if the combustion process is also taken into account. However, the presence of injector may also influence the flow structure. Thus, deeper investigations of further effects are still necessary.

270^o aTDC (Exhaust Stroke)

In the exhaust stroke, both exhaust valves are opened and the air is pressed by the piston out of the cylinder. During this process, piston movement is the main source term, the vertical velocity component becomes the dominant characteristics in the chamber; A recirculation zone appears on the left side of the symmetric plane due to the asymmetric opened valves.

The turbulent properties in the exhaust stroke remain very chaotic. This feature has great influence on the flow structures in the intake stroke for the next engine cycle. A well prediction in the exhaust stroke may ensure the realization in the intake stroke in a realistic manner.

The numerical results in the exhaust process have, in general, similar evolution presented in the cross plots, see Fig 6.15. For one, VLES and LES have very good agreement capturing the velocity profiles. While RANS overestimates the recirculation zone, the vertical velocity component is underestimated.

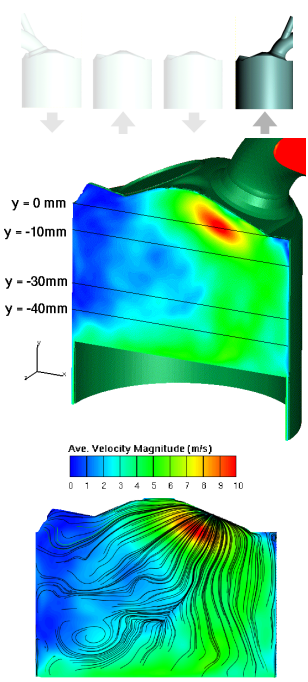

Figure 6.14: Velocity magnitude contour

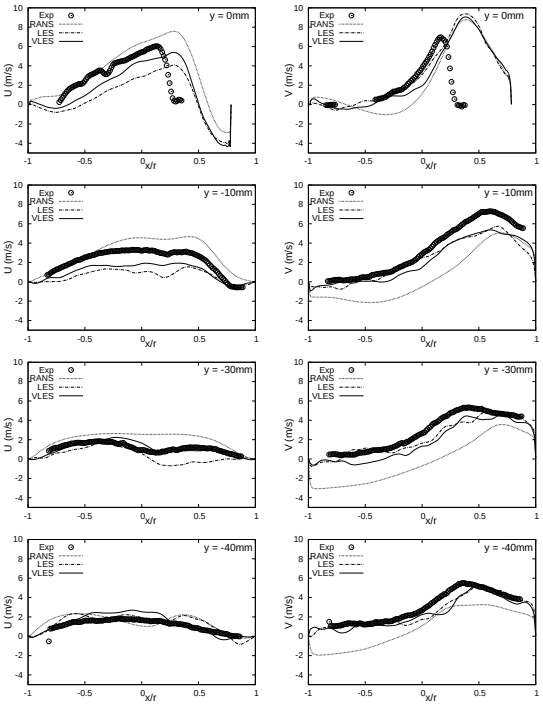

Figure 6.15: Mean velocity profile, exhaust stroke, 270^0 aTDC

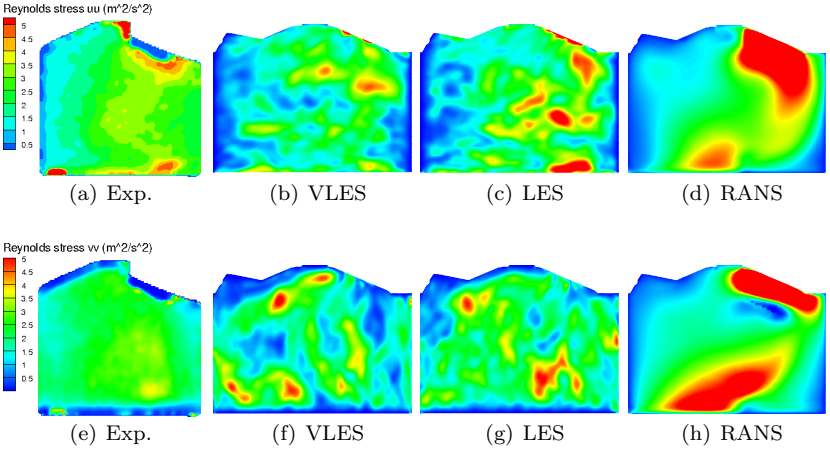

(a) Exp. (b) VLES (c) LES (d) RANS

(e) Exp. (f) VLES (g) LES (h) RANS

Figure 6.16: Reynolds stress components $\overline{uu}$(upper) and $\overline{vv}$ (lower), exhaust stroke, 270^0 aTDC

6.3.2 Modeling Analysis

VLES

Fig 6.17 shows the modeling factor F_k of VLES for three selected crank angle position respectively to intake, compression and expansion stroke. As it is also shown in the previous chapters, the F_k develops from unity in the near-wall region to the lower values in the cylinder center. In the intake jet region, where strong coherent structure and high velocity magnitude dominate, is also covered with high F_k values. This can be interpreted as the higher modeling level is required for the higher Re region, where the inertial subrange in the energy spectrum is larger and the unresolved part of turbulent kinetic energy increases due to the fixed filtered length. Thus, more modeling portion should be applied to estimate the subgrid scale turbulent properties.

In the intake stroke, the F_k values are in general larger than the in the compression and expansion stroke. This phenomenon can be also understood by the governed high velocity magnitude appearing in the cylinder.

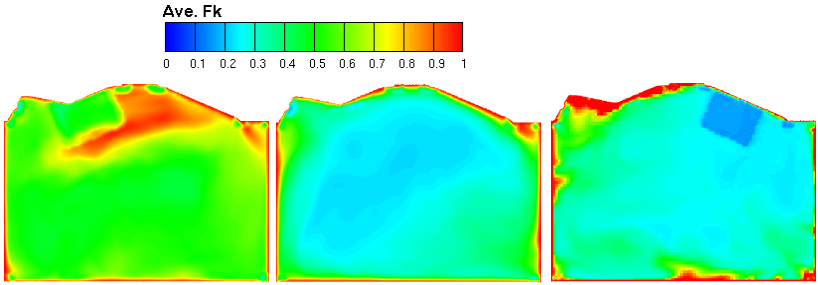

(a) 270^o bTDC (b) 90^o bTDC (c) 270^o aTDC

Figure 6.17: Modeling factor of VLES (F_k), averaged over 13 cycles

LES

The most determinative factor of simulation utilizing LES Smagorinsky model is the applied mesh resolution. As mentioned in chapter 4.1, the critical cut off wave number should lie around the end of the inertial subrange to fulfill the 80% of resolved turbulent kinetic energy criterion suggested by Pope (2000, [72]). With regard to the ICE system, Baumann et al. (2013, [7]) showed the resolving ratio to demonstrate the sufficiency of applied mesh. For this work, Fig 6.18 shows the modeling ratio of VLES

and LES. Seemingly, the applied mesh is sufficient for both utilized turbulence models. However, how could the high modeling factor of VLES (Fig 6.17) lead to the low modeling ratio?

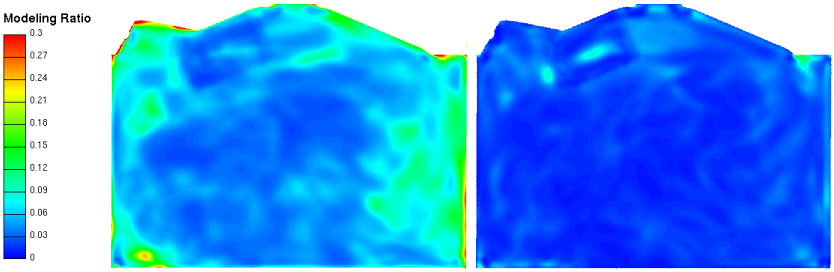

(a) VLES (b) LES

Figure 6.18: Modeling ratio ($k_{\mathrm{sgs}}/k_{\mathrm{total}}$) of VLES and LES realizations, 270^o bTDC

The crucial problem of the representations is the interpretation of turbulent properties. In the general ICE system, the total turbulent kinetic energy is obtained by three characteristics in the simulation utilizing filter based turbulence model:

Firstly, the subgrid scale turbulent kinetic energy, which is evaluated by the applied subgrid scale turbulence model.

Secondly, the resolved turbulent kinetic energy, where the flow structure are captured by the momentum equation instantaneously. This value is built by applying the averaging procedure.

Thirdly, the cycle-to-cycle variations, which is mainly due to the interaction between different scales of structure and piston movement. By utilizing the averaging procedure, these variations are also obtained in the representation of turbulent kinetic energy, while this phenomenon belongs to rather the flow characteristics than the turbulent properties.

Thus, applying the modeling ration is not accurate to demonstrate the modeling technique of LES since the CCV, which cannot be differentiated from the representation of resolved turbulent properties, possessing more than 30% in the total turbulent kinetic energy.

A suitable method to prove the mesh resolution is the Δ/η value, which shows the ratio of grid spacing to Kolmogorov length scale. In general, Δ/η should not be larger than 30 in the LES simulation utilizing Smagorinsky model. For high anisotropic turbulent flows, this value should be even

smaller the reach the local isotropic region.

RANS

Realizations of RANS k-ζ-f model has good qualitative agreement capturing the velocity profile. However, the turbulent properties mostly failed to estimate due to the missing CCV information. As mentioned in chapter 2.1, RANS applies the averaging principle to reach the main flow; multi-scale flow structures are not able to be seen, see Fig6.6(c). Hence, the CCV cannot be shown in the numerical realizations and the turbulent properties do not match the experimental data.

PANS

The only difference between RANS and PANS is the implementation of f_k. I.e., the divergence of the calculation should be due to this factor. In general, f_k denotes the ratio of modeled-to-total turbulent kinetic energy and has the formulation of Eq 2.42 in the PANS equation system. However, this equation applies the time averaging method to determine the resolved turbulent kinetic energy, which is not suitable for the time depending system. As mentioned in chapter 5.2, f_k becomes very small when the main stream changes, the momentum equation tends to apply no model (DNS level) to capture the flow structure. This becomes extreme in the thin clef area when the valves are slightly opened, where the velocity magnitude is very high and f_k is close to 0. Then, the calculation diverges due to the numerical instability.

In the report of Hasse et al. (2010, [33]), they showed the modeling factor σ of DES in the intake stroke, where σ in the intake pipe region goes high to adapt the acceleration of flow velocity according to the high Re. The f_k value of PANS completely show the inverse scale due to the defined formulation, see Fig 6.19. In this case, VLES has similar realizations to the DES results and is capable to pave the numerical instability by applying higher modeled portion.

6.4 Summary

Generally speaking, CFD is a useful tool predicting the flow phenomena in the internal combustion engine configuration. The computational results capturing the in-cylinder velocity profiles match well with the experimental data for all utilized turbulence models. However, analyzing the cyclic variations is still a difficult issue, for which the applied turbulence model is of great concern. The CCV properties are characterized in the turbulent kinetic energy by applying the phase-averaged Reynolds stress.

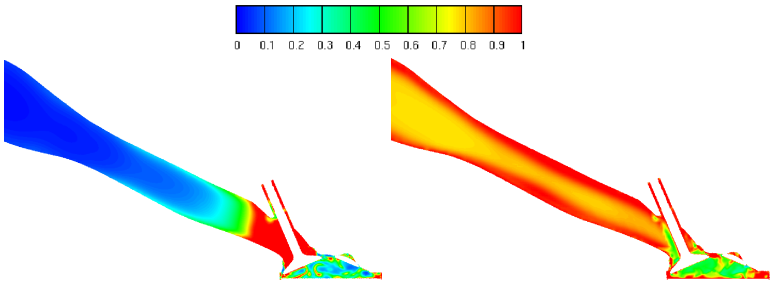

(a) PANS, f_k (b) VLES, F_k

Figure 6.19: Modeling factor in the intake pipe region

The RANS models, which are well employed in the most industrial applications, fail estimating the turbulent properties due to the missing information of interaction between fine flow structures and moving geometry.

Nowadays, LES is regarded as a promising method for the ICE configurations, which predicts the CCV phenomenon appropriately. The applied numerical mesh becomes another problem. i.e. mesh studies is necessary in the simulation procedures. Also, several piston revolutions are required for a statistically competent realization. In the work of Baumann et al. (2013, [7]), 50 cycles are observed and the realizations of turbulent properties remains very scattered, which indicates that more sample data are needed for the averaging procedure. This leads to very high computational costs.

Hybrid turbulence modeling compensates some problems of both methods. On the one hand, eddies are resolved due to the low portion of modeled stress in the momentum equation according to the grid spacing. On the other hand, the unresolved scale is estimated by the turbulence model. This methodology transfers the grid dependency problem of LES to an implicit issue. For the critical region in the ICE system, where the flow accelerates, hybrid models can adapt to the flow condition and apply more modeled portion in the momentum equation. Hence, CCV can be captured, also turbulence model restricts the calculation in the realistic range.

High computational costs is still an unavoidable problem in the simulation utilizing hybrid turbulence models. According to the report of Hasse et al. (2010, [33]), at least 13 cycles are required for the DES. However, this issue relates strongly to the geometric configuration and applied mesh

resolution. Different systems (geometry, applied equation system, mesh resolution, etc.) would have various sample requirements. The explicte criterion of minimal realization samples still requires further investigations.

7 Summary, Conclusion and Outlook

Numerical capturing of turbulent aerodynamic effects is a very challenging task; not only the computational mesh should be constructed carefully, the utilized modeling strategies should also be handled in a proper manner. Compared to the well applied RANS and LES methods, the hybrid eddy-resolving modeling technique combines the advantages of the both and exhibits an upcoming option for the industry respective to complex flow system.

In this work, two eddy-resolving modeling methodologies, the so-called Partially-Averaged Navier-Stokes (PANS) methods and Very Large-Eddy Simulation (VLES) method are validated by computing numerous flow configurations of relevance for an internal combustion engine system. Whereas the PANS method, formulated by Basara et al. (2011) was 'straightforwardly' adopted, the present VLES method represents the result of the modeling activities performed in the framework of this thesis. Both model schemes utilize the near-wall RANS k-ζ-f model as the background model; its adaptation to function as a sub-scale model within these two eddy-resolving strategies is achieved by introducing appropriately the ratio of modeled turbulent quantities (kinetic energy of turbulence and its dissipation rate) to their total counterparts formulated dynamically in terms of the corresponding filter length; the latter represents principally the ratio of the turbulent length scale pertinent to the corresponding residual motion and the representative grid-spacing. For preliminary validation, the natural decay of homogeneous isotropic turbulence, fully-developed flow in a plane channel and flow over a series of two-dimensional hills, for which an intensive numerical database originating from highly-resolved DNS and LES simulations exists in the published literature, are computed. These configurations have been carefully selected as they deal with some basic mean flow and turbulence phenomena: exponential decay of isotropic turbulence in absence of additional turbulence production, logarithmic law for the mean velocity field, strong near-wall Reynolds stress anisotropy, flow separation at a curved continuous wall associated with flow reattachment and recovery. Both computational models result in a fluctuating turbulence field in all configurations exhibiting superior performance compared

to the background RANS model. The results obtained exhibit high level of qualitative and quantitative agreement with the reference database. This relates especially to the present VLES model returning more comprehensive performance than PANS regarding the fluctuated physical properties.

Turbulent flow configurations featured by swirling and tumbling phenomena are simulated consequently, as these are the phenomena encountered principally in internal combustion engine systems. For these applications, the reference data are based on the experiments of Borée et al. (2002, [8]) and Grundmann et al. (2012, [27]). Compared to the results of the LES and RANS simulations, which have been performed in parallel by applying the same mesh and numerical settlements, the hybrid VLES method shows reliable representations of the 'three-layered' axial flow structure with alternating flow directions within the vortex tube and the cycle-to-cycle variation in a simplified engine geometry characterized by a quadratic piston. The corresponding mean flow and turbulence characteristics also match well the reference data in a realistic engine flow configuration investigated experimentally by Baum et al. (2012, [6]); the realized fields of mean velocity and turbulent properties show similar evolution compared with experimental data influenced by the moving piston and intake and outtake valves. The PANS method exhibits some deficits in the regions where the forcing effects originating from configuration geometry are weaker, as encountered in the vortex tube featured by centrically positioned outlet orifices. Also, the treatment of modeled grid resolution parameter in the time-dependent configuration pertinent to the periodically moving boundaries of the solution domain, as in the case of the internal combustion engines, is not straightforward. This is mainly influenced by applying inadequate averaging principles interactively within the computational procedure aiming at evaluating turbulent quantities necessary for determining the grid resolution parameter f_k: currently, a time-averaged value is utilized, instead of a phase-averaged value relevant to a given piston position. This can results in underestimation of modeled fraction, causing the model weakening concerning its numerical robustness deteriorating eventually convergence efficiency (Chapter 6).

Another important aspect in the simulation is the mesh design. While the mesh-independent results are expected to be achieved in steady RANS simulations, the mesh resolution remains a crucial issue when applying LES and hybrid eddy-resolving models. Hybrid models bridge the resolved and modeled properties in a seamless manner; the turbulent features are partially captured (resolved) by mesh and partially estimated by the models.

This strategy established the possibility of a mesh-independent representation by resolving the flow field in an unsteady manner. These captured physical characteristics may further contribute to a better understanding of turbulent flows in the complex system. However, there is still no a universally applicable model for all flow configurations, 'reconciling' both mesh and modeling issues. The presently formulated VLES model represents certainly a promising model with respect to bringing in accord both latter issues.

Outlook

The concept of PANS as an eddy-resolving model is innovative. Currently, the resolved velocity fluctuations are required for model implementation; the evaluation of these values towards the determination of their averaged properties is not straightforward. For the further development of this methodology, solving the transport equation for resolved turbulent kinetic energy would be important; such activity is in progress, see e.g. Basara (2014, [4]) of corresponding models. It would certainly increase the suitability of the PANS method for complex systems as well.

Regarding the numerical simulation of internal combustion engines, turbulence modeling is only one important component. Spray behavior, chemical reactions, combustion and associated interacting effects are also decisive for the purpose of estimating the burning efficiency and further applications in the engine design. Based on the realized flow field, simulation regarding spray and combustion in conjunction with the turbulence models can be carried out for further validations.

Bibliography

[1] S. Alekseenko, P. Kuibin, V. Okulov, and S. Shtork. Helical Vortices in Swirl Flow. *Journal of Fluid Mechanics*, 382:195–243, 1999.

[2] G. Almeida, D. Durao, and M. Heitor. Wake Flows Behind 2-Dimensional Model Hills. *Experimental Thermal And Fluid Science*, 7(1):87–101, Jul 1993.

[3] A. AST. AVL FIRE Userguide, v2011. Technical report, AVL GmbH, Graz, Austria, 2011.

[4] B. Basara. PANS method as a computational framework from an industrial perspectives. *5th Int. Symp. on 'Advances in Hybrid RANS-LES Modelling', Texas A and M University*, 2014.

[5] B. Basara, S. Krajnović, S. Girimaji, and Z. Pavlovic. Near-Wall Formulation of the Partially Averaged Navier-Stokes Turbulence Model. *AIAA Journal*, 49(12):2627–2636, Dec 2011.

[6] E. Baum, B. Peterson, B. Böhm, and A. Dreizler. On The Validation of LES Applied to Internal Combustion Engine Flows: Part 1: Comprehensive Experimental Database. *Flow, Turbulence and Combustion*, 10.1007/s10494-013-9468-6:1–29, 2013.

[7] M. Baumann, F. di Mare, and J. Janicka. On the Validation of Large Eddy Simulation Applied to Internal Combustion Engine Flows Part II: Numerical Analysis. *Flow, Turbulence and Combustion*, 10.1007/s10494-013-9472-x:1–19, 2013.

[8] J. Borée, S. Maurel, and R. Bazile. Disruption of a Compressed Vortex. *Physics of Fluids*, 14(7):2543–2556, JUL 2002. Symposium on Turbullent Years in Honor of John L Lumley on his 70th Birthday, Cornell Univ, ITHACA, NEW YORK, June 24-25, 2001.

[9] I. Celik, I. Yavuz, and A. Smirnov. Large Eddy Simulations of In-cylinder Turbulence for Internal Combustion Engines: A Review. *International Journal of Engine Research*, 2(2):119–148, 2001.

[10] B. Chaouat. A New Partially Integrated Transport Modelling (PITM) Method for Continuous Hybrid Non-zonal RANS/LES Simulations. In S.-H. Peng, P. Doerffer, and W. Haase, editors, *Progress in Hybrid RANS-LES Modelling*, volume 111 of *Notes on Numerical Fluid Mechanics and Multidisciplinary Design*, pages 213–224. Springer Berlin Heidelberg, 2010.

[11] S. G. Chumakov. Scaling Properties of Subgrid-scale Energy Dissipation. *Physics of Fluids*, 19(5):058104, May 2007.

[12] J. Deardorff. Three-dimensional Numerical Study of the Height and Mean Structure of a Heated Planetary Boundary Layer. *Boundary-Layer Meteorology*, 7(1):81–106, 1974.

[13] P. Durbin. Near-wall Turbulence Closure Modeling Without 'Damping Functions'. *Theoretical and Computational Fluid Dynamics*, 3:1–13, Sept. 1991.

[14] P. Durbin. A Reynolds Stress Model For Near-Wall Turbulence. *Journal of Fluid Mechanics*, 249:465–498, Apr 1993.

[15] S. Eiamsa-ard and P. Promvonge. Review of Ranque - Hilsch effects in vortex tubes. *Renewable and Sustainable Energy Reviews*, 12(7):1822 – 1842, 2008.

[16] M. Escudier, A. Nickson, and R. Poole. Influence of Outlet Geometry on Strongly Swirling Turbulent Flow Through a Circular Tube. *Physics of Fluids*, 18:125103, 2006.

[17] A. Fadai-Ghotbi, C. Friess, R. Manceau, and J. Boree. A Seamless Hybrid RANS-LES Model based on Transport Equations for the Subgrid Stresses and Elliptic Blending. *Physics of Fluids*, 22(5):055104, May 2010.

[18] H. Fasel, D. von Terzi, and R. Sandberg. A Methodology for Simulating Compressible Turbulent Flows. *Journal of Applied Mechanics-Transactions of the ASME*, 73(3):405–412, May 2006. 4th ASME/JSME Joint Fluids Engineering Conference, Honolulu, HI, Jul 06-10, 2003.

[19] C. Garth, R. S. Laramee, X. Tricoche, J. Schneider, and H. Hagen. Extraction and Visualization of Swirl and Tumble Motion from Engine Simulation Data. In *Topology-based Methods in Visualization*, pages 121–135. Springer, 2007.

[20] M. Germano, U. Piomelli, P. Moin, and W. Cabot. A Dynamic Subgrid-scale Eddy Viscosity Model. *Physics of Fluids A-Fluid Dynamics*, 3(7):1760–1765, Jul 1991.

[21] S. Ghosal, T. Lund, P. Moin, and K. Akselvoll. A Dynamic Localization Model for Large-Eddy Simulation of Turbulent Flows. *Journal of Fluid Mechanics*, 286:229–255, Mar 10 1995.

[22] S. Girimaji. Partially-averaged Navier-Stokes Model for Turbulence: a Reynolds-averaged Navier-Stokes to Direct Numerical Simulation Bridging Method. *Transactions of the ASME. Journal of Applied Mechanics*, 73:413–21, May 2006.

[23] S. Girimaji, E. Jeong, and R. Srinivasan. Partially Averaged Navier-Stokes Method for Turbulence: Fixed Point Analysis and Comparison with Unsteady Partially Averaged Navier-Stokes. *Journal of Applied Mechanics-Transactions of the ASME*, 73(3):422–429, May 2006. 4th ASME/JSME Joint Fluids Engineering Conference, Honolulu, HI, JUL 06-10, 2003.

[24] S. S. Girimaji and K. S. Abdol-Hamid. Partially–Averaged Navier-Stokes Model For Turbulence: Implementation and Validation. *AIAA paper*, 502:2005, 2005.

[25] D. Goryntsev, A. Sadiki, M. Klein, and J. Janicka. Large Eddy Simulation based Analysis of the Effects of Cycle-to-cycle Variations on Air-fuel Mixing in Realistic DISI IC-engines. *Proceedings of the Combustion Institute*, 32(2):2759 – 2766, 2009.

[26] A. Gosman, Y. Tsui, and C. Vafidis. Flow in a Model Engine with a Shrouded Valve: A Combined Experimental and Computational Study. Technical report, Society of Automotive Engineers, Inc., Warrendale, PA, 1985.

[27] S. Grundmann, F. Wassermann, R. Lorenz, B. Jung, and C. Tropea. Experimental Investigation of Helical Structures in Swirling Flows. *International Journal of Heat and Fluid Flow*, 37:51–63, Oct 2012.

[28] X. Han and S. Krajnović. *A New Very Large Eddy Simulation Model for Simulation of Turbulent Flow*, volume 117 of *Notes on Numerical Fluid Mechanics and Multidisciplinary Design*. Springer, 2012.

[29] X. Han, S. Krajnovic, and B. Basara. Study of Active Flow Control for a Simplified Vehicle Model using the PANS Method. *International Journal of Heat and Fluid Flow*, 42:139–150, Aug 2013.

[30] K. Hanjalić. Two-dimensional asymmetric turbulent flow in ducts. Technical report, PhD Thesis, Imperial College London, UK, 1970.

[31] K. Hanjalić, M. Popovac, and M. Hadziabdic. A Robust Near-wall Elliptic-relaxation Eddy-viscosity Turbulence Model for CFD. *International Journal of Heat and Fluid Flow*, 25(6):1047–1051, Dec 2004.

[32] C. Hasse, V. Sohm, and B. Durst. Detached Eddy Simulation of Cyclic Large Scale Fluctuations in a Simplified Engine Setup. *International Journal of Heat and Fluid Flow*, 30(1):32–43, Feb 2009.

[33] C. Hasse, V. Sohm, and B. Durst. Numerical Investigation of Cyclic Variations in Gasoline Engines using a Hybrid URANS/LES Modeling Approach. *Computers & Fluids*, 39(1):25 – 48, 2010.

[34] D. Haworth. Large-eddy Simulation of In-cylinder Flows. *Oil & Gas Science and Technology-Revued IFP Energies Noevelles*, 54(2):175–185, Mar-Apr 1999. Conference on Multi-Dimensional Simulation of Engine Internal Flow, RUEIL MALMAISON, FRANCE, DEC 03-04, 1998.

[35] D. Hennecke and K. Wörrlein. Flugantriebe und gasturbinen. Technical report, Technische Universität Darmstadt, 2000.

[36] J. Heywood. *Internal Combustion Engine Fundamentals*. McGraw-Hill, New York, USA, 1998.

[37] S. Jakirlić and K. Hanjalić. A New Approach to Modelling Near-wall Turbulence Energy and Stress Dissipation. *Journal of Fluid Mechanics*, 459:139–166, May 25 2002.

[38] Y. Jang, M. Leschziner, K. Abe, and L. Temmerman. Investigation of Anisotropy-resolving Turbulence Models by Rreference to Highly-resolved LES Data for Separated Flow. *Flow, Turbulence and Combustion*, 69(2):161–203, 2002.

[39] S. Johansen, J. Wu, and W. Shyy. Filter-based Unsteady RANS Computations. *International Journal of Heat and Fluid Flow*, 25(1):10–21, Feb 2004.

[40] W. Jones and B. Launder. Prediction of Laminarization with a 2-equation Model of Turbulence. *International Journal of Heat and Mass Transfer*, 15(2):301–&, 1972.

[41] T. Kamiński, M. Wendeker, K. Urbanowicz, and G. Litak. Combustion Process in a Spark Ignition Engine: Dynamics and Noise Level Estimation. *Chaos*, 14:461–466, 2004.

[42] W.-W. Kim and S. Menon. A New Dynamic One-equation Subgrid-scale Model for Large Eddy Simulation. *AIAA 33rd Aerospace Science Meeting and Exhibit*, 95:0356, 1995.

[43] M. K. King, R. R. Rothfus, and R. I. Kermode. Static Pressure and Velocity Profiles in Swirling Incompressible Tube Flow. *AIChE Journal*, 15(6):837–842, 1969.

[44] H. Kobayashi, F. Ham, and X. Wu. Application of a Local SGS Model based on Coherent Structures to Complex Geometries. *International Journal of Heat and Fluid Flow*, 29(3):640–653, Jun 2008. 5th International Symposium on Turbulence and Shear Flow Phenomena, Munich, GERMANY, AUG 27-29, 2007.

[45] A. Kolmogorov. Dissipation of Energy in the Locally Isotropic Turbulence. *Proceedings of the Royal Society of London Series A-Mathematical Physical and Engineering Sciences*, 434(1890):15–17, Jul 8 1991.

[46] P. Koutmos and C. Mavridis. A Computational Investigation of Unsteady Separated Flows. *International Journal of Heat and Fluid Flow*, 18(3):297–306, Jun 1997.

[47] S. Krajnović, R. Larusson, and B. Basara. Superiority of PANS Compared to LES in Predicting a Rudimentary Landing Gear Flow with Affordable Meshes. *International Journal of Heat and Fluid Flow*, 37:109–122, Oct 2012.

[48] S. Lakshmipathy and S. S. Girimaji. Partially-averaged Navier–Stokes Method for Turbulent Flows: k-ω Model Implementation. *AIAA paper*, 119:2006, 2006.

[49] S. Lakshmipathy and S. S. Girimaji. Partially Averaged Navier-Stokes (PANS) Method for Turbulence Simulations: Flow Past a Circular Cylinder. *Journal of fluids engineering*, 12(12):132, 2010.

[50] C. D. Langhe, B. Merci, and E. Dick. Hybrid RANS/LES Modelling with an Approximate Renormalization Group. I: Model Development. *Journal of Turbulence*, 6(6):1–18, 2005.

[51] B. Launder, G. Reece, and W. Rodi. Progress in Development of Reynolds-Stress Turbulence Closure. *Journal of Fluid Mechanics*, 68(Apr15):537–566, 1975.

[52] B. Launder and B. Sharma. Application of the Energy-dissipation Model of Turbulence to the Calculation of Flow Near a Spinning Disc. *Letters in Heat and Mass Transfer*, 1(2):131 – 137, 1974.

[53] B. Launder and D. Spalding. The numerical computation of turbulent flows. *Comput. Methods Appl. Mech. Engng.*, 3:269–289, 1974.

[54] A. Leonard. Energy Cascade in large-eddy Simulations of Turbulent Fluid Flows. *Advances in Geophysics*, 18:237–248, 1975.

[55] M. Leschziner and S. Hogg. Computation of Highly Swirling Confined Flow with a Reynolds Stress Turbulence Model. *AIAA journal*, 27(1):57–63, 1989.

[56] D. K. Lilly. The Representation of Small Scale Turbulence in Numerical Simulation Experiments. In *H. H. Doldstine (Ed.) Proc. IBM Scientific Computing Symp. on environmental Sciences. Page 195-210*, 1967.

[57] C. Lin. Modeling a Confined Swirling Coaxial Jet. *Ann. Research Briefs, Center for Turbulent Research, Stanford, EUA*, 1:211–219, 1998.

[58] J. M. Ma, S. H. Peng, L. Davidson, and F. J. Wang. A Low Reynolds Number Variant of Partially-averaged Navier-Stokes Model for Turbulence. *International Journal of Heat and Fluid Flow*, 32(3, SI):652–669, Jun 2011.

[59] R. Maduta and S. Jakirlić. *An eddy-resolving Reynolds stress transport model for unsteady flow computations*, volume 117 of *Notes on Numerical Fluid Mechanics and Multidisciplinary Design*. Springer Berlin Heidelberg, 2012.

[60] J. Magnient, P. Sagaut, and M. Deville. A Study of Built-in Filter for some Eddy Viscosity Models in Large-Eddy Simulation. *Physics of Fluids*, 13(5):1440–1449, May 2001.

[61] D. Marc, J. Borée, R. Bazile, and G. Charnay. Combined PIV and LDV Analysis of the Evolution and Breakdown of a Compressed Tumbling Vortex. In *In: 11th Symposium on Turbulent Shear flows*. In: 11th Symposium on Turbulent Shear flows, 1997.

[62] K. Matsumoto, I. Tsuda, and Y. Hosoi. Controlling Engine System: A Low-dimensional Dynamics in a Spark Ignition Engine of a Motorcycle. *Zeitschrift fur Naturforschung A-Journal of Physical Sciences*, 62(10-11):587–595, 2007.

[63] F. Menter. 2-Equation Eddy-Viscosity Turbulence Models for Engineering Applications. *AIAA Journal*, 32(8):1598–1605, Aug 1994.

[64] F. R. Menter and Y. Egorov. The Scale-Adaptive Simulation Method for Unsteady Turbulent Flow Predictions. Part 1: Theory and Model Description. *Flow, Turbulence and Combustion*, 85(1):113–138, July 2010.

[65] R. D. Moser, J. Kim, and N. N. Mansour. Direct Numerical Simulation of Turbulent Channel Flow up to Re= 590. *Physics of fluids*, 11:943, 1999.

[66] F. Nicoud and F. Ducros. Subgrid-scale Stress Modelling based on the Square of the Velocity Gradient Tensor. *Flow, Turbulence and Combustion*, 62(3):183–200, 1999.

[67] N. Ozdor, M. Dulger, and E. Sher. Cyclic Variability in Spark Ignition Engines: A Literature Survey. Technical report, SAE paper No. 940987, 1994.

[68] R. Palm, S. Grundmann, M. Weismüller, S. Šarić, S. Jakirlić, and C. Tropea. Experimental Characterization and Modelling of Inflow Conditions for a Gas Turbine Swirl Combustor. *International Journal of Heat and Fluid Flow*, 27:924–936, 2006.

[69] C. Paschereit, E. Gutmark, and W. Weisenstein. Coherent Structures in Swirling Flows and Their Role in Acoustic Combustion Control. *Physics of Fluids*, 11:2667–2678, 1999.

[70] L. J. Peltier and F. J. Zajaczkowski. Maintenance of the Near-wall Cycle of Turbulence for Hybrid RANS/LES of Fully-developed Channel Flow. Technical report, DTIC Document, 2001.

[71] S. B. Pope. A More General Effective-viscosity Hypothesis. *Journal of Fluid Mechanics*, 72:331–340, 10 1975.

[72] S. B. Pope. *Turbulent Flows*. Cambridge University Press, 2000.

[73] C. Rapp and M. Manhart. Flow over periodic hills: an experimental study. *Experiments in Fluids*, 51:247–269, 2011.

[74] R. Roback and B. V. Johnson. Mass and Momentum Turbulent Transport Experiments with Confined Swirling Coaxial Jets. Technical report, , Aug. 1983.

[75] O. L. Roy and L. L. Penven. Compression of a Turbulent Vortex Flow. *International journal of heat and fluid flow*, 19(5):533–540, 1998.

[76] M. Schäfer. *Numerik im Maschinenbau*. Springer, 1999.

[77] R. Schiestel and A. Dejoan. Towards a New Partially Integrated Transport Model for Coarse Grid and Unsteady Turbulent Flow Simulations. *Theoretical and Computational Fluid Dynamics*, 18(6):443–468, Feb 2005.

[78] U. Schumann. Subgrid Scale Model for Finite-Difference Simulations of Turbulent Flows in Plane Channels and Annuli. *Journal of Computational Physics*, 18(4):376–404, 1975.

[79] A. Seidel. Kirk-othmer encyclopedia of chemical technology. Technical report, John Wiley & Sons, 2004.

[80] S. Shtork, C. Cala, E. Fernandes, and M. Heitor. Coherent Helical Structures in Swirl Flows. *Technical Physics Letters*, 31(8):660–662, 2005.

[81] J. Smagorinsky and S. Manabe. Numerical Model for Study of Global General Circulation. *Bulletin of the American Meteorological Society*, 43(12):673–&, 1962.

[82] P. Spalart and S. Allmaras. A One-equation Tubulence Model for Aerodynamic Flows. *Recherche Aerospatiale*, 1(1):5–21, 1994.

[83] C. Speziale. Turbulence Modeling for Time-dependent RANS and VLES: A Review. *AIAA Journal*, 36(2):173–184, Feb 1998. AIAA 13th Computational Fluid Dynamics Conference, SNOWMASS VILLAGE, COLORADO, June 29-July 02, 1997.

[84] C. Speziale, S. Sarkar, and T. Gatski. Modeling the Pressure Strain Correlation of Turbulence - An Incariant Dynamic-Systems Approach. *Journal of Fluid Mechanics*, 227:245–272, Jun 1991.

[85] S. Tavoularis, J. Jiménez, and O. Leuchter. A Selection of Test Cases for the Validation of Large-Eddy Simulations of Turbulent Flows. Technical report, Fluid Dynamics Panel of AGARD, 1997. http://torroja.dmt.upm.es/turbdata/agard/.

[86] L. Temmerman, M. Leschziner, C. Mellen, and J. Frohlich. Investigation of Wall-function Approximations and Subgrid-scale Models in Large Eddy Simulation of Separated Flow in a Channel with Streamwise Periodic Constrictions. *International Journal of Heat and Fluid Flow*, 24(2):157–180, Apr 2003.

[87] M. S. Toledo, L. Le Penven, M. Buffat, A. Cadiou, and J. Padilla. Large Eddy Simulation of the Generation and Breakdown of a Tumbling Flow. *International Journal of Heat and Fluid Flow*, 28(1):113–126, Feb 2007.

[88] A. Travin, M. Shur, M. Strelets, and P. Spalart. Detached-eddy Simulations Past a Circular Cylinder. *Flow, Turbulence and Combustion*, 63(1-4):293–313, 2000.

[89] O. Vermorel, S. Richard, O. Colin, C. Angelberger, A. Benkenida, and D. Veynante. Towards the Understanding of Cyclic Variability in a Spark Ignited Engine using Multi-cycle LES. *Combustion and Flame*, 156(8):1525–1541, 2009.

[90] O. Veromel, S. Richard, O. Colin, C. Angelberger, and A. Benkenida. Predicting Cyclic Variability in a 4 Valve SI Engine using LES and the AVBP CFD code. In *International Multidemensional Engine Modeling*, 2007.

[91] O. Vitek, J. Macek, and B. Mares. LES Simulation of Motored Internal Combustion Engine. In *International Scientific Conference of Czech and Slovak University Departments and Institutions Dealing with Research of Combustion Engines*, 2011.

[92] O. Vitek, J. Macek, Tatschl, R., Z. Pavlovic, and P. Priesching. LES Simulation of Direct Injection SI-Engine In-Cylinder Flow. Technical report, SAE Paper Technical Series, SAE Paper Technical Series 2012, 2012.

[93] M. Voisine, L. Thomas, J. Borée, and P. Rey. Spatio-temporal Structure and Cycle to Cycle Variations of an In-cylinder Tumbling Flow. *Experiments in Fluids*, 50(5):1393–1407, 2011.

[94] S. Wallin and A. Johansson. An Explicit Algebraic Reynolds Stress Model for Incompressible and Compressible Turbulent Flows. *Journal of Fluid Mechanics*, 403:89–132, Jan 25 2000.

[95] P. Wang, X. Bai, M. Wessman, and J. Klingmann. Large Eddy Simulation and Experimental Studies of a Confined Turbulent Swirling Flow. *Physics of fluids*, 16:3306, 2004.

[96] D. Wilcox. Reassessment of the Scale-determining Eaqtion for Advanced Turbulence models. *AIAA Journal*, 26(11):1299–1310, NOV 1988.

[97] H. XingSi, Y. TaoHong, and C. YiLiang. Calibration of a New Very Large Eddy Simulation (VLES) Methodology for Turbulent Flow Simulation. *Science China-Physics Mechanics & Astronomy*, 55(10):1905–1914, Oct 2012.

[98] A. Yoshizawa. A Statistically Drived System of Equations for Turbulent Shear Flows. *Physics of Fluids*, 28(1):59–63, 1985.

Nomenclature

Latin letters

upper case

symbol	description
C	Constant of universal log-law, 5.4
C_K	Kolmogorov Constant, 1.5
C_s	Smagorinsky Constant, 0.1-0.2
C_E	dissipation rate Constant, 0.9-1.1
C_{ij}	Cross stress
C_f	drag coefficient
D	diameter of vortex tube
F_k	ratio of unresolved to unsteady turbulent kinetic energy, VLES
F_ϵ	ratio of unresolved to unsteady dissipation rate, VLES
F_r	ratio of residual to unsteady turbulent viscosity, VLES
L	characteristics length scale
L_{ij}	Leonard stress
E_k	turbulent kinetic energy in Fourier space
G	filter function
N	averaging sample number
Nx, Ny, Nz	cell number in x, y, z direction
Q	second invariance of velocity gradient tensor
R_{ij}	subgrid scale Reynolds stress
Re	Reynolds number
Re_c	critical Reynolds number
Re_λ	Reynolds number for homogeneous turbulence
Re_τ	Reynolds number for plane channel flow
Re_H	Reynolds number based on height of 2D hill geometry

$\overline{S}_{ij}$	mean rate of strain
$\widetilde{S}_{ij}$	filtered rate of strain
$\overline{\Omega}_{ij}$	mean rate of rotation
$\widetilde{\Omega}_{ij}$	filtered rate of strain
U	characteristics velocity scale
U^+	mean velocity normalized by friction velocity
U_τ	friction velocity
$\overline{U}$	mean velocity
$\widetilde{U}$	filtered velocity
V_p	maximal piston velocity

lower case

symbol	description
$a(t)$	piston position in the dependency of time
a_{ij}	parameters of Butcher's array
b_i	parameters of Butcher's array
c_i	parameters of Butcher's array
f	elliptic relaxtion function, k-ζ-f model
f_k	ratio of unresolved to total turbulent kinetic energy, PANS
f_ϵ	ratio of unresolved to total dissipation rate, PANS
f_u	elliptic relaxtion function for subgrid properties, PANS
f_{us}	elliptic relaxtion function in unsteady module, VLES
f_μ	dampling function for turbulent viscosity, low-Re k-ϵ model
$f_{\tilde{\epsilon}}$	dampling function for dissipation rate, low-Re k-ϵ model
h	height of 2D-hill geometry
k	turbulent kinetic energy
k_{res}	resolved turbulent kinetic energy
k_u	residual turbulent kinetic energy
k_{us}	unsteady turbulent kinetic energy
l_c	characteristic length scale
$\dot{m}_f$	mass flux on surface f

n_i	normal vector
p''	aberration pressure for iterative pressure correction
t	time
u_c	characteristic velocity scale
u_i'	fluctuated part of velocity
u_i^*	residual part of velocity
u''	aberration velocity for iterative pressure correction
$\overline{u_i' u_j'}$	Reynolds stress tensor
$\overline{v^2}$	to-wall nnoraml stress
y	to-wall distance
y^+	normalized to-wall distance
z	axial direction in the vortex tube

Greek letters

upper case

symbol	description
Δ	grid spacing
Δt	time step
Λ	integral length scale
Λ_{us}	unsteady modeled integral length scale
Ω	engine speed
Ψ	known function for the time derivative numerical procedure

lower case

symbol	description
α	diffusion coefficient
β	coefficients of analytical solution of Reynolds stress tensor
β	blending factor

γ	variable of filter function
δ	constant of original VLES formulation
δS	control surface
δV	control volume
χ	Kolmogorov length scale
η	ratio of grid spacing and subgrid model parameter
ϵ	dissipation rate
ϵ_u	residual dissipation rate
ϵ_{us}	unsteady dissipation rate
λ	Taylor length scale
κ	wave number
κ	von Karman constant
κ_c	cut off wave number
ϕ	concerned physical property
$\overline{\phi}$	mean part of concern physical property
ϕ'	fluctuation part of concern physical property
ν	molecular viscosity
ν_t	turbulent viscosity
ν_u	subgrid-scale turbulent viscosity
ω	turbulent frequency
ρ	density
τ_w	wall shear stress
τ_{ij}	residual stress
ξ	sample number index
ζ	ratio of turbulent to-wall normal stress to kinetic energy

Abbreviations

symbol	description
aTDC	after Top Dead Center
bTDC	before Top Dead Center
BDC	Bottom Dead Center
CA	Crank Angle
CAD	Computer-Aided Design
CCV	Cycle-to-Cycle Variation
CR	Compression Ratio
CDS	Central Differencing Scheme
CFD	Computational Fluid Dynamics
DNS	Direct Numerical Simulation
DHIT	Decay of Homogeneous Isotropic Turbulence
ER	Eddy Resolving
EVM	Eddy Viscosity Model
FVM	Finite Volume Method
LES	Large Eddy Simulation
LUDS	Linear Upwind Differencing Scheme
PANS	Partially Averaged Navier-Stokes
PIV	Particle Image Velocimetry
QUICK	Quadratic Upwind Interpolation for Convection Kinematics
RANS	Reynolds Averaged Navier-Stokes
RPM	Revolution per minute
RSM	Reynolds Stress Model
SIMPLE	Semi-Implicit Method for Pressure Linked Equations
TDC	Top Dead Center
VLES	Very Large Eddy Simulation
UDS	Upwind Differencing Scheme
URANS	Unsteady Reynolds Averaged Navier-Stokes

List of Figures

List of Tables

Chi-Yao Chang

Institute for
Fluid Mechanics and Aerodynamics
Technische Universität Darmstadt
Alarich-Weiss-Str. 10
D-64287 Darmstadt
Germany

phone: +49 6151 16-6553
fax: +49 6151 16-6246
email:
chang@sla.tu-darmstadt.de

Personal

Born on May 01, 1981, in Taipei, Taiwan R.O.C.

Education

Apr. 2009 - Dec. 2013	Doctoral research in Mechanical Engineering (Dr.-Ing.), Technische Universität Darmstadt, Darmstadt, Germany
Oct. 2005 - Feb. 2009	Studies in Mechanical Engineering (Dipl.-Ing.), Technische Universität Darmstadt, Darmstadt, Germany
Sep. 1999 - Aug. 2003	Studies in Civil Engineering (B.Sc), National Chiao Tung University, Hsin-Chu, Taiwan, R.O.C.

Employment

May 2013 - Sep. 2013	Research assistant at Institute for Fluid Mechanics and Aerodynamics, Technische Universität Darmstadt, Darmstadt, Germany
Nov. 2009 - Apr. 2013	Scholarship holder of AVL List GmbH Graz, Austria